SMOS validation in the Skjern River Catchment, Denmark

Bircher, Simone

Publication date:
2011

Document Version
Publisher's PDF, also known as Version of record

SMOS validation in the Skjern River Catchment, Denmark

PhD Thesis

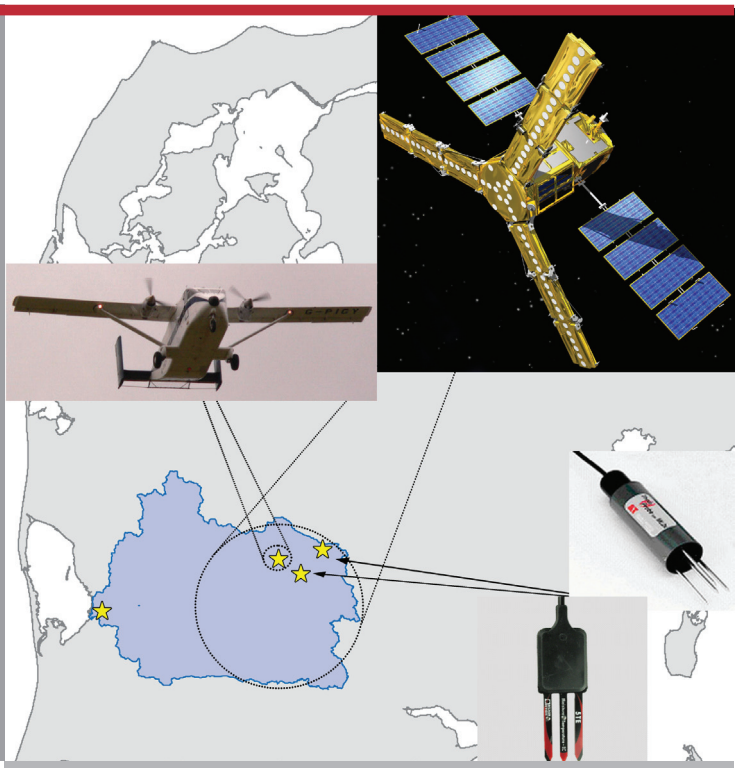

Simone Bircher
October 2011

DTU Space
National Space Institute

SMOS Validation in the Skjern River Catchment, Denmark

Simone Bircher
DTU Space, Technical University of Denmark
PhD Thesis, Kongens Lyngby, October 31, 2011

Financed by DTU Space, Technical University of Denmark, and
Hydrological Observatory and Exploratorium (HOBE, funded by Villum Foundation).

Supervised by Prof. Niels Skou, DTU Space, Technical University of Denmark,
Assoc. Prof. Henning Skriver, DTU Space, Technical University of Denmark, and
Assoc. Prof. Inge Sandholt, Department of Geography and Geology, University of Copenhagen.

http://www.space.dtu.dk

ISBN-13 978-87-92477-09-5

Preface

This thesis is submitted in fulfillment of the requirements for obtaining a PhD degree at DTU Space, National Space Institute, Technical University of Denmark. The PhD project was carried out within the Division of Microwaves and Remote Sensing, DTU Space , under the supervision of Professor Niels Skou (DTU Space), Associate Professor Henning Skriver (DTU Space), and Associate Professor Inge Sandholt (Department of Geography and Geology, University of Copenhagen).

The PhD research and related activities have been conducted in the framework of the Hydrological Observatory and Exploratorium (HOBE, funded by the Villum Foundation) by which the program was also partly financed.

Several external research stays of 1-2 months were spent in the team of the SMOS Principal Investigator, Yann Kerr, at the Centre d'Etudes Spatiales de la Biosphère (CESBIO) in Toulouse, France. For a short while, work was also carried out in the group of Professor Karsten Høgh Jensen at the Department of Geography and Geology, University of Copenhagen. During the establishment of the soil moisture and temperature network and the organisation of the HOBE SMOS Calibration/Validation (Cal/Val) Campaign, approximately three months were spent in the Skjern River Catchment in Western Denmark.

In the course of the PhD project, the opportunity was given to participate in several SMOS workshops as well as in the Australian Airborne Cal/Val Experiments for SMOS (AACES) in the Murrumbidgee Catchment, southeast Australia, under the lead of Professor Jeff Walker, Sandy Peischl and Chris Rüdiger (Department of Civil Engineering, Monash University, Monash, Australia).

In connection with the HOBE Cal/Val Campaign, an academic field course was organized in cooperation with Professor Christian Hauck (Department of Geosciences, University of Fribourg, Switzerland) in the framework of their master program.

Simone Bircher

Kongens Lyngby, October 2011

Abstract

Soil moisture is a key variable for water resources management, weather and climate predictions as well as hazard analysis. It is highly variable in space and time across scales, and thus difficult to assess. The European Space Agency's Soil Moisture and Ocean Salinity (SMOS) satellite with a passive L-band microwave radiometer on board is the first mission dedicated to surface soil moisture monitoring from space with global coverage every three days. By means of a complex retrieval algorithm, soil moisture is derived from the acquired brightness temperatures. Currently, data validation is performed across a range of climatic regions. In this context, the overall objective of this dissertation is SMOS validation in the Skjern River Catchment in Denmark, including the acquisition of the required in situ data, and its comparison with the SMOS products.

Data collection included a short-term airborne campaign with the L-band radiometer EMIRAD-2 and in situ measurements, as well as the establishment of a soil moisture and temperature network. To a priori increase the probability of a representative network average at SMOS scale (∼40-50 km), a method based on analysis of the prevailing environmental conditions was developed and successfully applied. In addition to retrieved soil moisture, validation also involved SMOS brightness temperature data and the most sensitive parameters of the retrieval algorithm. Using two complementary data sets allowed for comprehensive analysis over spatial and temporal scales. While the campaign data set of high spatial coverage and density proved of value for site-specific determination of important algorithm parameters, the long-term network record enables the assessment of temporal trends.

Consistent with worldwide findings, results show that SMOS well captures the temporal soil moisture dynamics in the Skjern River Catchment. However, the retrieved soil moisture shows a constant dry-bias and exhibits a stronger precipitation response compared to the in situ measurements. In addition to the broadly discussed Radio Frequency Interferences (RFI) and a mismatch in sampling depth between in situ sensors and L-band emission depth, several inaccuracies in the algorithm could be located as most likely error sources at the Danish site. This includes the vegetation optical depth and surface roughness parameters, soil properties and the Dobson dielectric mixing model.

This dissertation is not only a valuable contribution to SMOS validation, but can also be supportive for upcoming space missions such as NASA's Soil Moisture Active and Passive, SMAP. Knowing the current caveats the use of SMOS data in regional and global modeling of water resources and climate can be initiated. Future work in the Skjern River Catchment will focus on the disclosed error sources, as well as the influence of organic layers by means of not yet explored campaign data.

Dansk Resume

Jordfugtighed er en afgørende parameter for styring af vandressourcer, for vejr- og klimaforudsigelser, samt for risikoanalyser. Parameteren er vanskelig at bestemme, idet den er stærkt variabel alt efter hvilken tidslig og/eller rumlig skala, der benyttes. ESAs Soil Moisture and Ocean Salinity-satellit, som har et passivt L-bånds mikrobølgeradiometer om bord, er den første mission dedikeret til monitering af overfladejordfugtighed fra rummet med global dækning hver tredie dag. Via en kompleks algoritme udledes jordfugtigheden af de opsamlede brightness-temperaturer. Aktuelt foretages datavalidering på tværs af flere forskellige klimazoner. Det overordnede mål med denne afhandling validering af SMOS-data fra oplandet for Skjern Å i Danmark, herunder indsamling af de nødvendige in-situ data, samt at sammenligne disse med SMOS-dataprodukterne.

Dataindsamlingen omfattede dels en to-ugers kampagne, bestående af målinger med det flybårne L-båndsradiometer EMIRAD-2 samt in-situ-målinger, dels etableringen af et jordfugtigheds- og temperaturnetværk. For at sandsynliggøre et repræsentativt netværksgennemsnit ved SMOS-skala (∼40-50 km), blev en metode baseret på analyse af de fremherskende miljømæssige forhold udviklet og siden anvendt med succes. Udover beregnet jordfugtighed omfattede valideringen også SMOS brightness-temperaturdata, samt udledningsalgoritmens mest følsomme parametre. Anvendelsen af to komplementære datasæt muliggjorde en omfattende analyse over rumlige og tidslige skalaer. Mens datasættet fra kampagnen - med høj rumlig dækning og tæthed - viste sig værdifuldt i forbindelse med lokalitetsspecifik bestemmelse af vigtige parametre, gør langtidsmålingerne fra netværket det muligt at bedømme tidsmæssige tendenser.

Konsistent med øvrige observationer på verdensplan viser resultaterne, at SMOS er i stand til at opfange den tidsmæssige dynamik med hensyn til jordfugtighed i Skjern Å-området. De udledte værdier bliver imidlertid konsekvent underestimeret og udviser desuden en kraftigere nedbørsrespons i forhold til in-situ-målingerne. Udover forekomster af højfrekvent interferens (RFI) samt et misforhold mellem in-situ-sensorernes samplingsdybde og den maksimale L-båndsemissionsdybde, er der adskillige unøjagtigheder i algoritmen, der kunne udpeges som de mest sandsynlige fejlkilder med hensyn til måleområdet, herunder parametrene for optisk vegetationsdybde og overfladeruhed samt Dobsons dielektricitetsmodel.

Denne afhandling er ikke blot et værdifuldt bidrag til SMOS-validering, men kan også understøtte kommende rumbaserede missioner såsom NASAs Soil Moisture Active and Passive. Et kendskab til de aktuelle forbehold betyder, at anvendelsen af SMOS-data i forbindelse med modellering af vandressourcer og klima vil kunne påbegyndes. Det fremtidige arbejde i Skjern Å-området vil have fokus på de oplyste fejlkilder samt på indflydelsen af organiske lag. Dette vil ske ved anvendelse af kampagnedata, som endnu ikke er undersøgt.

Contents

List of Figures

List of Tables

List of Abbreviations

AACES	Australian Airborne Cal/Val Experiments for SMOS
AMSR-E	Advanced Microwave Scanning Radiometer for EOS
ASCAT	Advanced SCATterometer
AUX	AUXiliary
Cal/Val	Calibration and Validation
CESBIO	Centre d'Etudes Spatiales de la BIOsphère
CORINE	COoRdinated INformation on the European Environment
DFFG	Discrete Flexible Fine Grid
DGG	Discrete Global Grid
DMI	Danish Meteorological Institute
DTU	Technical University of Denmark
ECMWF	European Centre for Medium-range Weather Forecasts
EGI	Inertial navigation system
ERS	European Remote Sensing
ESA	European Space Agency
FAO	Food and Agriculture Organization of the United Nations
FC	Field Capacity
FEU fraction	Urban land fraction
FFO fraction	Forest fraction
FMO fractions	Radiometric land cover fractions
FNO fraction	Low vegetation fraction
FRZ fraction	Frost fraction
FSM fraction	Non permanent mixed snow fraction
FSW fraction	Non permanent wet snow fraction
FWL fraction	Wetland fraction
FWO fraction	Open water fraction
GIS	Geographic Information System
HOBE	Hydrological OBservatory and Exploratorium
IPCC	Intergovernmental Panel on Climate Change
ISLSCP	International Satellite Land Surface Climatology Project
ISSS	International Soil Science Society
LATT	Laboratoire Astrophysique de Toulouse - Tarbes
L1C	Level 1C
L2	Level 2
LAI	Leaf Area Index
L-MEB	L-band Microwave Emission of the Biosphere
MeTop	Meteorological Operational satellite programme
MW	MicroWaves
MIR	Medium InfraRed

MODIS	MODerate Resolution Imaging Spectroradiometer
NASA	National Aeronautics and Space Administration
NIR	Near InfraRed
PWP	Permanent Wilting Point
RFI	Radio Frequency Interference
RMSE	Root Mean Square Error
SAR	Synthetic Aperture Radar
SMAP	Soil Moisture Active and Passive
SMMR	Scanning Multi-channel Microwave Radiometer
SMOS	Soil Moisture and Ocean Salinity
SRTM	Shuttle Radar Topography Mission
SSM/I	Special Sensor Microwave/Imager
SVAT	Soil-Vegetation-Atmosphere Transfer
TIR	Thermal InfraRed
TOA	Top Of Atmosphere
UV	Ultraviolet Radiation
VIS	VISible

List of Symbols

$CHI2\_P$	SMOS L2 parameter expressing probability that no anomaly occured about the model fit
DQX	SMOS Data Quality Index
E	Energy
ET	Evapotranspiration
FL_NO_PROD	SMOS L2 confidence flag raised when retrieval failed
H_R	Parameter expressing the intensity of roughness effects
H_{R_Min}	Parameter to express H_R as function of soil moisture
M	Mass
M_AVA0	SMOS L2 parameter expressing number of views initially available for given DGG node
N_{RH}/N_{RV}	Parameter for modulation of reflectivity as function of incidence angle for H/V, respectively
N_RFI_X/Y	SMOS L2 parameter expressing number of deleted views due to RFI in X/Y polarization, respectively
P	Precipitation
Q	Runoff
Q_R	Parameter expressing polarization mixing effects of roughness
S_D	Root mean square deviation of the mean height
T	Physical temperature
T_B	Brightness Temperature
T_{EFF}	Soil effective temperature
T_v	Vegetation temperature
V	Volume
VWC	Vegetation Water Content
X_SWATH	SMOS L2 parameter expressing absolute abscissa of dwell line
a	Air
b	Vegetation parameter accounting for canopy type/structure
c	Speed of light ($2.99792458 \cdot 10^8 \mathrm{m/s}$)
e	Emissivity
f	Void
h	Planck's constant ($6.626068 \cdot 10^{-34} \mathrm{m^2\,kg/s}$)
i	Incident electromagnetic wave
p	Polarization
s	Solid
t	Total

tr	Transmissivity
tt_H/tt_V	Parameters to express τ_{NAD} as a function of incidence angle for H/V, respectively
w	Water
ΔS	Change in storage
$\varepsilon'/\varepsilon''$	Real/imaginary part of relative permittivity (dielectric constant), respectively
Γ	Reflectivity
Γ^*	Fresnel reflectivity (perfectly smooth surface)
η	Porosity
γ	Vegetation transmissivity
λ	Wavelenght
ν	Frequency
ω	Single scattering albedo of the canopy
ρb	Density of dry bulk material
ρW	Density of water
σ°	Backscattering coefficient
τ_{NAD}	Vegetation optical depth at nadir
θ	Incidence angle
θ_{Vol}	Volumetric soil moisture
θ_{Grav}	Gravimetric soil moisture

Part I.

Objectives, Background and Methods

1. Motivation and Objectives

The assessment of water resources is vital under changing climate and land use and a steadily increasing population (e.g. *FAO-Aquastat*, 2003). Soil moisture is one of the key functions in the water balance. It significantly impacts water and energy exchanges at the land surface-atmosphere interface and represents the main source of water for agriculture and natural vegetation. Many authors (*Famiglietti et al.*, 1998; *Mohanty et al.*, 2000; *Western et al.*, 2002) have reported that soil moisture is highly variable both in space and time and across scales as a result of (1) spatially variable land surface properties (namely soil and vegetation properties, climate and topography), and (2) anthropogenic influences, e.g. agricultural practices. Furthermore it has been found that the relative importance of these individual influencing factors depends on local environmental conditions and on the temporal and spatial scale at which they are acting relative to the soil moisture variability scale (*Entin et al.*, 2000). The above render soil moisture highly difficult to assess and turn it into one of the major uncertainties in a large range of applications from hydrologic, weather forecast and climate modeling to agriculture, water management or flood monitoring.

Only spaceborne sensors have the capability to provide the required global long-term soil moisture observations. The first mission dedicated to this purpose is the Soil Moisture and Ocean Salinity satellite SMOS (*Kerr et al.*, 2001, 2010) with a passive L-band (1.4 GHz) microwave radiometer on board - the technique currently believed to be most effective for the remote assessment of soil moisture (*Kerr*, 2007; *Wagner et al.*, 2007). Since its launch at the beginning of November 2009, SMOS has been acquiring data with global coverage every three days. Based on the L-band Microwave Emission of the Biosphere (L-MEB) radiative transfer model (*Wigneron et al.*, 2007) brightness temperatures (T_B) are calculated from an initial soil moisture guess as well other auxiliary input (auxiliary products). The modeled T_Bs are compared to the ones measured by SMOS (Level 1C product) at ∼44 km spatial resolution. Using this multi-angular and full polarization information a cost function is minimized to retrieve surface soil moisture (∼0-5 cm depth), vegetation optical thickness and other parameters (Level 2 product) for each node of the so-called Discrete Global Grid (DGG, *Kerr et al.*, 2011) with ∼15 km spacing.

After the first half year commissioning phase with intense instrument checks and decisions on calibration and polarization mode, SMOS was declared to perform according to expectations and the data considered sufficiently good for distribution. However, though operating in a protected band for scientific exploration, SMOS data quality turned out to be seriously affected by Radio Frequency Interferences (RFI). Furthermore, there are still unresolved image reconstruction issues, and inaccuracies in both the retrieval algorithm and in the auxiliary data. Thus, at this point, an important step is data validation by independent in situ measurements across a range of climatic regions. Worldwide the SMOS retrieval algorithm and its associated products are currently checked to identify inaccuracies and anomalies (*Delwart et al.*, 2008). By means of the feedback from the SMOS calibration and

validation (Cal/Val) teams, the algorithm is adjusted and the data reprocessed accordingly to steadily improve the SMOS products.

Beside the high spatial and temporal variability of soil moisture across scales, the comparison of satellite data with ground measurements is complicated by the distinct scale-mismatch between the large satellite footprints and the point measurements on the ground (*Cosh et al.*, 2004). This entails the necessity of a high number of distributed observations of the latter to accurately represent the satellite scale. Two approaches have been widely used to attain the required data for satellite validation and together they also constitute the core of SMOS Cal/Val activities: (1) short-term intensive field campaigns, and (2) soil moisture networks.

The first method is often a combination of an airborne campaign with concurrent ground measurements at the times of the satellite overpasses. Several such campaigns were carried out in preparation of and during the Cal/Val for SMOS and other satellite missions, e.g. Australia (*Panciera et al.*, 2008; *Merlin et al.*, 2008; *Peischl et al.*, In Prep.); Germany (*Dall'Amico et al.*, 2010; *Kainulainen et al.*, 2010); France (*Albergel et al.*, 2011); USA (*Schmugge et al.*, 1988; *Jackson et al.*, 1995, 1999); Finland: (*Kontu et al.*, 2010). Via the airborne measurements with a footprint of few kilometers, this offers the advantage of stepwise validation across spatial scales. Furthermore, the airborne and satellite data can be compared at brightness temperature level excluding uncertainties inherent in the model-derived soil moisture product. Nevertheless, due to high costs this method outputs snapshot data for very limited time spans and thus only provides reliable estimates for a subset of environmental and climatic conditions.

This drawback can be overcome by means of the second method: Permanently installed soil moisture networks with several sensors distributed in space monitor continuously at high temporal resolution. Such networks have recently evolved across all continents of the world, e.g. USA (*Bosch et al.*, 2006; *Schaefer et al.*, 2007; *Jackson et al.*, 2010); Canada (*Champagne et al.*, 2010); Australia (*Walker et al.*, 2001; *Merlin et al.*, 2008); Africa (*de Rosnay et al.*, 2009); Europe - Spain (*Martinez-Fernandez and Ceballos*, 2003), France (*Calvet et al.*, 2007), Germany (*Krauss et al.*, 2010; *Bogena et al.*, 2010). Many of them can be found in the International Soil Moisture Network Database (*Dorigo et al.*, 2011), the follow-up of the historical Global Soil Moisture Data Bank (*Robock et al.*, 2000). Yet, these networks often face constraints of either limited network-density or spatial extent (*Cosh et al.*, 2004). Therefore, the identification of spatially representative locations for the individual network stations is a crucial issue.

One of the official SMOS Cal/Val sites is situated in the Skjern River Catchment in Western Denmark. The importance of validating SMOS data at the Danish site is twofold. First, it complements the other Cal/Val regions in that it is Europe's northernmost intensely cultivated area with features related to latitude-specific environmental conditions such as heathland and very sandy soils with large organic deposits. This imposes specific hydrological processes including the evolution of soil moisture. Secondly, the area is located at short distance to the coast line in two directions. Since there is a large difference in the signal contribution originating from land and from open water (brightness temperatures in the order of 250 and 100 K, respectively), a small open water fraction highly influences the signal measured by SMOS. Thus, this site can be used to test techniques for removing open water impacts on SMOS data rendering it useful in coastal areas. The site benefits

from temporally increased data acquisition at this latitude and from its pronounced flatness where topographical influences are unlikely.

In the framework of the Danish Hydrological Observatory and Exploratorium (HOBE, `www.hobe.dk`, *Jensen and Illangasekare*, 2011), work package 3 - soil moisture and recharge - the main objective of this dissertation was the validation of SMOS data from one selected node (DGG 2002029) and the corresponding pixel (surrounding area of 44 km in diameter). A first goal was the acquisition of the required in situ data, through (1) the design and establishment of a soil moisture and temperature network, and (2) the planning and realization of an airborne campaign with the L-band radiometer EMIRAD-2 and concurrent ground measurements of soil moisture and auxiliary parameters. The second goal was then the comparison of the collected data with measured Level 1C (L1C, brightness temperature) and retrieved Level 2 (L2, soil moisture and vegetation optical depth) SMOS data. Furthermore, it included the investigation of the quality of the main auxiliary parameters (AUX, surface temperature, vegetation and roughness model parameters, land cover and soil properties) used to initialize the SMOS retrieval algorithm in order to identify potential sources of inaccuracies inherent in the final data product.

Chapter 2 of Part I covers an introduction to the hydrologic cycle, soil moisture and its spatial and temporal variability across scales, as well as an overview over remote sensing and its application for soil moisture assessment. In Chapter 3, the chosen approach of this dissertation is illustrated and an introduction to each scientific article is given. The four articles are then found in Part II. Finally, in Part III an overall discussion, main conclusions of the thesis as well as an outlook on future work are given.

2. Background

2.1. Hydrologic Cycle

The hydrologic cycle describes the transportation and storage of the earth's water driven by the sun. Transportation includes sublimation and evapotranspiration, advection, condensation (cloud formation), liquid and solid precipitation, melting of snow and ice, surface runoff, infiltration, percolation and subsurface discharge (Fig. 2.1) In between the water is stored in the oceans (97.2%), in the atmosphere (0.001%), in inland waters and lakes (0.017%) and rivers (0.0001%), in ice sheets and glaciers (2.15%), in the ground as soil moisture (0.005%) and groundwater (0.62%) (*Strahler and Strahler*, 1999). Generally, the cycle can be split into four components which together add up to the water balance as following:

$$P = Q + ET + \Delta S \tag{2.1}$$

with P: precipitation, Q: runoff, ET: evapotranspiration (transportation), and ΔS: change in storage.

Under a changing climate, changes in the intensity of the transportation processes as well as a redistribution of the water content in the different storages can be expected. The Intergovernmental Panel on Climate Change (*IPCC*, 2007) predicts an intensification of the water cycle throughout the 21st century with an increase in precipitation in some areas and a decrease, and consequently a higher probability of drought, in others. Also, more water will be stored in oceans and less as ice and snow as a result of currently increasing global temperatures. Furthermore, changing land use practices are leading to altered runoff conditions. The assessment of the current and future water distribution is thus of high importance, especially given the increasing world's population leading to steadily augmented demand of water supply.

Hydrologic, weather forecast and climate models constitute important tools for the assessment of the water distribution. Currently, problems exist with closing the water balance in hydrologic models (e.g. *Plauborg et al.*, 2003). Although, significant progress has been made in recent years, we have to keep in mind that models are always an approximation of the reality. Many assumptions and simplifications must be made introducing errors to the model output. One of the major uncertainties is soil moisture. At this stage, it also remains a 'tuning parameter' in weather prediction models as operational observations are lacking.

2.2. Soil moisture

2.2.1. Relevance

Although a tiny fraction, soil moisture is a very influential store of water in the hydrologic cycle. Where rainfall lands on the soil surface, a fraction infiltrates into the soil to replenish

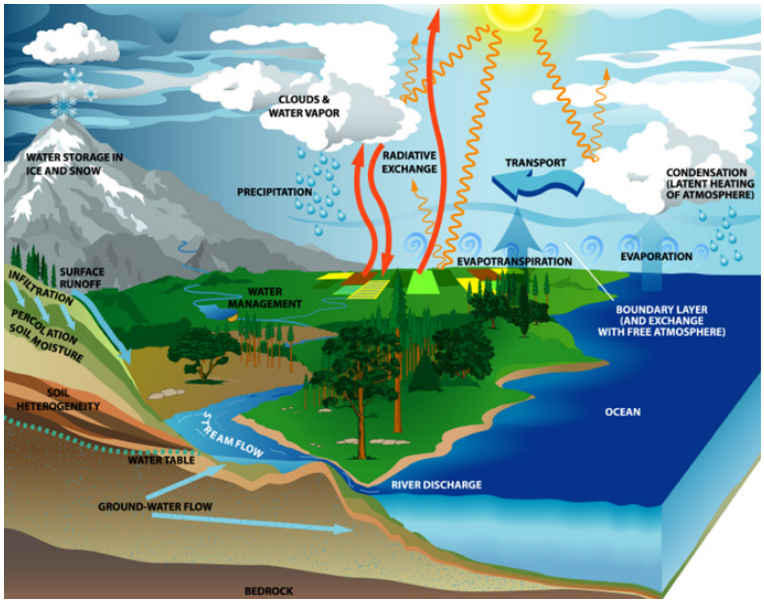

Figure 2.1.: Schematic representation of the earth's water cycle (source: `http://smap.jpl.nasa.gov/files/smap2/cycle3.jpg`, 06.10.2011).

the soil water or flows through to recharge the groundwater. Another fraction may run off as overland flow and the remaining fraction is depleted by soil evaporation and plant transpiration back into the atmosphere (*Bot and Benites*, 2005). Drainage from the soil profile is the primary source of recharge for many groundwater systems, and capillary rise from shallow groundwater tables can be an important source for the water storage during drier periods (*Western et al.*, 2002). The above-mentioned processes do not occur at the same moment. Some are instantaneous, such as runoff taking place during a rainfall event, while others are continuous such as evaporation/transpiration and infiltration.

By partitioning net radiation into latent and sensible heat components, and rainfall into runoff and infiltration, soil moisture significantly impacts water and energy exchanges at the land surface-atmosphere interface (*Schmugge et al.*, 1980). In the atmosphere, soil moisture is one of the determining variables for both short-term processes (weather) and long-term processes (climate) in the atmosphere. The availability of soil moisture governs the moisture in the atmosphere which in turn is crucial for precipitation processes. Moreover, moist/dry surfaces result in reduction/increase in the daily amplitude of air temperature, which amongst others also leads to a very complex relationship between soil moisture, convective processes and thunderstorms. In the long run, the soil water content can be responsible for positive climate feedback effects as given in the following example: less summer precipitation leads to less soil water content, causing plant water stress and a decrease of evapotranspiration/latent heat flux as well as an increase of sensible heat flux and near-surface temperatures. This all the more reduces summer precipitation and triggers the consequences, overall resulting in an enhanced climate change signal of summer temperatures. Furthermore, soil moisture influences a variety of soil and plant growth related processes (e.g. rate of plant water-uptake), as it represents the main source of water

for agriculture and natural vegetation. To minimize the impact of drought, soil needs to capture the rainwater that falls on it, store as much of the water as possible for future plant use, and allow for plant roots to penetrate and proliferate. Problems with or constraints on one or several of these conditions cause soil moisture to be one of the main limiting factors for crop growth (*Bot and Benites*, 2005). Consequently agricultural production and practices are highly dependent on the availability of soil moisture (e.g. improved yield forecasting and irrigation scheduling). Last but not least, antecedent soil moisture conditions co-determine flooding. Thus, soil moisture is a key variable for a large range of applications at various spatial and temporal scales, from climate and weather predictions to agriculture, water management, or flood monitoring (*Prigent et al.*, 2005).

2.2.2. Definition and important terms

In this section some definitions and important terms in connection with soil moisture are given. For further information, reference is made to (*Hillel*, 1998; *Scheffer and Schachtschabel*, 2002).

Soil moisture can simply be described as the quantity of water in a soil. If we consider the soil as a three-component sytem where water and air fill the voids of a solid particle matrix (Fig. 2.2):

$$V_t = V_s + V_f = V_s + V_w + V_a \tag{2.2}$$

with V: volume, t: total, s: solid, f: void, w: water, and a: air, the moisture content can either be expressed in terms of soil volume (volumetric soil moisture):

$$\theta_{Vol} = V_w/V_t \tag{2.3}$$

or mass (gravimetric soil moisture):

$$\theta_{Grav} = M_w/M_s \tag{2.4}$$

where M: mass. The conversion between gravimetric and volumetric soil moisture is based on the densities of the dry bulk material ρb and water ρW as follows:

$$\theta_{Vol} = \theta_{Grav} * \rho b/\rho W \tag{2.5}$$

with

$$\rho b = M_s/V_t = M_s/(V_s + V_a + V_w) \tag{2.6}$$

An important term is the porosity η, which is an index of the relative pore space in a soil:

$$\eta = V_f/V_t = (V_a + V_w)/(V_s + V_a + V_w) \tag{2.7}$$

Its value generally ranges from 0.3 to 0.6. Coarse-textured (sandy) soils tend to be less porous than fine-textured (clay) soils, though the mean size of individual pores is greater in the former.

Soil texture is one of the most important soil properties, particularly when dealing with water movement through the soil. It denotes the relative proportions of the three particle

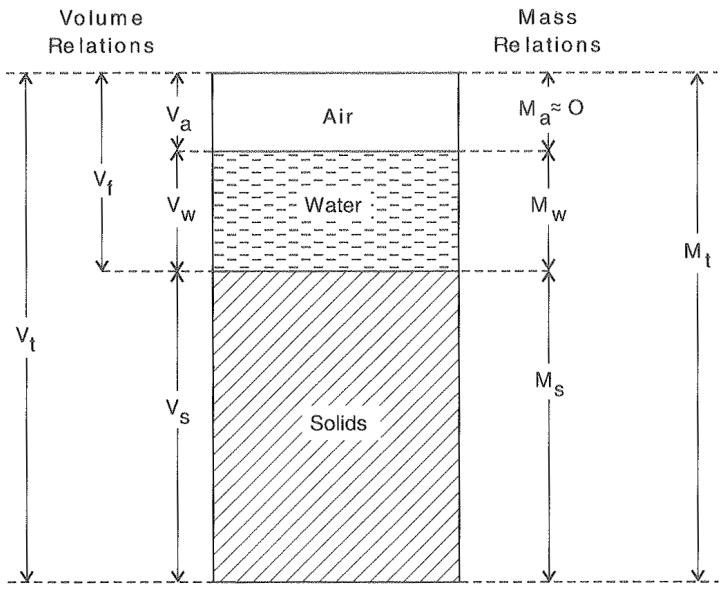

Figure 2.2.: Schematic diagram of the soil as a three-phase system (source: *Hillel*, 1998).

diameter size ranges (textural fractions), sand, silt and clay, of the soil material. The conventional definition of the latter includes particles < 2 mm, while larger particles are considered as rock fragments. Unfortunately, several differing soil texture classification schemes exist. Generally, in Denmark the one of the International Soil Science Society (ISSS) is applied, so that it was used throughout this dissertation. It defines sand as particles ranging in diameter from 2000 μm (2 mm) to 20 μm, silt from 20 μm to 2 μm, and clay from 2 μm downward. Soil types are usually determined on the basis of the mass ratios of the three textural fractions, illustrated by the textural triangle (Fig. 2.3).

Another important property is the soil structure. It describes the arrangement of the individual soil particles and of the soil pores between them (loose, bound together or aggregated), and determines the pore volume (porosity), the density (compaction) and stability of the soil. This has a major influence on water and air movement, biological activity and root growth. The structure depends on what the soil developed from, and is significantly altered under most forms of cultivation, e.g. plowing, irrigation, etc.

The suction power (or tension) describes a soil's ability to hold water in the soil matrix. It is usually given in pF, which expresses the force with which soil holds water. It is a strong function of the pore size distribution, which depends on soil texture and structure (Fig. 2.4). The Field Capacity (FC) is the maximal amount of water that a soil can hold against gravity, whereas the Permanent Wilting Point (PWP) is the minimal point of soil moisture a plant requires not to wilt. Between these two points the water is plant available.

The water holding capacity of sandy soils is much smaller than the one of clayey soils. Clay minerals have high water-binding capacities leading to a tendency of water logging and bad aeration, and some of the water is bound too tight to be plant-available. These important characteristics as function of soil type are summarized in Fig. 2.5.

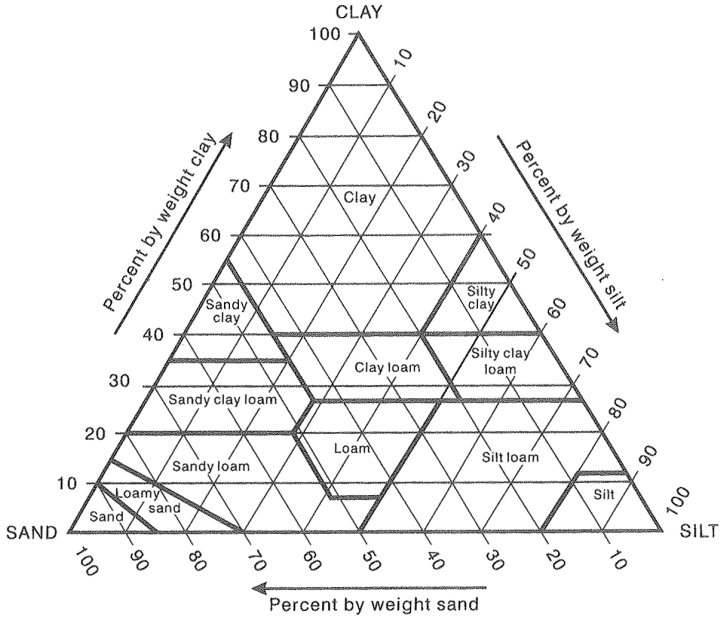

Figure 2.3.: Textural triangle, showing the percentages of clay, silt, and sand (source: *Hillel*, 1998).

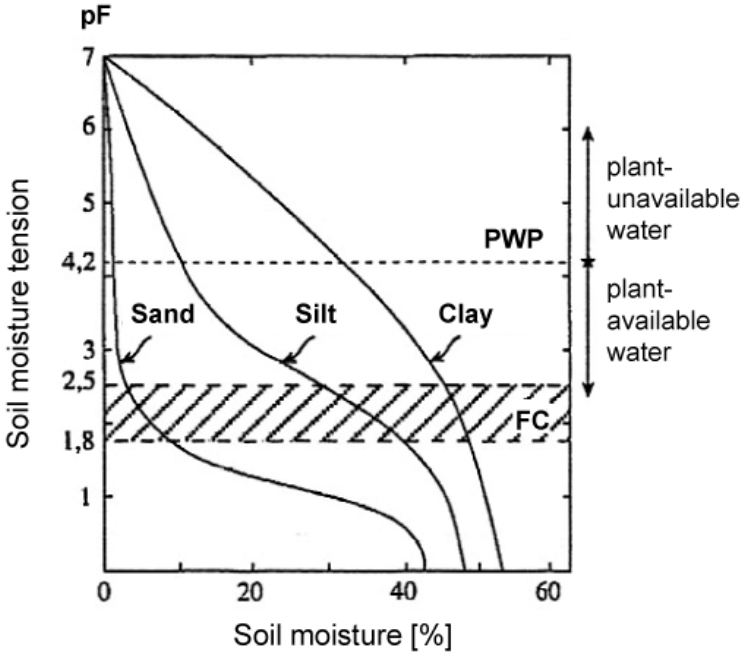

Figure 2.4.: Relation between soil water content [%] and suction power [pF] (water retention) for a sand, silt and clay soil, respectively. FC: Field Capacity, PWP: Permanent Wilting Point (source: adjusted after *Scheffer and Schachtschabel*, 2002).

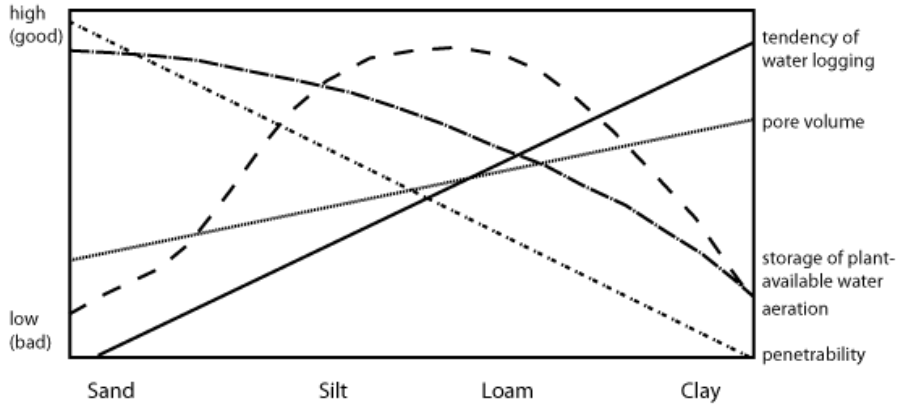

Figure 2.5.: The performance of different soil characteristics (from low/bad to high/good) as a function of soil type (source: after *Ruethnick*, 1998).

Last but not least, organic litter layers on top of soils as well as the organic matter content intermixed in mineral soils are very important properties (*Bot and Benites*, 2005): Plant residues that cover the soil surface protect the soil from sealing and crusting by raindrop impact, thereby enhancing rainwater infiltration and reducing runoff. Organic matter affects both the chemical and physical properties of the soil and its overall health. It influences soil structure by an enhanced stability of soil aggregates and pores through bonding/adhesion of particles and increases diversity and activity of soil organisms, and nutrient availability. Furthermore, and very importantly, organic matter increases the soil moisture holding capacity by increasing the soil porosity as well as (like in case of clay minerals) through high water-binding capacities of humic substances. (*Miller*, 1977) stated that typically 1-3 kg/m^2 of liquid water are stored in a medium dense forest vegetation, and a like amount can be retained on the forest floor. (*Helvey and Patric*, 1965) reported that the water storage capacity of the forest floor can be 135-170% of the weight of the forest floor litter.

2.2.3. Spatial variability of soil moisture across scales

A precondition to successfully model and monitor soil moisture across spatio-temporal scales is profound understanding of the interrelationship between scale and variability. Thus, in the following, first an introduction into the spatial and temporal variability of soil moisture and its influencing factors and processes is given. Afterwards, soil moisture variability is discussed in the context of scale.

Soil moisture influencing factors and processes

Soil moisture is highly variable both in space and time as a result of both temporal dry-down dynamics (*Peters-Lidard et al.*, 2001) and spatially variable land surface properties. The latter are natural and anthropogenic factors. All of them exhibit spatial correlations to some degree, which in turn introduces spatial correlations into the soil moisture pattern (*Western et al.*, 2002). Detailed reviews on relevant literature with respect to the influence of these factors on soil moisture are for instance given by *Famiglietti et al.* (1998) and *Mohanty*

and Skaggs (2001), and if not otherwise stated, the following illustrations are resumed from these articles.

The natural factors are namely soil properties, land cover/vegetation, climate/meteorological conditions, and topography:

With respect to soil properties, the important influence of a broad range of factors, such as the parent material (geology), soil texture, structure and organic matter content has already been pointed out in the preceding section. They determine the saturated moisture content and, in conjunction with the vegetation, the wilting point (*Western et al.*, 2002). Furthermore, the soil depth naturally influences the amount of water that can be stored and soil color has an impact on the albedo and thus, the rate of evaporative drying.

Vegetation influences soil moisture variability by the pattern of throughfall imposed by the canopy, by shading the land surface and affecting the rate of evaporative drying, by generating turbulence and enhancing evapotranspiration rates, by affecting soil hydraulic conductivity through root activity and the addition of organic matter to the soil surface layer, and by extracting moisture for transpiration from the soil profile - the degree, to which these factors affect the soil moisture distribution, varies with vegetation type, density and season.

Climate forcings for soil moisture are primarily precipitation, solar radiation, wind, humidity, and temperature. Variations in the latter four affect soil moisture through the evapotranspiration process (*Western et al.*, 2002). However, the frequency, duration and intensity of precipitation are the most important influencing contributors to soil moisture variability. (*Famiglietti et al.*, 1999) found for instance a distinct trend in mean soil moisture with a south-to-north precipitation gradient. An important point is that rainfall occurs at a range of spatial scales with different impact. This will be further discussed in the subsequent section.

Important topographical parameters are mainly slope, aspect, curvature, specific contributing area, and relative elevation. They affect slope infiltration, drainage and runoff and thus, soil moisture variability. Steeper slopes are likely to be drier than flat areas owing to lower infiltration rates, rapid subsurface drainage, and higher surface runoff. Aspect influences solar irradiance and thus evapotranspiration and soil moisture. Curvature influences the convergence of lateral flow. Depressions with high curvature tend to be wetter than planar areas with low curvature. The specific contributing area, that drains through a unit length of contour on a hillslope, influences soil moisture distribution by controlling the potential volume of subsurface moisture flowing past a particular point on the landscape.

The relative importance of the individual influencing factors depends on local conditions. The influences of vegetation and climate on soil moisture are more dynamic compared to soil and topographic factors. (*Famiglietti et al.*, 1998) for instance found in a study on the influence of topography and soil properties on a hillslope transect with consistent vegetation and precipitation that dominant influence on soil moisture variability gradually changed from soil heterogeneity to joint influence by topography and soil properties as the transect dried following rain events. This suggested that no single predictive index (e.g. topographic wetness index) can be expected accurately to predict surface moisture content throughout an entire dry down sequence - rather, different predictive indices for wet versus dry conditions may be required.

The anthropogenic factors are mostly agricultural practices, such as irrigation and tilling. The latter, for instance, affects both the magnitude and variability of soil properties, be-

cause it physically disrupts the structure of the soil and causes changes in water and solute flow patterns (*Coquet et al.*, 2005). This may change again with time as soil settles and continuous macropores develop through active soil biota and/or by physical processes, such as freezing/thawing or wetting/drying (*Corwin et al.*, 2006). Appropriate soil management can improve the water holding capacity. *Bot and Benites* (2005) for example stated that conserving fallow vegetation as a cover on the soil surface, and thus reducing evaporation, can result in four percent more water in the soil, which can make the difference between wilting and survival of a crop during temporary dry periods.

Soil moisture variability in context of scale

The variability of soil moisture and its influencing factors exist across different scales. This, and the fact that many moisture dependent processes are nonlinear, lead to complex scale effects. These complicate the comparison of data sets, such as ground measurements and satellite observations across scales, where it is necessary to aggregate in space and/or time. (*Western et al.*, 2002) give a good overview of relevant work about this topic, and if not otherwise stated, this section is based on their article.

In order to compare soil moisture variability across scales, one is interested in knowledge on the spatial and temporal arrangement of soil moisture. To specify the spatial dimensions of measurements, *Bloeschl and Sivapalan* (1995) suggested a scale triplet, composed of spacing (distance between measurement points), extent (overall coverage), and support (integration volume/area). If spacing, extent and support are chosen in a reasonable way, the observed data can be used to estimate spatial and temporal correlations, and the scale on which they prevail. The concept of spatial/temporal correlation is based on the assumption of soil moisture being a random field with a given probability density function and a given correlation structure. The observed soil moisture field is then one out of many possible realizations of that random field, and instead of attempting to quantify the actual pattern of soil moisture, one quantifies the spatial statistical structure, usually represented as a variogram. The variogram is a plot of the variance of soil moisture differences between two points as a function of the spatial or temporal distance (lag) between them. As two locations at short distance tend to have rather similar soil moisture values, the variogram value increases with increasing lag. The shape of the variogram can be described by three parameters, namely the sill, correlation length or range, and nugget, and is tried to be fitted by a smooth function (most commonly exponential). The sill is the level at which the variogram flattens out. If a sill exists, the soil moisture variability is stationary, and the sill can be thought of as the spatial or temporal variance of two distantly separated points. The correlation length and range are measures of the spatial or temporal continuity of soil moisture and can be used to quantify the scale of variability. They relate to the average and maximum distance for which correlation is present, respectively. The nugget relates to the variance between pairs of points separated by very small distances, and can be due to either sampling error, short scale variability, or both.

Western and Bloeschl (1999) analyzed scale effects on the variance and correlation length by means of a small, densely-instrumented catchment with a very large number of soil moisture samples. In a first step they acquired a 'true' variogram from the full data set, while in a consequent step they resampled the data for the estimation of apparent variograms for different scales. The authors found that for the ideal case of very small spacings, very

large extents and very small supports, the apparent variance and the apparent correlation length were close to their true values. However, as the spacing increased, the extent decreased or the support increased, bias was introduced between the true and the apparent variogram: the apparent correlation lengths always increased with increasing spacing, extent or support, while the apparent variance increased with increasing extent, decreased with increasing support, and remained unchanged with varied spacing. The authors pointed out that these biases were a function of the ratio of the measurement scale and the scale of natural variability. This stresses the importance of a good sampling design, if one wishes to assess the natural soil moisture variability.

Generally, it was shown that the soil moisture variations in space and time, and the respective range of influencing factors can be related to a small scale and a large scale component (*Hu et al.*, 1997; *Entin et al.*, 2000; *Vinnikov et al.*, 1996). *Western et al.* (2002) gave an overview over studies on soil moisture correlation scales. Most studies focused on small scales (test sites of few m^2 to some km^2), while only a small number of studies addressed larger scales.

Famiglietti et al. (1998) and *Western et al.* (1998) reviewed small-scale studies on the near-surface soil moisture variability which showed very inconsistent results. More recent small-scale studies more clearly demonstrated the existence of stationarity with correlation lengths in the order of tens to few hundreds of meters spatially and in the range of a few days temporally (e.g. *Western et al.*, 1998; *Mohanty et al.*, 2000; *Western et al.*, 2004). Large (global) scale studies also revealed stationarity in soil moisture variation. *Vinnikov et al.* (1996) and *Entin et al.* (2000) both observed spatial correlation lengths of soil moisture in the order of several hundred kilometers for an extensive in situ data set in Russia and a global network of test sites in Russia, Mongolia, China, and the USA, respectively. The former further reported a temporal correlation scale of about 2 - 3 months. Nonstationary behavior of soil moisture has been suggested for intermediate scales, but this finding is mainly based on one remotely sensed data set (*Rodriguez-Iturbe et al.*, 1995; *Hu et al.*, 1997; *Peters-Lidard et al.*, 2001). *Vinnikov et al.* (1996) and *Entin et al.* (2000) noted the existence of a smaller scale (< 50 km) component to the spatial variability that was unresolved by their data.

The discrepancies in these findings are likely to be attributed to sampling effects, e.g. different sampling scales and spacings, different measurement techniques and depths as well as uncertainty in the sample variograms due to small sample sizes. But they are probably also caused by differences in environmental conditions between the study areas and important related process controls of the previously mentioned soil moisture influencing factors. The scale at which the latter are acting is of high importance for the prevailing soil moisture patterns (*Western and Bloeschl*, 1999). *Kim and Barros* (2002) presented a study that exemplary demonstrated the complexity of soil moisture patterns as a result of the impact of several environmental factors acting at a range of different spatial and temporal scales. Generally, they suggested a strong connection to soil texture indices. However, after rainfall events the spatial correlation structure of soil moisture was similar to that of rainfall and topography. Then, as the landscape became increasingly drier, it approached first the spatial correlation structure of sand content, and next that of clay content and vegetation water content, when soil moisture levels were close to, or below, field capacity.

Soil properties, land cover attributes and local topography lead to small scale variations in soil moisture (*Robock et al.*, 1998; *Entin et al.*, 2000; *Western et al.*, 2004). At intermedi-

ate scales *Robock et al.* (1998) and *Entin et al.* (2000) expect that soil characteristics and vegetation may play a significant role; however, this has not been fully analyzed to date. Large-scale variations are related to atmospheric forcings, namely precipitation and evaporation processes (*Robock et al.*, 1998; *Entin et al.*, 2000). Variations in rainfall also occur at small spatial scales due to the passage of storm cells. However, the long-term effect on soil moisture variability is most likely found at larger spatial scales, as the soil store integrates precipitation over time, and thus smoothes some of the spatial and temporal variation in instantaneous rainfall rates. At still larger scales, climatic variations in precipitation lead to substantial changes in general soil moisture conditions between climatic regions (*Western et al.*, 2002). Similarly, *Entekhabi* (1995) pointed out that the correlation timescales for soil moisture were much longer than for precipitation due to the 'memory' of the soil moisture store, which smoothes out the relatively rapid variations in precipitation.

In this context, a couple of studies have emphasized the existence of seasonal character of soil moisture patterns. Seasonal changes were found to occur in the spatial soil moisture variance and correlation lengths at both small and large scales associated with changes in the processes controlling the soil moisture pattern. *Western et al.* (1998) for instance found the geostatistical structure in their investigated small-scale soil moisture data set to evolve seasonally with high sills and low spatial correlation lengths during the wet winter period and smaller sills and longer spatial correlation lengths during the dryer summer period. *Entin et al.* (2000) stated that temporal scales increased with latitude and in winter, which he attributed to changes in the potential evapotranspiration. Supporting the findings of *Robock et al.* (1998) and *Entin et al.* (2000), *Woods et al.* (2001) found the main driver for seasonal soil moisture variability to be the seasonal changes in the balance between potential evapotranspiration and precipitation. Superimposed on this seasonal cycle was a series of wetting and drying events with time scales related to storm duration and inter-storm period, respectively. The same had already been discovered by *Grayson et al.* (1997) who stated that there is a seasonal shift between two states in the temporal distribution of soil moisture: where potential evapotranspiration dominates over precipitation and vice versa, soil moisture tends to be consistently low/high, respectively. They further noted that in landscapes with significant lateral movement of water, this temporal behavior corresponded with a change in controls on the spatial soil moisture pattern, from being dominated by local vertial fluxes during the dry state to being dominated by lateral fluxes during the wet state.

2.2.4. Soil moisture measurements

A thorough review on soil moisture measurements is presented by *Robinson et al.* (2008). Several physical properties can be used to determine water content by a vast range of measuring techniques. Here, only the ones relevant for this work are mentioned.

Generally, soil moisture is quantified by either gravimetric (g/g) or volumetric measurements (m^3/m^3). The former are conducted by soil sample taking and estimation of the wet weight as well as dry weight after oven drying at 105 °C. Knowing the volume of the sample, the volumetric water content can be calculated from the gravimetric water content using 2.5. As the sampling is labor-intensive, these measurements are mostly used for the calibration of soil moisture sensors. There is a variety of such sensors, whereof the most common ones make use of the dielectric properties to measure volumetric water content.

The method is based on the large permanent dipole of water (displacement of positive and negative molecular charge due to the position of the hydrogen atoms in relation to the oxygen atom), resulting in a significantly higher dielectric constant (relative permittivity) compared to most other natural materials. Therefore, the proportion of water strongly affects the measured bulk permittivity of a soil. The latter is a composite value of the soil's components, air, solid particles and water, and several so-called dielectric mixing models exist to estimate soil moisture from it (e.g. *Wang and Schmugge*, 1980; *Topp et al.*, 1980; *Dobson et al.*, 1985; *Roth et al.*, 1990; *Mironov et al.*, 2004).

In addition to in situ sensors, this principle is also applied to indirectly assess soil moisture by means of air- and spaceborne remote sensors. in situ measurements and remote sensing are two methods that are in many ways complimentary. Ground measurements provide continuous long-term records at high temporal resolution. They can be applied over any depth, accurately calibrated, and logged at any time scale, which is important to study and improve our understanding of small-scale hydrologic processes in the soil. However, the restriction to single points, and in accessible areas only, makes spatial interpretation difficult (*Western et al.*, 2002). Also, it is an invasive approach, where the soil is damaged during the measurement. Meanwhile, airborne remote sensors are able to deliver data with blanket coverage at spatial resolutions of few kilometers. However, such airborne data is limited in spatial extent, complex to process due to significant attitude variations during data acquisition, and only gives insight into snapshot soil moisture conditions in time due to very high costs. Only spaceborne remote sensors have the capability of long term observations with global coverage, and are the only means of providing observations for areas that are in a hydrological context unexplored. This is crucial for the global monitoring of water resources and climate, as well as for respective model predictions. But as for airborne sensors, they suffer from the indirect nature of the method and from a shallow measurement depth limited to the surface layer. Furthermore, the use of spaceborne sensors for soil moisture acquisition is limited by the short life span of a single satellite mission (couple of years), and the coarse spatial resolution of the available data (some tens of kilometers). The development of disaggregation and data assimilation methods is important. Furthermore, the satellite data needs to be validated by means of direct measurements in the ground. Thereby, airborne data can be supportive in that it provides a link between the in situ point and satellite large spatial scale.

2.3. Remote Sensing

2.3.1. Basics

In this section a basic introduction into remote sensing, and more specifically, into the remote assessment of soil moisture, is given. The information is extracted from several textbooks (*Ulaby et al.*, 1981, 1982, 1986; *Albertz*, 2001; *Woodhouse*, 2006) to which reference is made for more details.

Each body with a temperature above the absolute zero emits electromagnetic radiation (energy) over the entire electromagnetic spectrum. This energy can be measured by means of sensors on ground-based platforms, airplanes or satellites. Such data acquisition, where the sensing device is not in physical contact with the observed object or phenomenon, is called remote sensing.

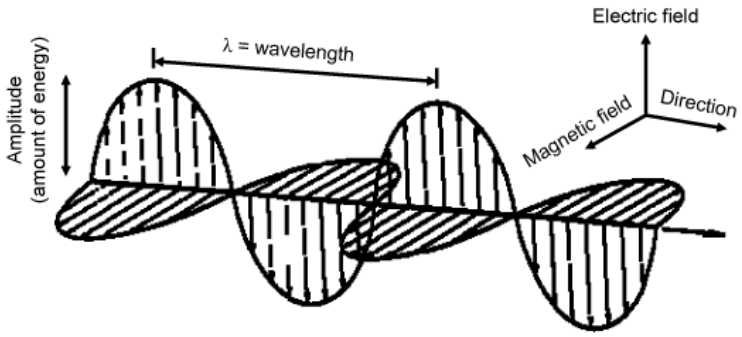

Figure 2.6.: Schematic illustration of an electromagnetic wave (source: after *Kraus*, 1988)

Electromagnetic radiation propagates as waves at the speed of light c ($2.99792458 \cdot 10^8$m/s), with:

$$c = \lambda * \nu \tag{2.8}$$

where λ: wavelenght and ν: frequency. These waves are composed of an electric and a magnetic field component, oscillating in phase perpendicular to each other as well as perpendicular to the travel direction (Fig. 2.6). The amplitude denotes the amount of transported energy.

An important property of electromagnetic waves is polarization. It indicates the direction in which the oscillations are taking place. If the direction of propagation is along the Z-axis, the wave having only Y-displacement is said to be polarized in the Y-direction, and the one with only X-displacement polarized in the X-direction. Instead of X and Y, often the letters H (for Horizontal) and V (for Vertical) are used, respectively.

The electromagnetic spectrum spans from X-rays via Ultraviolet Radiation (UV), visible (VIS), Near, Medium and Thermal InfraRed (NIR, MIR, TIR) to Micro- (MW) and Radio Waves with increasing wavelengths and decreasing frequencies and energy E (Fig. 2.7):

$$E = h * \nu \tag{2.9}$$

where h: Planck constant ($6.626068 \cdot 10^{-34}$m^2 kg/s). The microwave section of the spectrum is further divided into several wavelength/frequency bands (Table 2.1).

According to Planck's law, the respective distribution of emitted radiation over the spectrum is a function of body temperature - the warmer the body, the more is the maximum of radiation shifted towards shorter wavelengths. For example, the sun with a temperature of 6000 K has its maximum in the visible domain of the spectrum, while the one of the earth with a temperature of around 300 K is located in the thermal infrared (Fig. 2.7).

As electromagnetic waves travel, they collide with atoms and molecules (Fig. 2.8). These become small electromagnetic osciallators, which (1) absorb and emit the waves (transformation into other energy forms such as heat) and (2) reflect and scatter them in all directions (forcing them to deviate from a straight trajectory), while (3) parts of the wave might simply be refracted and travel through the medium (transmission, Fig. 2.9).

Table 2.1.: Designation of microwave bands. γ: wavelengths [cm], ν: frequency [GHz] (source: after *Loeffler*, 1985).

Band	γ [cm]	ν [GHz]
Q	0.8–0.6	40–50
Ka	1.2–0.8	26–40
K	1.7–1.2	18–26
Ku	2.4–1.7	12.5–18
X	3.8–2.4	8–12.5
C	7.5–3.8	4–8
S	15–7.5	2–4
L	30–15	1–2
P	100–30	0.3–1.0

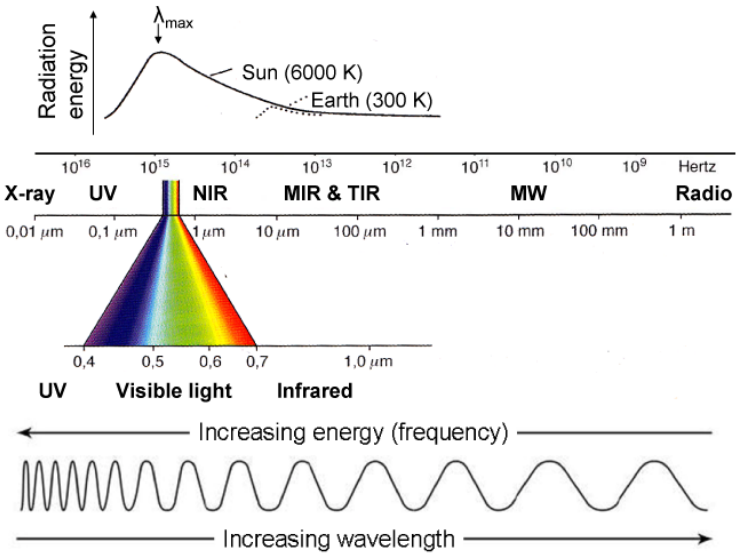

Figure 2.7.: The electromagnetic spectrum with designation of individual spectral regions, corresponding wavelengths [μm–m] and frequencies [Hz], and distribution of radiation energy of sun and earth over the spectrum. UV: UltraViolet, NIR: Near InfraRed, MIR: Middle InfraRed, TIR: Thermal InfraRed, MW: MicroWave (source: after *Albertz*, 2001).

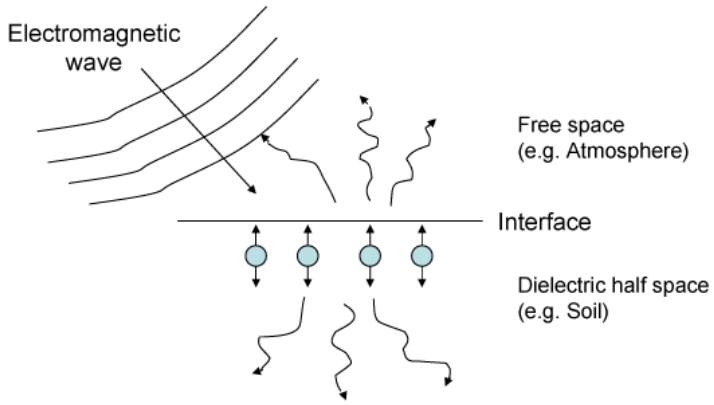

Figure 2.8.: An incident wave on a dielectric half-space excites the dielectric atoms, which become small oscillating dipoles (source: after *Elachi and van Zyl*, 2006).

The reflectivity Γ is the fraction of the incident radiation reflected by a surface, while the emissivity e is the ratio of energy emitted by a material's surface and the one radiated by a black body (optimal absorber/emitter) at equal temperature. These mechanisms are especially pronounced at interfaces separating two media of different electric or magnetic properties, for example at the boundary between the atmosphere (free space) and the soil (dielectric half space). They can be summarized as following:

$$i = \Gamma + tr + e \tag{2.10}$$

where i: incident electromagnetic wave, and tr: transmitting part of wave. Note, that for $tr = 0$:

$$e = 1 - \Gamma \tag{2.11}$$

The way a wave is scattered at a boundary depends on its roughness. In case of a perfectly smooth surface, the wave is reflected at an angle of the same size as the incidence angle, referred to as perfect specular (mirror-like) reflection. As the surface becomes slightly rough, the mirror-like reflection is still the preferred scatter direction, but now there are also scatter components pointing in other directions (near-perfect specular reflection). Towards rougher conditions, the fraction of perfect reflection diminishes gradually while the scattering in all directions becomes more and more pronounced (near-perfect diffuse reflection). Finally, for very rough surfaces the scattering is equally distributed in all directions. Such surfaces are called perfect diffuse reflectors or Lambertian surfaces (Fig. 2.10).

The wave-particle interaction always depends on (1) the incidence angle of the wave, (2) the surface roughness-wavelength relation, (3) and the scatterer size-wavelength relation. Each of the factors is illustrated in the following.

Fig. 2.11 depicts reflectivity and emissivity of a wave travelling from free space to a medium with a dielectric constant of 3.2 as a function of the incidence angle θ for both polarizations. Between 0 and 60° θ the reflectivity/emissivity is increasing/decreasing for the H-polarized

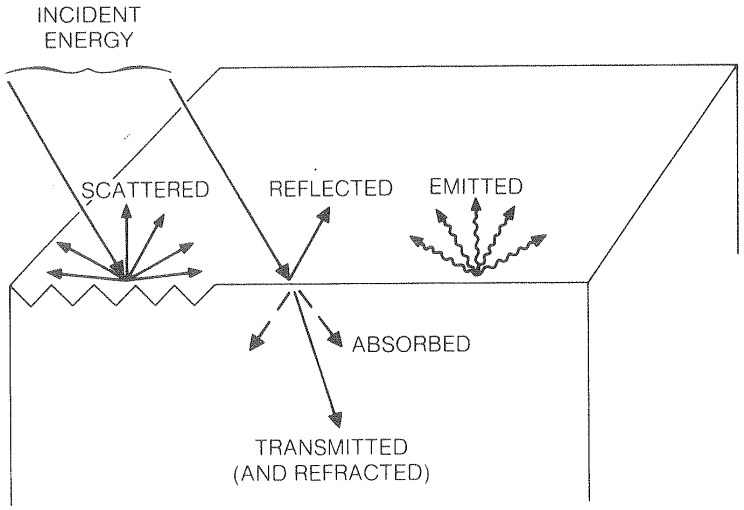

Figure 2.9.: Interaction processes between electromagnetic energy and matter: An electromagnetic wave incident on a dielectric half-space is reflected/scattered, transmitted/refracted and absorbed/emitted (source: *Sabins*, 1996).

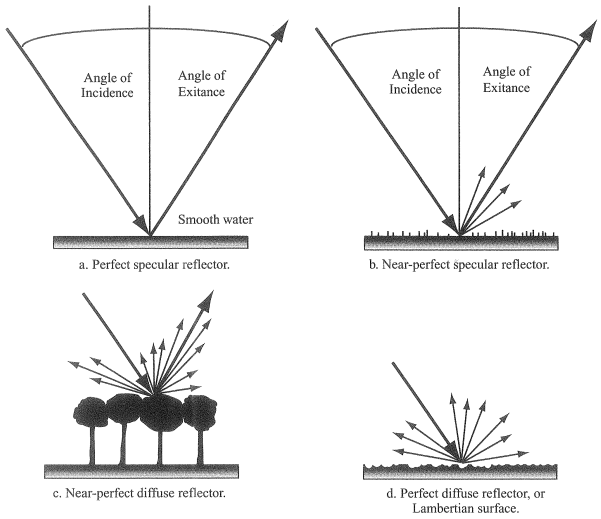

Figure 2.10.: Scattering types as a function of surface roughness (source: *Jensen*, 2007).

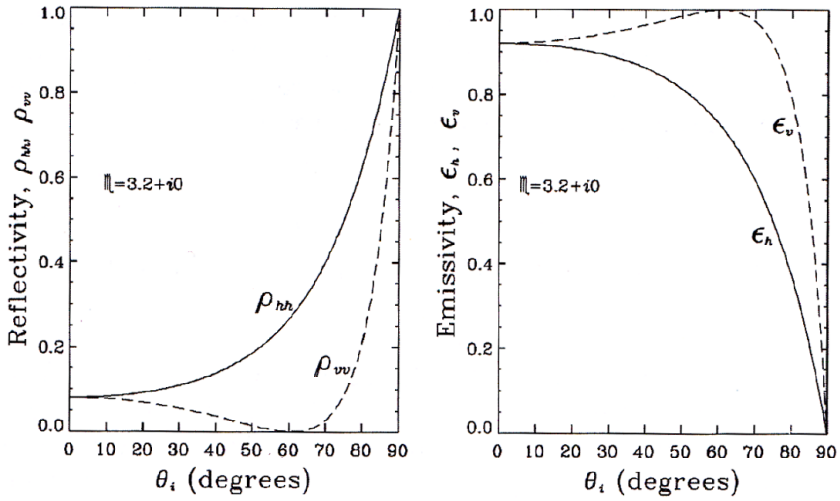

Figure 2.11.: Reflectivity and emissivity as a function of incidence angle θ_i for a wave travelling from free space to a medium with dielectric constant $\varepsilon = 3.2$ (source: *Woodhouse*, 2006).

wave and vice versa for the V-polarized wave. At larger incidence angles, both polarizations show an increase in reflectivity and a decrease in emissivity.

Whether a surface is considered rough, and thus, what type of scattering occurs, depends on the incidence angle as well as the wavelength of the incident wave. According to the Rayleigh criterion:

$$S_D < \lambda/(8cos\theta) \tag{2.12}$$

where S_D: standard height deviation (root mean square deviation of the mean height). This implies that the longer the wave, the rougher the surface must be to impact the ideal (specular) scattering.

Furthermore, the relation between the particle size and a wave's length determines whether an interaction, and thus, scattering takes place. This is shown in Fig 2.12 at the example of three microwaves from different bands travelling through a vegetation canopy and glacier ice. In case of the canopy, the X- and C-band waves of 3 and 5 cm wavelengths, respectively, are sooner or later totally scattered by leaves and small branches of corresponding size, so that they do not reach the ground at all. Meanwhile, the L-band wave of around 23 cm is scattered by larger branches as well as the stem. However, parts of the wave are able to reach the ground and reflect a signal from it. Likewise, the penetration depth in glacier ice is enhanced, the larger the wavelength. It is self-evident, that the polarization of the wave, and hence, the way it encounters a medium, also has a strong impact on the form of interaction between the two.

Generally, waves with shorter wavelengths (higher energy) are more easily measurable, especially from such large distances as in case of spaceborne remote sensors. However, on the way through the atmosphere the radiation is attenuated by scattering and absorption through H_2O, O_2, O_3 and CO_2 molecules over a large part of the electromagnetic spectrum.

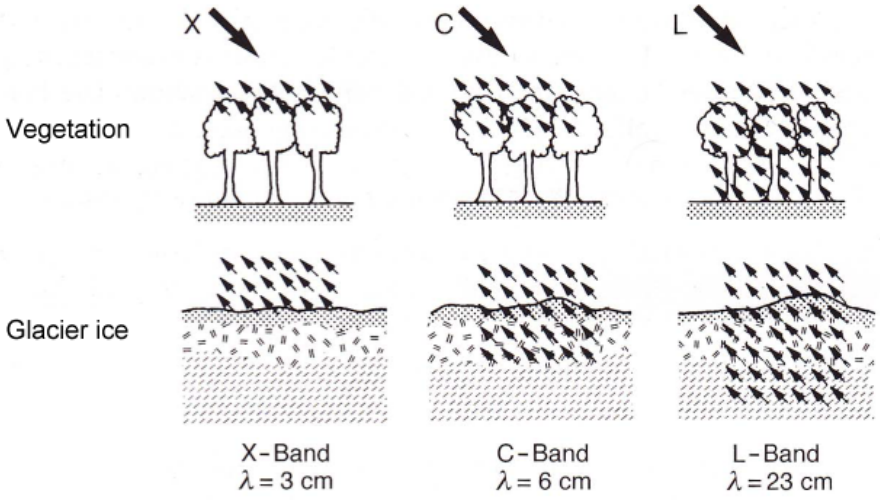

Figure 2.12.: Schematic illustration of microwave penetration depths as a function of wavelength λ (source: *Albertz*, 2001).

The atmospheric impact can solely be ignored in the microwave domain (unless in case of heavy rain), while at higher frequencies spaceborne measurements are limited to certain 'observation windows' (Fig. 2.13). Naturally, in case of the visible domain, fog and drizzle increase the attenuation, and there are daylight restrictions.

Resolution is an important term in remote sensing. It can be described as the ability to decompose values of equal dimension in distinguishable elements. For example, spatial resolution is a measure of how close objects can be to each other to still be visibly resolved. For a given sensor type, this is determined by the size of its footprint, i.e. the area of a pixel observed at one point in time. The spectral resolution gives an indication on the ability to separate frequency ranges, while the radiometric resolution describes the capacity of a detector to discriminate between the measured values. The temporal resolution gives the time span between two consecutive measurements.

A detecting instrument measures the incident power (energy per unit time in Watts [W]), given by the square of the wave's amplitude. The energy is received by the antenna of the instrument, which is pointed towards the object under investigation. The major part of the signal is caught from an area with a certain opening angle (beamwidth) around the pointing direction of the antenna, called the main lobe. The width of the main lobe, where half of the power originates from is known as the half-power or -3 dB beamwidth. Even though antennas should optimally solely receive power from the main lobe, practically, some signal contributions always originate from other directions as well, referred to as side- and back lobes.

In remote sensing two types of sensors exist: Passive sensors such as radiometers are receivers that catch naturally reflected and emitted radiation, while active sensors such as radar systems send pulses and again receive the reflected signal. In case of the latter, scatterometers and Synthetic Aperture Radar (SAR) constitute two different measuring

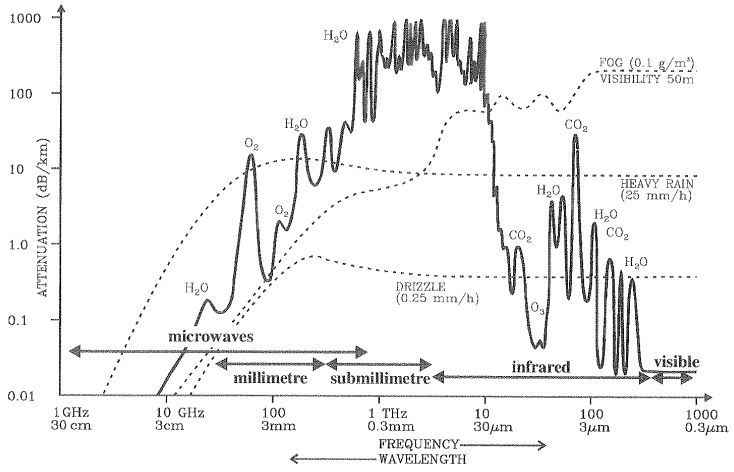

Figure 2.13.: The attenuation of the atmosphere for a nominal clear atmosphere, with additional attenuation shown for fog, heavy rain and drizzle. Notice that the regions used most often for terrestrial remote sensing are in the 'windows' (visible, infrared and microwave) (source: *Woodhouse*, 2006).

techniques. Radiometers and scatterometers are 'natural' antennas where the spatial resolution depends on (1) the distance between object and sensor, and (2) the antenna size. The larger the antenna is, the smaller the beamwidth and the higher the resolution. Consequently, the spatial resolution is restricted by technical limitations of the antenna size for the large observation distances (∼700-900 km) of spaceborne sensors.

In turn, the 'synthetical' antennas of SAR sytems jointly process many returning wave pulses received from different antenna positions during the sensor movement. Thus, objects are synthetically resolved at a much higher spatial resolution than naturally possible at a given antenna size. In other words, a large synthetic aperture with a small real antenna results in a small synthesized footprint, i.e. a high resolution. A drawback of spaceborne SAR systems are usually low temporal repetition rates.

2.3.2. Remote sensing of soil moisture

Reviews on surface soil moisture retrieval from remote sensing were made by (*Jackson et al.*, 1996; *Wagner et al.*, 2007; *Kerr*, 2007).

Theoretically, soil moisture information can be acquired over the entire range of the electromagnetic spectrum: in the visible and thermal infrared domains distinctions can be made by the soil color (darker when wet) and temperature (wet soils cooler than dry soils), respectively. However, for the monitoring of a highly temporally variable component such as soil moisture, day-light and weather restrictions constitute a serious drawback. Thus, observations in the microwave domain are most suitable.

As already described in Section 2.2.4, the measurement principle is based on the relative permittivity (dielectric constant) ε, which is a strong function of water content in this range of the electromagnetic spectrum. The dielectric constant is a complex number that describes

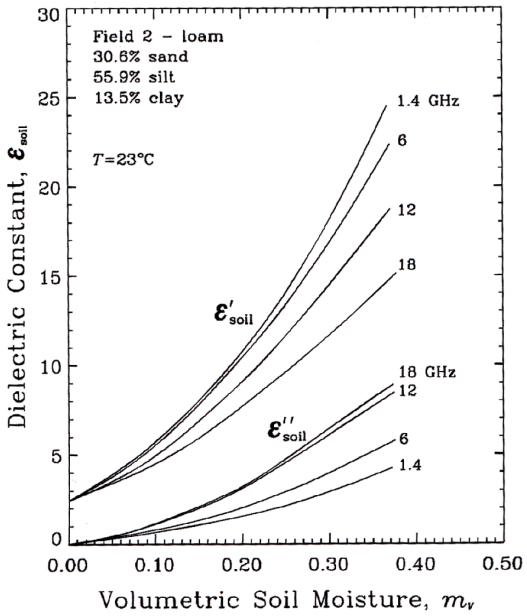

Figure 2.14.: Measured dielectric constant as a function of volumetric moisture content for a loamy soil at four microwave frequencies (source: *Ulaby et al.*, 1986).

how much an electric field of an electromagnetic wave interacts with the medium it travels through. Its real part ε' represents the ability of the material to polarize in response to the electric field compared to the free space (air, with ε=1), while the imaginary part ε'' is the ability of the medium to absorb the wave. The dielectric constant is a function of frequency with an increasing strength of the water content-dependency with decreasing frequency as shown in Fig. 2.14. At the 1.4 GHz frequency (microwave L-band) the dielectric constant of dry soil is around 4 while the one of pure water is approximately 80. Furthermore, signal attenuations by influences of surface roughness as well as vegetation and atmospheric water are minimized at small frequencies (Fig. 2.15). At the same time the penetration/emission depth is generally increasing with decreasing frequency (Fig. 2.16). However, with respect to the latter, it is again a function of water content and decreases with increasing dielectric constant/moisture of the medium. *Laymon et al.* (2001) found penetration/emission depth of 3 - 5 cm in the 1.4 GHz domain for soil water contents below 0.3 m^3/m^3, and less at higher moisture values, while *Raju et al.* (1995) and *Escorihuela et al.* (2010) described it generally to be more around 2-2.5 cm at this frequency. All the above and the fact that the 1.4 GHz frequency is a protected band for scientific exploration renders it an optimal frequency for soil moisture assessment from space.

In case of passive sensors, the provided measurements are brightness temperatures T_B, which are directly proportional to the received electromagnetic radiances in the microwave domain of the spectrum (Rayleigh-Jeans Law). These measurements include contributions from the atmosphere, reflected cosmic radiation and the land surface. As already indicated,

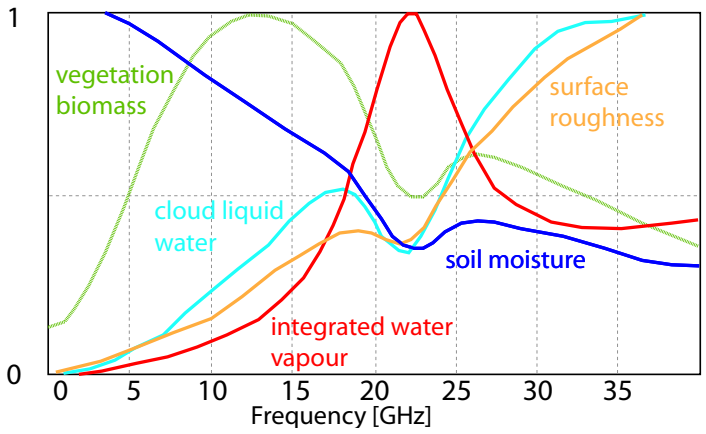

Figure 2.15.: Electromagnetic signal attenuations (0 = none, 1 = total) by different components as a function of frequency [GHz] (source: *Kerr*, 1996)

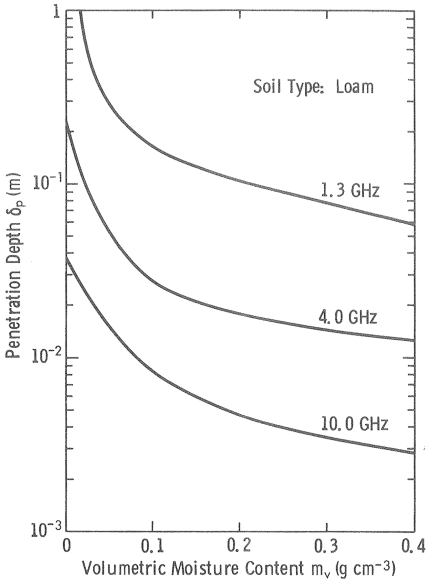

Figure 2.16.: Penetration depth of loamy soil as a function of moisture content (source: *Ulaby et al.*, 1982).

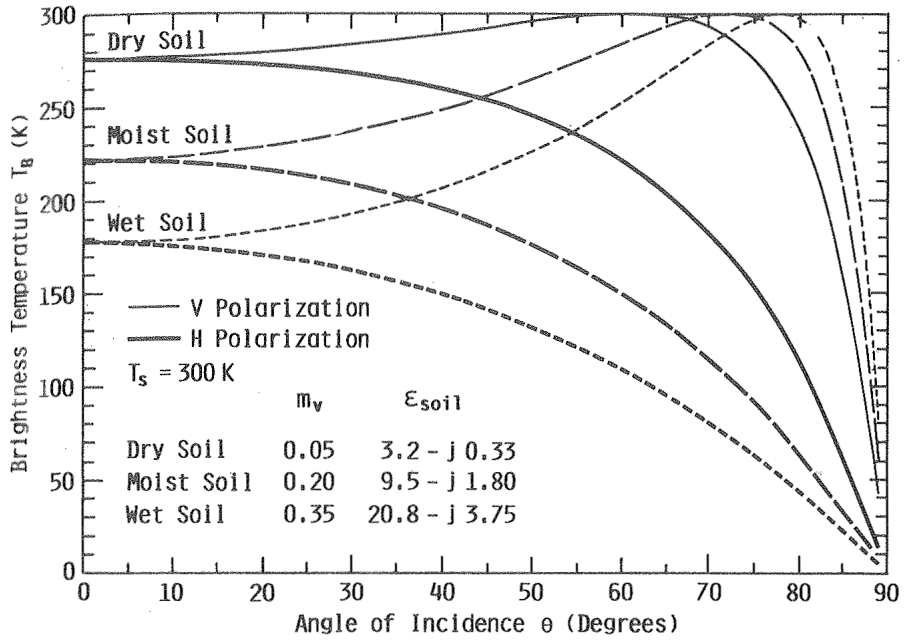

Figure 2.17.: Calculated brightness temperature for a homogeneous soil medium with a specular surface at three moisture conditions (source: *Ulaby et al.*, 1986).

atmospheric contributions are negligible at wavelengths > 5 cm, while cosmic radiation has a known value. Brightness temperature can be expressed as:

$$T_B = e * T \tag{2.13}$$

where e: emissivity and T: physical temperature. If T is estimated independently, e can be determined. Generally, 2.11 holds at these wavelengths. In turn, the reflectivity is linked to the dielectric constant through the Fresnel equations, when primarily segregating the contributions of vegetation and surface roughness. And as described in Section 2.2.4 soil moisture can be derived from the dielectric constant by means of a dielectric mixing model. Fig. 2.17. shows brightness temperatures for H and V polarization measured across a range of incidence angles for different soil moisture contents.

Active radar systems (SAR and scatterometers) measure the backscattering coefficient σ°, which can be related to the surface reflectivity. In the same way as described for the passive measurements, soil moisture can be estimated therefrom. The backscatter of active radar systems is highly influenced by surface roughness and vegetation (structure and water content), which renders soil moisture retrieval complex and error-prone. Furthermore, the above-mentioned low temporal repetition rates constitute a serious drawback for the monitoring of a highly fluctuating variable such as soil moisture. Thus, passive radiometers are currently considered most effective for soil moisture retrieval. They have a much higher sensitivity to soil moisture under vegetated conditions. This results in rather straightforward soil moisture retrieval, which is well established. However, their major limitation is their

Table 2.2.: Overview of characteristics of different space-borne microwave sensor types for soil moisture retrieval (source: after *Kerr*, 2007).

	SAR	Scatterometer	Radiometer
Measurement mode	active	active	passive
Spatial resolution	high (tens of m)	low (tens of km)	low (tens of km)
Temporal resolution	low (20–40 d)	high (4–6 d)	high (1–3 d)
SM retrieval	complex	complex	straight forward

coarse spatial resolution. The properties of the different sensor types available for space-borne soil moisture assessment are compiled in Table 2.2.

Fig 2.18 gives an overview of former or currently operating space-borne microwave sensors. Different approaches have been developed to retrieve soil moisture using higher frequencies (5-20 GHz), e.g. SMMR and SSM/I (*Owe et al.*, 2001), AMSR-E (*Owe et al.*, 2001; *Njoku et al.*, 2003), ERS-ASCAT and MeTop-ASCAT (*Wagner et al.*, 1999; *Naeimi et al.*, 2009). Despite the higher sensitivity to vegetation growth, atmosphere and roughness effects, they remain a valuable time series for the period 1978 until now (*Leroux et al.*, Submitted).

Launched in November 2009, the first space-borne passive microwave radiometer operating at the preferred frequency for soil moisture retrieval (1.4 GHz, 21.4 cm λ) is the Soil Moisture and Ocean Salinity (SMOS) mission (*Kerr et al.*, 2001, 2010). It is specifically designed for

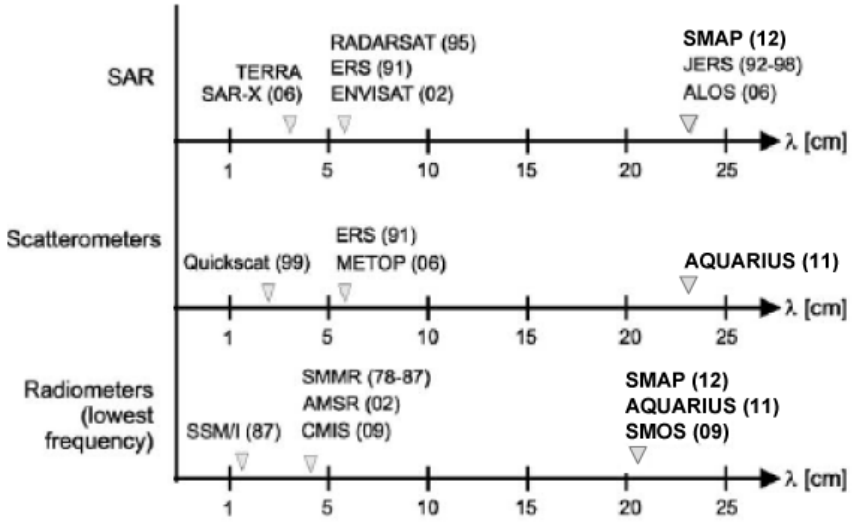

Figure 2.18.: Overview of available spaceborne microwave sensors (year of launch) at different wavelengths λ divided into the three sensor type categories Synthetic Aperture Radar (SAR), scatterometers and radiometers. Please note that radiometers have generally channels over the entire microwave range, while only the lowest frequency channel is indicated here (source: adjusted after *Wagner et al.*, 2007).

the monitoring of surface soil moisture at a spatial resolution of ∼44 km with global coverage every 3 days. The goal is to achieve an accuracy of 0.04 m^3/m^3. The ascending equator-crossing is at 06:00 h in the morning (local time) when air, vegetation and soil are assumed to be in thermal equilibrium. This facilitates soil moisture retrieval.

Very recently, the AQUARIUS satellite was launched with three L-band radiometers (1.413 GHz) as well as an L-band scatterometer (1.26 GHz) on board (*Lagerloef et al.*, 2008). This mission focuses on sea surface salinity. With a repeat cycle of seven days and a spatial resolution of around 100-150 km it might not be fully suited for soil moisture studies.

Another project dedicated to spaceborne soil moisture assessment is the Soil Moisture Active and Passive SMAP satellite, which is scheduled for launch in December 2012. With both, an L-band SAR (1.26 GHz) as well as an L-band radiometer (1.41 GHz) on board, the goal is to jointly process soil moisture at a spatial resolution of 10 km with global coverage every 3 days. This should be achievable by taking advantage of the two system's strength, namely high spatial resolution of the radar (1-3 km) and high soil moisture accuracy of the radiometer. SMAP is based on the Hydros mission (*Entekhabi et al.*, 2004) that was cancelled in 2005 due to budgetary constraints (*Piles et al.*, 2009).

3. Methods

To start with, one SMOS pixel (DGG node 2002029 and surrounding area of 44 km in diameter) to be validated was selected covering the Skjern River Catchment in Western Denmark (Fig. 3.1).

Next, two complementary data sets were collected within this pixel. The acquisition of this data included (1) the design and establishment of a soil moisture and temperature network suitable for that purpose during fall 2009, including 30 stations with Decagon ECH2O 5TE sensors at 0-5, 20-25 and 50-55 cm depth, as well as in the organic layers (installed in summer 2010) in case of natural vegetation, and (2) the planning and realization of a campaign with the airborne radiometer EMIRAD-2 (1.4 km -3dB footprint, *Skou et al.*, 2010a) and simultaneous ground measurements between April 26 and May 9, 2010. Within three selected patches (2x2 km), covering the prevailing land cover conditions (agriculture, heath and coniferous forest with very sandy soils), soil moisture of the mineral and organic layers was measured by means of hand-held Delta T ML2x ThetaProbes (0-6 cm depth) at dense spacing. Land cover information was recorded for each measurement point and at some of the locations samples were taken of both layers. At the beginning and towards the

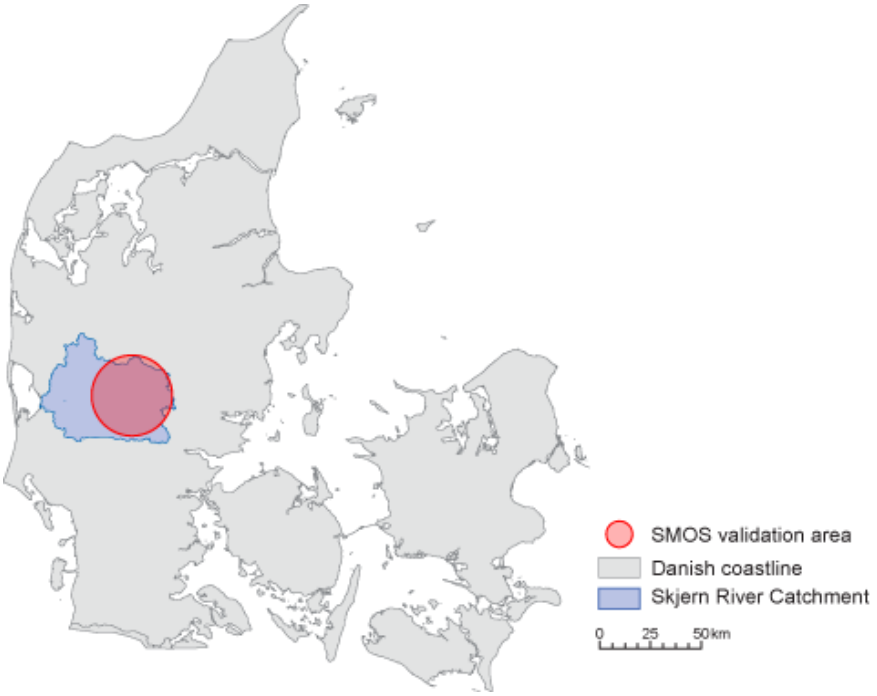

Figure 3.1.: Danish coastline (grey), Skjern River Catchment (blue) and selected SMOS pixel for validation (DGG node 2002029 and surrounding area of 44 km in diameter, red).

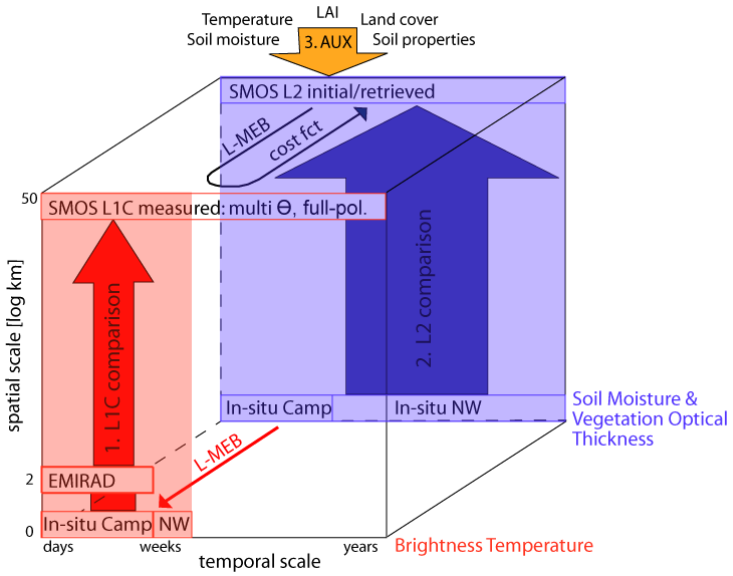

Figure 3.2.: Schematic illustration of approach followed for SMOS validation in the Skjern River Catchment

end of the campaign vegetation and roughness measurements were carried out. All data was preprocessed and quality checked before usage in the SMOS validation.

The chosen validation approach is illustrated in Fig. 3.2. Basically, there are three validation dimensions: the temporal and spatial scales, as well as two comparison levels, namely brightness temperature (L1C) and soil moisture and vegetation optical thickness (L2). In case of SMOS, initial data of soil moisture, temperature, Leaf Area Index (LAI), soil properties, land cover information, etc. (AUX products) are input to the retrieval algorithm. Based on the L-MEB radiative transfer model, brightness temperatures are calculated and compared to the ones acquired by SMOS (L1C product). Using the available multi-angular and full-polarization data a cost function is then minimized to retrieve soil moisture, and if data quality allows vegetation optical thickness and other parameters (L2 product).

In a first step, the same radiative transfer model was used in this dissertation to estimate brightness temperatures from the campaign ground sampling data (mineral soils only, each sampling point individually). The modeled data was averaged over the respective patches and compared to the corresponding EMIRAD footprints. Subsequently, the EMIRAD data was averaged over the SMOS pixel and compared to the L1C data. Additionally, the modeled patch data was averaged over the SMOS pixel using land cover fractions as weights, and compared. This validation approach has the advantage of step-wise bridging the large spatial scale differences. However, the two-week experiment with only four snapshot views of the prevailing conditions faces serious constraints in terms of the assessment of temporal variability. Thus, in a second step, the continuously recorded in situ network soil moisture data was averaged over all stations within the SMOS pixel and directly compared to initial and retrieved SMOS soil moisture data at L2 over much longer time frames. Thereby, the campaign period served as a link between the two data sets. For a period of a month spanning around the airborne campaign, brightness temperatures were also modeled for each

network station, and the average compared with SMOS, EMIRAD and modeled campaign data. Simultaneously, the brightness temperature data was put in relation with the corresponding soil moisture network data sets. Finally, the AUX products used in the SMOS retrieval algorithm were investigated: SMOS initial surface temperatures were compared with the average network temperatures from the 0-5 cm layer. Vegetation optical depth estimated for the modeling of the ground data from the vegetation sampling during the campaign was compared to the initial and retrieved SMOS vegetation optical depth. Likewise, this was done for the most important roughness model parameter. The land cover fractions assumed in the SMOS retrieval for the selected SMOS pixel were compared with the corresponding ones of a land cover classification with significantly higher spatial resolution. The soil properties (sand and clay fraction, soil bulk density) used in the SMOS retrieval were compared to field measurements conducted within the SMOS pixel in the campaign sampling patches as well as at the individual network stations.

Please note that all SMOS data used in this dissertation originates from the consistent data sets which were reprocessed by means of the state of the art L1 prototype algorithm (V3.46) in case of the L1C product and by means of the state of the art L2 prototype algorithm (V4.00) using the reprocessed L1 data in case of the L2 product.

One conference proceedings and three journal papers emanated from this dissertation. They describe all of the above in detail. An overview over their respective contents is compiled in Fig. 3.3 and a brief description of each article is given below:

Article 1: SMOS validation activities at different scales in the Skjern River Catchment, Western DK. Proceedings paper to ESA Living Planet Symposium, Bergen, Norway, June 28 - July 2, 2010. Bircher, S. Balling, J. and Skou, N. 2010.

This work introduces the study site, summarizes the airborne campaign activities including ground sampling, and presents first results of the collected campaign data. In case of the EMIRAD measurements, average brightness temperatures are listed for each flight day. In case of the ground moisture measurements, according averages from sensor readings in both mineral and organic layers are given and set in relation to network measurements of stations within the sampling patches. Based on this, the moisture conditions during the campaign period are discussed.

Article 2: Validation of SMOS brightness temperatures during the HOBE airborne campaign, Western Denmark. Accepted for publication in IEEE Transactions on Geoscience and Remote Sensing, SMOS Special Issue. Bircher, S., Balling, J. E., Skou, N. and Kerr, Y. H.

In this article the study site and the airborne campaign are described. ThetaProbe calibration for the mineral soils of the three campaign patches by means of gravimetric samples is illustrated. Furthermore, the estimation of auxiliary data based on field measurements is documented (soil bulk density, surface roughness standard deviation of height, vegetation water content) and the preprocessing and filtering of EMIRAD and SMOS data is illustrated.

		Article 1	Article 2	Article 3	Article 4
Study site	Selection of SMOS pixel			✓	
	Environmental conditions	✓	✓	✓	✓
Soil moisture & temperature network	Design			✓	
	Implementation			✓	
	Sensors and data			✓	
Soil sampling	Texture & soil bulk density		✓	✓	
Campaign ground measurements	Sensor calibration		✓		
	Mineral soil moisture readings	✓	✓		
	Organic moisture readings	✓			
	Auxiliary data (roughness, vegetation, land cover)		✓		
EMIRAD	Preprocessing		✓		
	Data	✓	✓		
SMOS	Retrieval algorithm		✓	✓	✓
	Preprocessing		✓		✓
	L-MEB model & parameter settings		✓		✓
Validation	L1C		✓		✓
	L2			✓	✓
	AUX				✓

Figure 3.3.: Overview of article contents

The theory of the L-MEB model, the choice of parameter settings, related uncertainties and associated model runs are described. Results of brightness temperature comparisons of average modeled ground data and EMIRAD at patch-scale as well as averaged EMIRAD, modeled patch data averaged over the SMOS pixel using land cover fractions as weights, and SMOS L1C data are shown and discussed.

Article 3: A soil moisture and temperature network for SMOS validation in Western Denmark. Submitted to Hydrology and Earth System Sciences, October 2011. Bircher, S., Skou, N., Jensen, K. H., Walker, J. P. and Rasmussen, L.

Here first the study site, the network equipment and the SMOS measurement and data retrieval concept are introduced. Subsequently the network design is illustrated by means of spatial analysis of the prevailing environmental conditions, followed by a description of the network implementation. Results of the collected network data are presented and discussed and first comparison with SMOS soil moisture, dielectric constant and surface temperature data is shown.

Article 4: Validation of SMOS L1C and L2 products and important parameters of the retrieval algorithm in the Skjern River Catchment, Western Denmark. Submitted to IEEE Transactions on Geoscience and Remote Sensing, October 2011. Bircher, S., Skou, N. and Kerr, Y. H.

This paper first describes the study site and the aquired validation data sets. The SMOS measurement and retrieval concept as well as the applied filtering are introduced. Subsquently, the main findings from the first three articles are shortly compiled. Finally, built on this, refined validation work on the SMOS L1C and L2 products, as well as comparison of the most sensitive retrieval algorithm parameters (vegetation optical thickness, surface roughness, soil properties, land cover) with in situ data are presented. The results are discussed in context of worldwide SMOS validation.

With respect to the network data, please note that originally a second sensor type (Decagon ECH2O EC-5) was installed to reproduce the Decagon ECH20 5TE measurements. However, as the two sensors were not found to be comparable without the application of very sophisticated sensor-specific calibrations, the EC-5 measurements were only used for the work presented in article 1, while discarded for all subsequent analyses (articles 3 and 4). However, this does not alter the main conclusions drawn of this study except for improving the agreement between the Decagon 5TE and the Delta T ML2x ThetaProbe measurements as can be seen from Fig. A.1 in Appendix A. The enhanced accordance furthermore results from site-specific calibration of the ThetaProbe readings in the mineral soil. The respective organic data has not been calibrated as it has not been used in the analysis yet. In case of the Decagon 5TE measurements, checks showed that site-specific calibration was not necessary to stay within the desired accuracy of 0.03 m^3/m^3. Corresponding standard deviations of the ThetaProbe readings using the site-specific calibration are listed in Tab. A.1 in Appendix A.

Part II.

Research Papers

4. SMOS Validation activities at different scales in the Skjern River Catchment, Western DK (Paper 1)

Bircher, S., Balling, J. and Skou, N.

Paper published in: ESA Living Planet Symposium, Bergen, Norway, 28. June - 02. July, 2010

Abstract The recently launched passive L-band microwave radiometer of the Soil Moisture and Ocean Salinity (SMOS) Mission delivers continuous large-scale soil moisture data which has the potential to ameliorate currently incomplete simulations of the water balance. However, the data first needs to be calibrated and validated. One validation site is operated within the framework of the Danish Hydrological OBservatory and Exploratorium (HOBE) in the Skjern River Catchment, Western Denmark. Here we describe the validation site and an airborne campaign with the passive L-band microwave radiometer EMIRAD in detail and present first results of the conducted ground and remotely sensed measurements. Throughout the campaign, agricultural mineral soils exhibited driest conditions, while the moss/organic layers in heath and forest clearly held highest moisture contents. In the near future, ground measurements will be upscaled and compared with both EMIRAD and SMOS data.

4.1. Introduction

The assessment of water resources is vital in a changing climate. Currently, in hydrological models problems exist with closure of the water balance at catchment scale - the scale on which sustainable water management strategies should be addressed. One of the major uncertainties is soil moisture. The passive L-band microwave radiometer SMOS launched in November 2009 delivers continuous large-scale soil moisture data which, when downscaled and assimilated into hydrological models, has the potential to ameliorate current simulations of the water balance. However, the data first needs to be calibrated and validated and such activities are presently ongoing in most parts of the world (*Delwart et al.*, 2008; *Peischl et al.*, 2009). One such validation site is situated in the Skjern River Catchment in Western Denmark. Interesting characteristics that distinguish this area from other SMOS validation sites are its short distance to the coast line in two directions and the very sandy soils with large moss/organic deposits due to the location at Northern latitudes. At present, the catch-

ment is broadly investigated through HOBE (`www.hobecenter.dk`). Within this project a soil moisture network has been installed to provide in situ soil moisture data feasible for upscaling and comparison with SMOS soil moisture data at large scale. To further support validation activities an airborne campaign with the passive L-band microwave radiometer EMIRAD, as well as simultaneous ground sampling, were carried out in the Skjern River Catchment in spring 2010 to directly acquire soil moisture data at intermediate scale (few kilometers spatial resolution). This paper describes the validation area and the airborne campaign in detail. First results of conducted ground and remotely sensed soil moisture measurements are presented and an outlook on future validation activities is given.

4.2. Description of the validation site

SMOS DGG node 2002029 (55.957 N, 9.131 E) and a surrounding area of approximately 44 km diameter (where nearly 100% of the measured SMOS signal used for data retrieval at the respective grid node originates from) have been selected as validation area (Fig. 4.1a). This region fulfills the criteria of maximizing its coverage of the Skjern River Catchment while at the same time minimizing the open water fraction within the validation site. The area comprises mainly low-relief glacio-alluvial plains with very sandy soils. Land cover includes nearly 80% agriculture, ca. 10% forest (mostly spruce) and 6% heath, moors and shrubland. The area is sparsely populated with scattered villages and farms. For the broadly investigated Skjern River Catchment a wealth of historical data is available, and HOBE is maintaining four test sites where all components of the water cycle are assessed (Fig. 4.1b).

4.3. Validation campaign

4.3.1. Airborne measurements

Four flights with the passive L-band microwave radiometer EMIRAD were carried out within a two week time window, namely on April 29, May 2, 4, and 9, 2010. EMIRAD has two antennas (nadir and 40 degree aft) and operates in full polarization mode with 1 msec integration time (*Skou et al.*, 2006). At the beginning of each flight sea calibration was conducted over the Ringkøbing Fjord. Consecutively, 10 north-south tracks were flown over the validation site in such a manner that a maximum number of ground soil moisture network stations and the dense snapshot sampling patches were covered (Fig. 4.1b). For all flights flight altitude was chosen at 2000 m corresponding to an approximate -3dB swath of 1.4 km. The respective flight duration was 3 hours centered around SMOS ascending overpass at approx. 6:30 a.m. local time. EMIRAD data is internally calibrated at regular intervals during the measurements by means of the radiometer's internal load as well as its noise diode. Additionally, to verify the stability of the instrument over time external calibration (including the antenna cables) is preformed in connection with each flight utilizing a standard noise generator cooled with liquid nitrogen.

4.3.2. Simultaneous ground measurements

During the flights surface soil moisture measurements on three 2x2 km patches of differing land cover (agriculture, heath and forest, Fig. 4.1c-e) were conducted by means of hand-

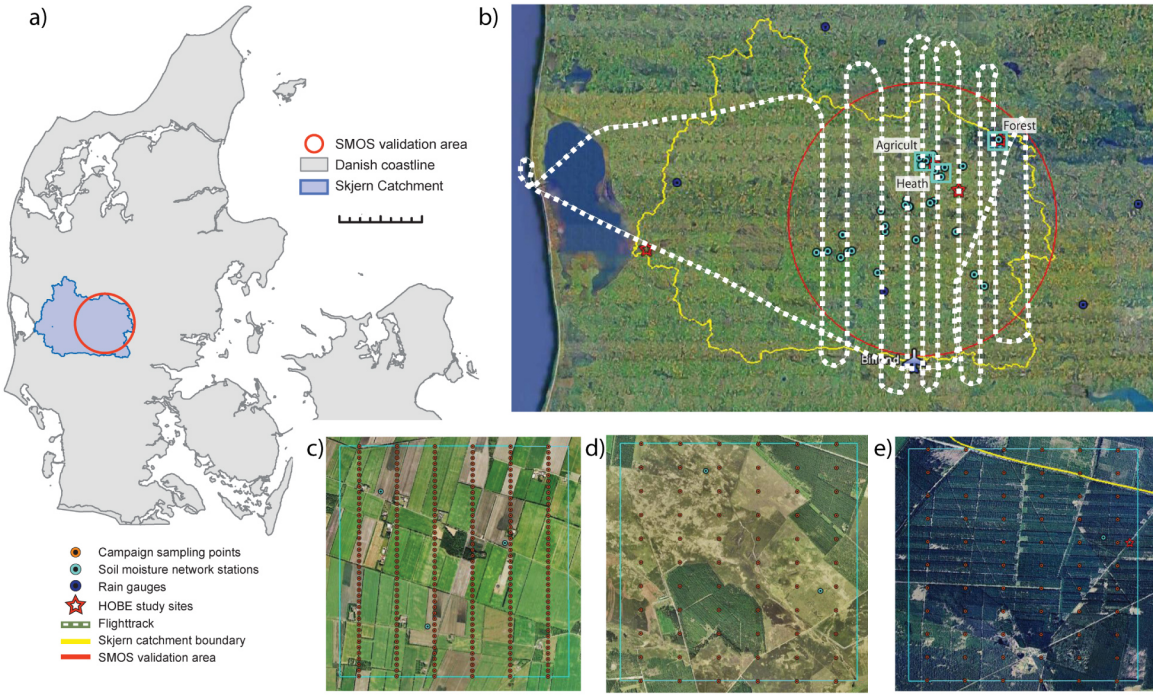

Figure 4.1.: Area overview. a) Danish coastline, Skjern River Catchment and SMOS validation site around DGG node 2002029, b) campaign flight tracks and sampling patches, network stations, DMI rain gauges and HOBE sites, c) agriculture, d) heath, and e) forest campaign ground sampling transects.

Figure 4.2.: Moss/organic layer.

held Delta-T ML2x ThetaProbes (integrating over 0-6 cm depth). The forest and heath patches were only sampled on the first three, the agricultural patch on all four flight days. Sampling time was about 4 - 6 hours roughly centered around ascending SMOS overpass time. On the agricultural patch 6 north-south transects were sampled at a spacing of 50 m with 3 Theta readings from the top of the mineral soil per location. On the heath and forest patches where a 5-20 cm thick moss/organic layer is prevalent in most cases (Fig. 4.2), the sampling spacing was 200 m with 3 readings from the top of the moss/organic layer and the mineral soil, respectively, per location. Gravimetric samples were taken at 15 locations per patch in case of the mineral soil, and at 33 locations on the heath and forest patches in case of the moss/organic layer. At the beginning and the end of the campaign destructive vegetation sampling was carried out on the agriculture and heath at around 8 locations per patch. Additionally, on the agricultural patch LAI measurements were conducted at the vegetation sampling sites by means of a Licor LAI-2000, and few 3 m surface roughness transects (north-south and east-west direction, respectively) were measured on freshly sown flat spring barley fields and freshly planted potato fields with pronounced row structure.

4.4. Soil moisture network

A soil moisture network was established within the selected SMOS validation area during autumn/winter 2009 (Fig. 4.1b) The network includes 30 stations which are spatially distributed according to respective fractions of prevailing land cover and soil types and aligned along the mean annual precipitation gradient of the area (*Bircher et al.*, Submitted). Per station, 1 Decagon 5TE (soil moisture, temperature, electrical conductivity) and 1 EC-5 (soil moisture) sensor are installed at 0-5 cm, and 20-25 cm depth of the mineral soil, respectively. Additionally, 1 5TE sensor measures the 50-55 cm depth. The logging interval is set to 30 minutes.

4.5. First results and discussion

4.5.1. Ground data

Average ThetaProbe readings and corresponding standard deviations for all respective patches and campaign dates are shown in Tab. 4.1. Fig. 4.3 depicts surface soil moisture measurements acquired by means of soil moisture network stations and hand-held ThetaProbes within the three patches during the spring campaign, along with averaged 24 hour precipitation sums of the 5 closest rain gauges of the Danish Meteorological Institute (DMI, `www.dmi.dk`) (see Fig. 4.1b). The soil moisture measurements are calculated by default calibration functions for Decagon sensors and ThetaProbes, respectively. Concerning the network data an average of all available 0-5 cm soil moisture measurements within each respective patch is presented (see Fig. 4.1c-e). Soil moisture generally follows the precipitation trend. The occuring time-shifts in precipitation-moisture response may be caused by the spatial distance between the soil moisture and precipitation measurement locations (see Fig. 4.1b). No considerable changes in average moisture content were observed between the different campaign sampling days. Network soil moisture and Theta readings are in comparable range and show similar patterns. However, there seems to be a bias

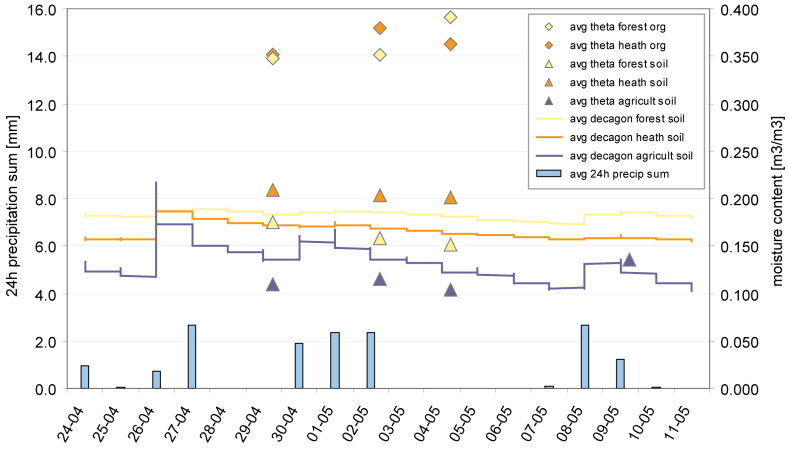

Figure 4.3.: Average 24 hour precipitation sum of 5 DMI rain gauges, average moisture from ThetaProbes and network stations within respective patches during airborne campaign.

between the measurements acquired by the two different sensor types. Agreement could possibly be improved by applying site- and sensor-specific calibration to the Decagon and ThetaProbe measurements which will be tested in the near future. Only the average Theta reading of the agricultural mineral soil from May 9 seems to somewhat deviate from the trend observed on the other sampling dates. That day, the patch was sampled by more people with adjusted sampling strategy, and might indicate altering spatial-temporal soil moisture conditions during the sampling time slot. This has to be further investigated. Agricultural mineral soils exhibited driest conditions throughout the campaign, and at the same time the network data shows a more distinct precipitation-moisture response for the mineral soil of this land cover type compared to heath and forest. The latter can be explained by the presence of moss/organic layers with high water storage capability on top of the mineral soils in forest and heath which act as a buffer. These layers appear to follow the precipitation trend more closely and clearly exhibit much higher moisture contents than the underlying mineral soils. This implies that with maximum likelihood emissions measured by radiometers originate to the largest extent from this layer. The spatial variability of the moisture content is generally high for all investigated land cover types and campaign dates. The moss/organic layers clearly exhibit the highest variability. In case of the mineral soils, variability is significantly higher in heath and forest compared to agriculture.

4.5.2. Airborne data

For May 2, EMIRAD antenna level brightness temperature (T_B) measurements in H and V polarization and for both nadir and 40 degrees aft antenna, respectively, are shown in Fig. 4.4. Please note that the data is displayed with the approximate -3dB swath at the roughly true ground location. In Tab. 4.2 average H and V polarized brightness temperatures for nadir and 40 degree aft antennas and for all flight days, respectively, are listed. A preliminary RFI filtering scheme is applied to the data. All measurements above 300 K T_B and/or with kurtosis ratios outside the mean +/- 4 standard deviation interval from an

Table 4.1.: Average (Avg.) and standard deviation (Std.) of ThetaProbe moisture readings $[m^3/m^3]$ for respective patches and campaign dates.

Date	Agriculture Soil		Heath Soil		Organic		Forest Soil		Organic	
	Avg.	Std.	Avg.	Std.	Avg.	Std.	Avg.	Std.	Avg.	Std.
29.04	0.109	0.039	0.209	0.118	0.351	0.170	0.175	0.088	0.349	0.120
02.05	0.115	0.043	0.203	0.101	0.380	0.158	0.158	0.088	0.352	0.125
04.05	0.104	0.034	0.201	0.114	0.363	0.160	0.152	0.068	0.391	0.133
09.05	0.136	0.033								

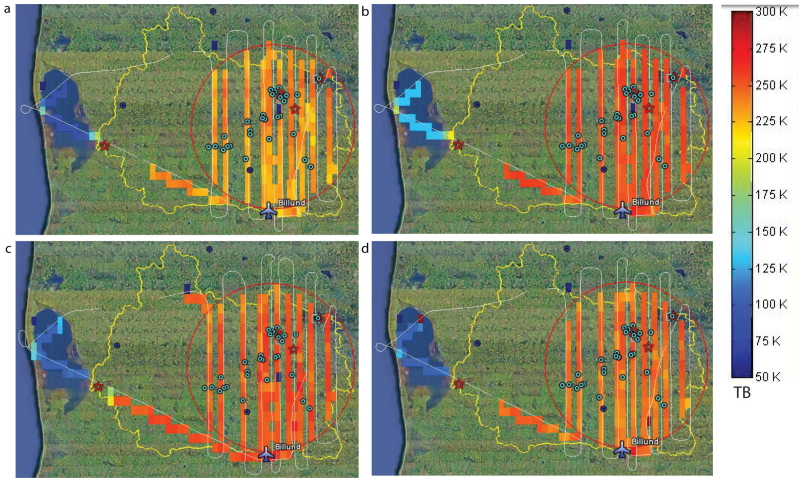

Figure 4.4.: EMIRAD antenna level T_Bs [K] for May 2, with approx. -3dB swath width. 40 deg aft a) H pol, b) V pol; nadir c) H pol, d) V pol.

RFI-free signal are flagged as RFI-contaminated (RFI-%). In accordance with the ground measurements, no considerable changes in average EMIRAD brightness temperatures were observed between the different campaign sampling days. Note that the relatively high standard deviations obtained for the here presented 1 msec data will be lowered after data integration. RFI-% is low throughout all flight dates.

4.5.3. SMOS data

On all flight days, SMOS brightness temperature data of DGG node 2002029 acquired at certain incidence angles exhibits unrealistically high/low brightness temperature values (possibly resulting from not yet tackled RFI problems, calibration artifacts, aliasing, etc.). However, in each case more reasonable values obtained from measurements at other incidence angles seem to exist. Careful data selection for validation will be a crucial task. As an example, Fig. 4.5 shows SMOS Top Of Atmosphere (TOA) H and V polarized brightness temperatures as a function of incidence angle on May 2 ascending overpass for DGG node 2002029.

Table 4.2.: Average (Avg.) and standard deviation (Std.) of EMIRAD H and V pol brightness temperatures [K] for nadir and 40 degree aft antennas on respective campaign dates.

Date	40°						Nadir					
	H			V			H			V		
	Avg.	Std.	RFI-%	Avg.	Std.	RFI-%	Avg.	Std.	RFI-%	Avg.	Std.	RFI-%
29.04	238.17	7.34	1.67	257.69	5.13	0.85	250.23	9.49	0.64	248.99	6.72	0.48
02.05	234.11	7.98	0.92	253.21	5.29	0.75	244.76	8.42	0.49	244.25	6.99	1.61
04.05	238.87	7.13	1.93	256.03	5.11	0.85	248.54	6.93	1.02	248.28	6.20	0.51
09.05	235.57	8.24	1.42	254.07	5.15	0.38	246.00	9.39	0.57	245.18	7.06	0.27

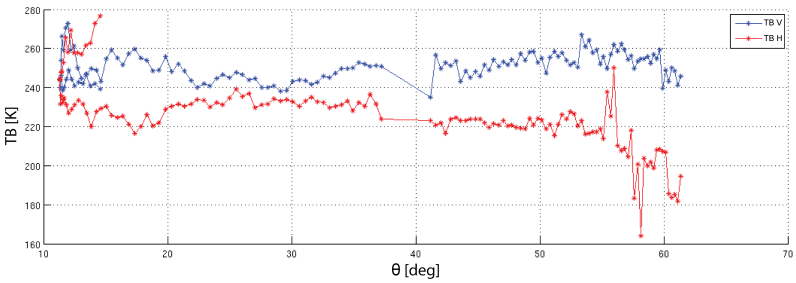

Figure 4.5.: SMOS TOA H and V pol T_Bs [K] as function of incidence angle [deg] for DGG node 2002029 on May 2.

4.6. Conclusions and outlook

Within the framework of HOBE, SMOS validation activities are carried out in the Skjern River Catchment, Western Denmark. Here the validation site and the conducted airborne campaign are described and first results of the acquired data presented. No considerable changes in average moisture content and brightness temperatures between the different campaign sampling days were observed through the ground and airborne measurements, respectively. Network soil moisture and Theta readings are in comparable range, though with a bias between the two different sensor types. This issue will be addressed by applying site- and sensor-specific calibration. Throughout the campaign, agricultural mineral soils exhibited driest conditions with more distinct precipitation-moisture response compared to heath and forest, where buffering moss/organic layers are present. The latter appear to follow the precipitation trend more closely and clearly exhibit much higher moisture contents. This implies that in case of forest and heath remotely sensed signals most likely originate mainly from these moss/organic layers which therefore should be taken into account in the validation process. The SMOS brightness temperatures for DGG node 2002029 (ascending overpasses) seem to be disturbed on all flight days, but for each day reasonable data at certain incidence angles exist. The crucial task will be to carefully select the SMOS data to be validated. In the near future, the acquired ground measurements (network and campaign Theta readings) will be used to simulate and upscale brightness temperatures to the scale of the remotely sensed data sets. By this means, ground measurements will be compared with both EMIRAD and SMOS data. EMIRAD data will itself be upscaled and compared to SMOS products. In a later stage the products will also be compared at soil moisture

level. Investigation of different upscaling techniques is planned. Special focus will be put on the impact of open water and the moss/organic layer.

Acknowledgments A special thank goes to all persons involved in the organization of the airborne campaign and the motivated ground sampling teams who did an excellent job. Further thank goes to Yann Kerr and his entire team at CESBIO for valuable discussions and providing codes for SMOS data processing. We are also very thankful for the ThetaProbes supplied by CESBIO and AALTO University.

5. Validation of SMOS brightness temperatures during the HOBE airborne campaign, Western Denmark (Paper 2)

Bircher, S., Balling, J., Skou, N. and Kerr, Y.

Paper accepted for publication in: IEEE TRANSACTIONS ON GEOSCIENCE AND REMOTE SENSING

Abstract The Soil Moisture and Ocean Salinity Mission (SMOS) delivers global surface soil moisture fields at high temporal resolution which is of major relevance for water management and climate predictions. Between April 26 and May 9, 2010, an airborne campaign with the L-band radiometer EMIRAD-2 was carried out within one SMOS pixel (44x44 km) in the Skjern River Catchment, Denmark. Concurrently, ground sampling was conducted within three 2x2 km patches (EMIRAD footprint size) of differing land cover. By means of this data set the objective of this study is to present the validation of SMOS L1C brightness temperatures T_B of the selected node. Data is stepwise compared from point via EMIRAD to SMOS scale. From ground soil moisture samples T_Bs are point-wise estimated through the L-band Microwave Emission of the Biosphere (L-MEB) model using land-cover specific model settings. These T_Bs are patch-wise averaged and compared with EMIRAD T_Bs. A simple uncertainty assessment by means of a set of model runs with the most influencing parameters varied within a most likely interval results in a considerable spread of T_Bs (5-20 K). However, for each land cover class a combination of parameters could be selected to bring modeled and EMIRAD data in good agreement. Thereby, replacing the Dobson dielectric mixing model with the Mironov model decreases the overall RMSE from 11.5 K to 3.8 K. Similarly, EMIRAD data averaged at SMOS scale and corresponding SMOS T_Bs show good accordance on the single day where comparison is not prevented by strong RFI (May 2, avg. RMSE=9.7 K). While the advantages of solid data sets of high spatial coverage and density throughout spatial scales for SMOS validation could be clearly demonstrated, small temporal variability in soil moisture conditions and RFI contamination throughout the campaign limited the extent of the validation work. Further attempts over longer time frames are planned by means of soil moisture network data as well as studies on the impacts of organic layers under natural vegetation and higher open water fractions at surrounding grid nodes.

5.1. Introduction

Soil moisture is a key variable for water resources and crop management, weather and climate predictions as well as hazard analysis. It is highly variable in space and time across scales (*Western et al.*, 2002; *Cosh et al.*, 2004) and thus, one of the major uncertainties in climate and hydrological models. Reliable soil moisture data of global coverage and with high temporal resolution is urgently needed.

By means of a spaceborne passive L-band (1.4 GHz) radiometer the Soil Moisture and Ocean Salinity Mission (SMOS) (*Kerr et al.*, 2001) acquires global surface soil moisture fields (~5 cm depth) every 3 days since launch in November 2009. Using full polarization multi-angle brightness temperature (T_B) measurements at ~44 km spatial resolution soil moisture is retrieved for each node of a fixed grid (*Kerr et al.*, 2011). The forward model in the retrieval algorithm is the L-band Microwave Emission of the Biosphere (L-MEB) model (*Wigneron et al.*, 2007). To account for influences of vegetation and surface roughness L-MEB uses several fitting parameters whose ideal values for various land cover conditions have been investigated in many previous studies, (eg. *Pardé et al.*, 2004; *Grant et al.*, 2008; *Panciera et al.*, 2009a,b; *Saleh et al.*, 2009; *Cano et al.*, 2010).

At this stage an important step of the SMOS mission is data validation in different climatic regions (*Delwart et al.*, 2008). Generally, the comparison between large-scale satellite products and point measurements on the ground is complicated by the distinct scale-mismatch (*Cosh et al.*, 2004). To bypass this problem one widely used approach is the performance of airborne campaigns with concurrent ground measurements at the times of the satellite overpasses. Via the airborne measurements with a footprint of few kilometers, this offers the advantage of stepwise validation across spatial scales.

Several airborne campaigns were carried out in preparation of the SMOS and similar missions and constitute a core activity in current SMOS calibration and validation (Cal/Val), e.g. arid climate, southeastern Australia: *Panciera et al.* (2008); *Merlin et al.* (2008); *Peischl et al.* (In Prep.); temperate zone, Upper Danube, Rur- and Erft Catchments, Germany: *Dall'Amico et al.* (2010); *Kainulainen et al.* (2010), southwestern France: *Albergel et al.* (2011), central USA: *Schmugge et al.* (1988); *Jackson et al.* (1995, 1999); Arctic, northern Finland: *Kontu et al.* (2010).

Between April 26 and May 9, 2010, one campaign took place in the Skjern River Catchment, Denmark, within the framework of the Danish Hydrological OBservatory and Exploratorium (HOBE, `www.hobe.dk`) (*Bircher et al.*, 2010). During flights centered at SMOS ascending overpass airborne measurements with the L-band radiometer EMIRAD-2 (*Skou et al.*, 2010a) were conducted within the 44x44 km area around one selected SMOS grid node (referred to 'SMOS pixel' hereafter). Surface soil moisture of the mineral as well as the organic layers, vegetation water content and roughness were measured on differing land covers within patches corresponding to approximate EMIRAD footprint (~2x2 km).

The importance of validating SMOS data at the Danish site is twofold. First, it complements the other Cal/Val regions in that it is Europe's northernmost intensely cultivated area with features related to latitude-specific environmental conditions such as sandy soils with large organic deposits and heathland. Secondly, the area is located at short distance to the coast line enabling studies of the impact of surrounding open water. The site benefits from temporally increased data acquisition at this latitude and from its pronounced flatness.

The objective of this article is to present the validation of SMOS L1C T_B data of one selected pixel by means of the HOBE airborne campaign data set. Data is compared at different spatial scales: (1) averaged modeled ground data and EMIRAD data at patch scale (2x2 km), (2) averaged modeled ground data, EMIRAD data and SMOS data at SMOS pixel scale (44x44 km). L-MEB is used to model T_Bs from in situ soil moisture with parameter choice based on literature as well as parameterization using campaign measurements. Three sets of model runs are conducted to (1) assess the spread in the modeled T_Bs as a result of parameter uncertainties and variability, (2) to determine ideal values for the most important roughness and vegetation parameters (H_R and τ_{NAD}), and (3) to test the performance of the Mironov dielectric mixing model against the one of Dobson, as well as two combinations of the roughness parameter pair N_{RH}/N_{RV} using an 'optimal' set of model parameters. At both scales, the benefit of a weighted average by means of the EMIRAD/SMOS antenna patterns, respectively, over a simple mean is investigated.

In this study only moisture data from the mineral soils is considered and a SMOS pixel virtually free of open water is chosen. Resulting knowledge creates a foundation for future investigations addressing the peculiarities of the Danish site, namely open water impact and influence of organic matter.

5.2. Data

5.2.1. Description of validation site

The SMOS pixel around grid node 2002029 (55.957 N, 9.131 E) was chosen for validation as it features minimal open water fraction while covering a substantial part of the Skjern River Catchment (~2500 km^2) in Western Denmark (Fig. 5.1a+b). The climate is temperate-maritime with winter and summer mean temperatures of ~2 and 16 $°C$, respectively, and annual precipitation around 800-900 mm. The eastern edge of the catchment is situated at the margin of the ice sheet during the last glacial advance with mainly loamy soils on undulating calcareous tills, while the major part comprises the primal fluvioglacial outwash plain with sandy soils and sediments (*Greve et al.*, 2007). The natural soil type is podsol covered by a pronounced raw humus layer. Nearly 80% of the land is under intensive cultivation (mainly winter/spring barley, potatoes and grass), intermixed with patches of forest (mostly spruce plantations with scarce understory and moss-covered ground, ca. 10%), as well as heath/grassland (primarily scotch heather with a herbal layer and dry grass) and wetlands (ca. 6%). The area is sparsely populated with scattered farms and villages.

The catchment is well-covered with climate stations and rain gauges operated by the Danish Meteorological Institute (DMI). HOBE is maintaining four sites to assess a wealth of hydrological parameters (*Jensen and Illangasekare*, 2011). In autumn 2009 a soil moisture network was established within the SMOS validation area (Fig. 5.1b). The network includes 30 stations which are spatially distributed according to respective fractions of prevailing land cover and soil types and aligned along the 30-year mean annual precipitation gradient (*Bircher et al.*, Submitted). Per station, soil moisture and temperature within the 0-5 cm, 20-25 cm and 50-55 cm depth ranges of the mineral soil are logged at 30 minute intervals.

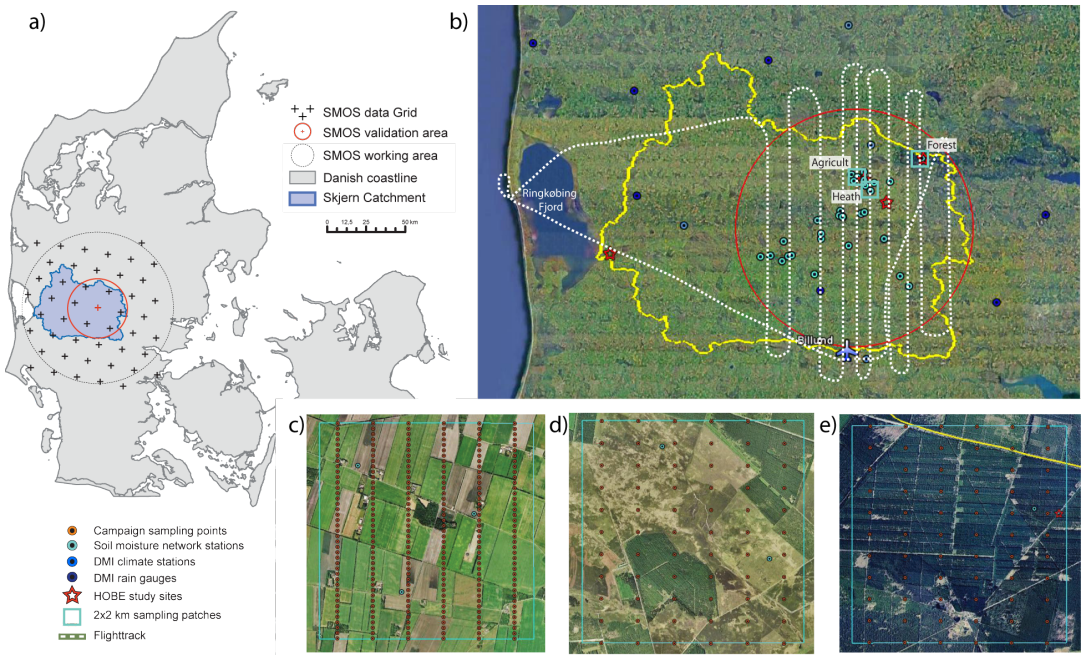

Figure 5.1.: Overview over the validation site: a) Danish coastline, Skjern River Catchment, SMOS pixel (44x44 km) and working area (123x123 km) around grid node 2002029, b) campaign flight tracks and sampling patches, soil moisture network stations, DMI rain gauges and HOBE study sites, c) agriculture, d) heath, and e) forest campaign ground sampling transects within respective 2x2 km patches

5.2.2. HOBE airborne campaign

The HOBE airborne campaign (*Bircher et al.*, 2010) took place between April 26 and May 9, 2010. Four 3-hour flights (April 29, May 2, 4, and 9) were carried out centered around SMOS ascending overpasses at ~6.30 local time. Simultaneously, ground measurements were taken within three 2x2 km patches selected according to the area's most representative land covers, agriculture, heath/grassland and forest (Fig. 5.1c-e). Within the agriculture patch all fields were under cultivation and still of bare appearance, with the exception of winter barley.

Ground data

Soil moisture measurements were carried out with hand-held Delta T ML2x ThetaProbes[1] (0-6 cm depth). The forest and heath patches were sampled on the first three, the agricultural patch on all four days. Sampling time was 4-6 hours roughly centered around SMOS overpass. Altering spatio-temporal soil moisture conditions during the sampling time slot were not discovered. On the agricultural patch along six north-south transects each 50 m three readings were recorded from the top of the mineral soil (Fig. 5.1c). On the heath and forest patches the sampling spacing was enlarged to 200 m (Fig. 5.1d-e) as per location additionally three readings were acquired from the top of the 5-20 cm thick moss/organic

[1]Mention of manufacturers is for the convenience of the reader only and implies no endorsement on the part of the authors

layer. Gravimetric samples were taken at 15 locations per patch in case of the mineral soil, and at 33 locations in case of the moss/organic layer. Land cover type and vegetation height were recorded for each sampling point.

Sensor- and site-specific linear calibration curves (for each sensor individually/all sensors together) were derived in the lab over the entire wetness range using mineral surface soil samples from the three patches, and validated by means of the field gravimetric samples (Fig. 5.2). ThetaProbe readings were recalculated using the respective sensor-specific calibration curves or the site-specific where the sensor id was not applicable. For all sampling patches and dates average soil moisture values and standard deviations (Table 5.1) reveal a high spatial variability, but no considerable temporal variability as a result of only few insignificant rain events (<3 mm in each case). Throughout the campaign, driest conditions were found in the agriculture patch with a more pronounced precipitation-moisture response. In case of heath and forest the latter is dampened by the presence of the organic layers (*Bircher et al.*, 2010).

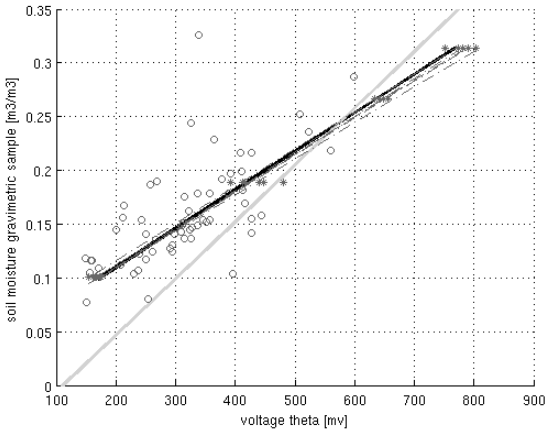

Figure 5.2.: ThetaProbe default curve (from manufacturer) for mineral soils (light grey -), and sensor- and site-specific linear ThetaProbe calibration curves (dark grey – and black -) derived from ThetaProbe lab measurements [mV] (dark grey $*$) and validated with gravimetric field samples [m^3/m^3] (dark grey $\circ$) at the example of agricultural mineral soil.

Table 5.1.: Average and standard deviation of the ThetaProbe soil moisture values (recalibrated by means of sensor-specific curves) [m^3/m^3] of the mineral soil for all respective campaign dates and patches.

	Agriculture		Heath		Forest	
	Avg.	Std.	Avg.	Std.	Avg.	Std.
29/04	0.146	0.031	0.237	0.075	0.184	0.075
02/05	0.151	0.033	0.235	0.069	0.168	0.07
04/05	0.142	0.026	0.232	0.073	0.162	0.06
09/05	0.167	0.027				

Soil bulk density estimated by means of the collected soil samples revealed average values (standard deviations) of 1.21(0.16), 1.31(0.16) and 1.34(0.18) g/cm^3 for agriculture, forest

and heath, respectively. Site-specific texture analysis of the campaign samples gave sand- and clay fractions between 0.82-0.95 and 0.01-0.05, respectively. This is in good agreement with the Danish topsoil grid (*Greve et al.*, 2007) indicating sand/clay fractions in the order of 0.75-1.0/0.0-0.05 within all three patches.

On April 28 and May 6 destructive vegetation sampling was carried out on agriculture land and heath at eight locations per patch (one sample in case of agricultural grass). A significant increase in average vegetation water content between the two measurement dates was observed for all vegetation types (except agricultural grass, Table 5.2).

Table 5.2.: Average and standard deviation of vegetation water content [kg/m^2] estimated for different land cover types on April 28 and May 6, respectively. Please note that on agriculture grass only one sample was taken per date.

		28/04		06/05	
		Avg.	Std.	Avg.	Std.
Agriculture	Spring barley	0.014	0.004	0.102	0.044
	Winter barley	0.519	0.11	1.105	0.152
	Grass	0.913		0.216	
Heath	Natural grass	0.338	0.222	0.622	0.417
	Scotch heather	0.496	0.308	0.703	0.3
	Scotch heather/grass	0.335	0.088	0.55	0.139

Within the agriculture patch 3 m transects of surface roughness were measured in both N-S and E-W direction on two recently plowed and sown spring barley fields and two freshly planted potato fields with pronounced row structure. The mean (standard deviation) root mean square deviations from the average measured heights (standard deviation of the height, S_D) over all available profiles per field type are 10.64(4.99), 9.76(0.85), and 63.51(5.80) mm in case of spring barley, potato parallel and orthogonal to row structure, respectively. These values span the conditions expected on agricultural fields and are in same magnitude as reported from other studies (e.g. *Wigneron et al.*, 2011). Within the heath and forest patches measurements were omitted as it was not possible to remove the vegetation cover without heavily disturbing the surface.

Airborne data (EMIRAD-2)

The airborne measurements were acquired by means of the L-band radiometer EMIRAD-2 (*Skou et al.*, 2010a) at incidence angles of 0 and 40° and both, H and V polarization (pol.), respectively, and integrated to 1 millisecond. On each sampling day ten north-south tracks were flown over the validation site to cover the selected sampling patches as well as a maximum number of network stations (Fig. 5.1b). Altitude was kept at 2000 m corresponding to an approximate -3 dB swath of 1.4 km. EMIRAD data coverages of the SMOS pixel and the 2x2 km patches were ~35 and 75%, respectively, and fairly consistent for 0 and 40° antennas on all dates (Fig. 5.3a-c).

Standard internal and external calibration by means of liquid nitrogen as well as over open water in the Ringkøbing Fjord at the beginning of each flight were conducted. This revealed a systematic offset of ~3.5 K in the 40° V-pol. channel. The bias is assumed to be caused by a source contained within the aircraft since it also appereared during

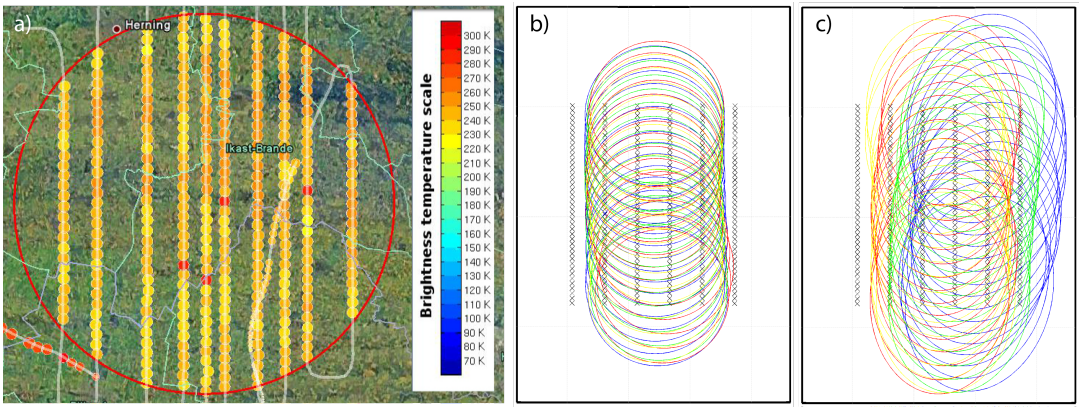

Figure 5.3.: a) EMIRAD-2 brightness temperature data coverage of the SMOS pixel (44x44 km) around grid node 2002029 for 0° H-pol on May 2, and coverage of the agriculture 2x2 km patch for b) 0° and c) 40° antennas, respectively. Blue: April 29, red: May 2, green: May 4, yellow: May 9.

subsequent flights in Southern Germany but was no longer present during later ground testing. The offset has not been corrected for as it does not change the overall conclusions of our study. It constitutes a secondary problem compared to the radiofrequency interference (RFI) contamination discovered in the SMOS data (see Section 5.2.2), and since it is well-known it could be taken into account during data analysis over land where a deviating behavior of this channel was noticed as well (see Section 5.5.1, Fig. 5.4-5.5).

The EMIRAD data was flagged as RFI-contaminated if measurements exhibited kurtosis ratios outside the mean +/-4 standard deviation interval from a signal known to be free from RFI (*Skou et al.*, 2010b), and/or where T_Bs/3rd and 4th Stokes parameter values were >300 K/outside the +/-10 K range, respectively. RFI-contamination of the EMIRAD data within the SMOS pixel was low throughout the campaign (~3-5%). After the RFI-cleaning the data was integrated to 1 second.

The onboard GPS and inertial navigation system (EGI) as well as the digital elevation model obtained by the Shuttle Topography Mission (SRTM) (*Jarvis et al.*, 2008) were used to georeference the locations of the antenna boresights and associated extents of the -3 dB footprints to the ground assuming flat earth. The effects of rotation-related polarization mixing (*Gasiewski*, 1993) were removed from the data by means of the aircraft attitude information.

Spaceborne data (SMOS)

L1C T_B data spanning a month centered on the HOBE campaign was considered in this study. For comparison with EMIRAD data, the L1C data was transferred from antenna to Top Of Atmosphere (TOA) level (XY to HV) by applying Faraday and geometric rotations.

The L1C data is resampled to a fixed grid with ~15 km spacing, while the overall received signal power originates from an area of ~123x123 km around each node. The signal integrates observations of a range of incidence angles (~0-60°) and view directions, and is weighted by the shape of the SMOS antenna pattern (*Kerr et al.*, 2011) with a -3 dB footprint of ~40-50 km (SMOS pixel, Fig. 5.1a). The radiometric land cover fractions (considering this

antenna weighting pattern) of open water, low vegetation and forest for SMOS pixel 2002029 are 0.4, 84.2 and 14.5%, respectively.

In contrast to the low-altitude EMIRAD data, SMOS data turned out to be heavily RFI-contaminated during the campaign period (*Daganzo et al.*, 2010; *Skou et al.*, 2010c). Additionally, there are unresolved SMOS image reconstruction issues due to land-sea contamination (transition between surfaces with very different T_Bs). To remove overpasses with corrupt observations, L1C data was filtered. As the L1C RFI flag is inoperative at present, 'good data quality' was based on corresponding soil moisture (L2) products. Filtering criteria included (1) absolute abscissa of dwell line (X_SWATH) < 10000, (2) probability that no anomaly occurred about the fit ($CHI2\_P$) > 0.5, (3) sum of number of deleted views due to RFI in X and Y pol. ($N\_RFI\_X+N\_RFI\_Y$) divided by number of views initially available for the given grid node (M_AVA0) < 0.1, and (4) confidence flag raised when retrieval has failed (FL_NO_PROD) $= 0$. This resulted in seven 'clean' ascending overpasses (April 19 and 27, and May 2, 10, 12, 15 and 17). T_Bs contained in these data sets were furthermore cut off at 300 K to get rid of potentially still present unrealistically high values.

5.3. Radiative transfer model - L-MEB

A version of the L-band Microwave Emission of the Biosphere (L-MEB) Model (*Wigneron et al.*, 2007) along the lines of the SMOS soil moisture (L2) processor (referred to 'breadboards' hereafter) (*Kerr et al.*, 2011) is used in this study to simulate T_Bs from in situ soil moisture and auxiliary data. To account for mixed land cover pixels observed at large spatial scales in the breadboards different generic forward model versions with specific sets of default parameters exist for different land covers.

L-MEB is based on a simplified (zero-order) radiative transfer equation (*Wigneron et al.*, 1995) representing the soil as flat surface in contact with the atmosphere, and the vegetation as a homogeneous layer. According to the Rayleigh-Jeans Law in the microwave domain of the electromagnetic spectrum the radiation as measured by a radiometer is directly proportional to brightness temperature. T_B depends on incidence angle θ and polarization p (H or V) and is directly related to the physical temperature T and the emissivity e/reflectivity Γ:

$$\begin{aligned} T_B(\theta, p) &= e_{\theta,p} \cdot T \\ with\ \ \Gamma &= 1 - e \end{aligned} \tag{5.1}$$

As the received signal originates from various sources, T_B is a composite of the following terms: 1) the soil emission attenuated (scattered and absorbed) by the canopy layer, 2) the direct canopy emission, 3) the canopy emission reflected by the soil and again attenuated by the canopy, 4) the direct sky emission and 5) the sky emission reflected by the soil and twice attenuated by the canopy layer.

In L-MEB the sky contribution to T_B is calculated according to *Pellarin et al.* (2003), while the effects of soil and vegetation are described by the '$\tau - \omega$ model' (*Mo et al.*, 1982):

$$\begin{aligned} T_B(\theta, p) = (1 - \omega_{\theta,p})(1 - \gamma_{\theta,p})(1 + \Gamma_{\theta,p}\gamma_{\theta,p})T_v \\ +(1 - \Gamma_{\theta,p})\gamma_{\theta,p}T_{EFF} \end{aligned} \tag{5.2}$$

ω is the single scattering albedo of the canopy, γ describes the vegetation transmissivity, and T_v and T_{EFF} denote vegetation and soil effective temperature, respectively.

γ is calculated from the vegetation optical depth at nadir τ_{NAD}:

$$\gamma(\theta, p) = \exp(\tau_{NAD}/\cos\theta) \tag{5.3}$$

Jackson and Schmugge (1991) developed a linear relationship to estimate τ_{NAD} from the vegetation water content (VWC) and a vegetation parameter b, the latter being a function of canopy type/structure, sensor frequency, polarization and incidence angle:

$$\tau_{NAD} = b \cdot VWC \tag{5.4}$$

To account for effects of a dominant vertical vegetation structure a parameterization has been included to express τ_{NAD} as function of both incidence angle and polarization by means of the parameter pair tt_H and tt_V.

According to *Wigneron et al.* (2001) T_{EFF} is computed from the soil surface temperature and the deep soil temperature (~50 cm depth) with contributions of the two varying as a function of soil moisture.

Based on *Choudhury et al.* (1979) the reflectivity of a naturally occurring rough surface Γ is related to the reflectivity of a perfectly smooth surface (Fresnel reflectivity) Γ^*. The latter is linked to the dielectric properties of the soil through the Fresnel equations, which in turn are related to soil moisture by means of the Dobson dielectric mixing model (*Dobson et al.*, 1985) adjusted by *Peplinski et al.* (1995). The roughness correction of the reflectivity term is as follows:

$$\begin{aligned}\Gamma(\theta, p) = [(1 - Q_R)\Gamma^*(\theta, p) + Q_R\Gamma^*(\theta, q)] \\ \exp[-H_R \cos^{N_R}(\theta)]\end{aligned} \tag{5.5}$$

p and q denote H or V pol., respectively. H_R describes the intensity of the roughness effects, Q_R represents the polarization mixing effects, and N_R allows the modulation of the reflectivity as a function of the incidence angle. Distinguishing N_R for the two polarizations (i.e. N_{RH} and N_{RV}) led to improved results in *Escorihuela et al.* (2007) and *Wigneron et al.* (2007).

Roughness is primarily understood as a geometric effect. As many studies also reported a soil moisture dependency (e.g. *Wigneron et al.*, 2001; *Saleh et al.*, 2006b, 2007; *Escorihuela et al.*, 2007; *Merlin et al.*, 2009; *Panciera et al.*, 2009b) in the breadboards H_R is implemented as a piecewise function of soil moisture with two texture-dependent transition moisture values defining H_R and H_{R_Min}).

However, the recent study by *Escorihuela et al.* (2010) suggests that the dependency might merely result from a mismatch between sampling depth of conventional soil moisture sensors (5-6 cm) and the depth contributing to soil emission (<5 cm), as well as a weak performance of the Dobson dielectric mixing model in certain cases. The substitution of the latter with the Mironov model (*Mironov et al.*, 2004) is under investigation. While the Dobson model is empirically-derived from a limited number of data sets of differing soil types with sand fractions smaller than 50%, the Mironov model is physically-based on the refractive index and built upon modeled data sets spanning the entire range of potential

soil conditions up to pure quartz sand as well as some measured soil data sets. Large differences between the Dobson and Mironov implementations occur for high sand fractions and soil moisture conditions around 0.1-0.2 m^3/m^3. In this case, Mironov results in warmer T_Bs than Dobson (*de Rosnay et al.*, 2008). The Dobson model requires soil moisture, soil effective temperature, clay-%, sand-%, dry soil bulk density and solid particle density as input, the Mironov model only uses the first three.

For future build-in into L-MEB several H_R-parameterizations based on surface roughness measurements have been developed (*Choudhury et al.*, 1979; *Mo and Schmugge*, 1987; *Wigneron et al.*, 2001, 2011). The most recent was derived from a data set covering the entire range of surface roughness conditions expected on agricultural fields (S_D 4.57-59.37 mm) (*Wigneron et al.*, 2011):

$$H_R = (0.9437 S_D / (0.8865 S_D + 2.2913))^6 \tag{5.6}$$

Besides the soil characteristics (soil texture and bulk density), the choice of b/τ_{NAD} and H_R have most impact on the modeled T_Bs (e.g. *Pardé et al.*, 2004; *Grant et al.*, 2008; *Panciera et al.*, 2009a; *Cano et al.*, 2010).

5.4. Methods

5.4.1. Comparison at ground patch scale (2x2 km)

Modeling and scaling

For the comparison of ground and EMIRAD data at patch scale (2x2 km), all EMIRAD samples acquired over the respective patches (see Fig. 5.3b+c) were averaged to one value per patch, sampling date, for 0° and 40° antennas, H and V pol., respectively. For each campaign ground sampling point T_Bs were modeled at 0 and 40° θ, H and V pol. and subsequently averaged per respective sampling patch and date.

Given the high sand fractions and the comments in Section 5.3 the Mironov dielectric mixing model was applied throughout this study. Model parameter settings were individually set as a function of inherent land cover conditions recorded for each sampling point per patch and date. Using this information all points were allocated into the land cover classes listed in Table 5.3. The nominal generic forward model for low vegetation was applied for all classes except for 'coniferous forest' and 'trees' where the forest model was used. The respective default parameter settings were adjusted wherever updated findings from recent studies or field measurements for parameterization were available. Moreover, for the parameters with highest impact on the model output (soil moisture, texture, H_R and τ_{NAD}) a min-max range of possible values was defined. Based on findings from reviewed studies for the vegetation parameters values differing from the respective averages of these ranges seemed to be most likely. Thus, for b and τ_{NAD} such 'uni' values were selected (Table 5.3, literature/parameterized values depicted in normal/italic letters, resp.). More details on parameter choices will be given in the subsequent section.

Three different types of model runs were conducted: First, the spread in the modeled T_Bs as a result of spatial variability and uncertainties inherent in the most influencing parameters was visualized. Model runs were conducted for all possible combinations of minimum and

Table 5.3.: L-MEB roughness parameter (H_R) and vegetation optical depth at nadir (τ_{NAD}) for each land cover class, including in situ measurements (where available) to parameterize the former: standard deviation of the height (S_D) [mm]; vegetation water content (VWC) [kg/m^2] per campaign flight day linearly interpolated between the two sampling dates (average in case of agriculture grass); vegetation parameter (b). Normal, italic and bold font represent measured, literature and 'optimal' values, resp. Average/most likely value 'uni'(min-max range) are given in case of all measured values and for parameterized H_R/for b and τ_{NAD}, resp.

Land cover classes	Date	S_D	H_R	VWC	b	τ_{NAD}
Bare field			0.39(0.15-**0.58**)			0
Potato field bare		63.51 (57.71-69.31)	1.15(1.12-**1.17**)			0
Spring cereal	29/04	10.64 (5.65-15.63)	0.39(0.15-**0.58**)	0.021(0.014-**0.028**)	*0.11(0.08-**0.15**)*	0.002(0.001-**0.004**)
	02/05			0.054(0.032-**0.076**)		0.006(0.003-**0.011**)
	04/05			0.076(0.044-**0.108**)		0.008(0.004-**0.016**)
	09/05			0.131(0.074-**0.189**)		0.014(0.006-**0.028**)
Winter cereal	29/04		0.39(0.15-**0.58**)	0.564(0.451-**0.677**)	*0.11(0.08-**0.15**)*	0.062(0.036-**0.102**)
	02/05			0.786(0.657-**0.915**)		0.086(0.053-**0.137**)
	04/05			0.934(0.795-**1.074**)		0.103(0.064-**0.161**)
	09/05			1.305(1.138-**1.472**)		0.144(0.091-**0.221**)
Agriculture grass			0.39(0.15-**0.58**)	0.565(0.216-**0.913**)	*0.12(0.1-**0.3**)*	0.068(0.022-**0.274**)
Trees			*1.1(**1.0**-1.2)*			*0.65(**0.2**-1.0)*
Coniferous forest			*1.1(**1.0**-1.2)*			*0.65(**0.2**-1.0)*
Forest clearing			*1.1(**1.0**-1.2)*			0
Young forest			*1.1(**1.0**-1.2)*			*0.3(**0.2**-0.6)*
Natural grass	29/04		*0.8(0.5-**1.1**)*	**0.360**(0.123-0.598)	***0.12***(0.1-0.3)	**0.043**(0.012-0.179)
	02/05			**0.468**(0.156-0.779)		**0.056**(0.016-0.234)
	04/05			**0.539**(0.179-0.900)		**0.065**(0.018-0.270)
Scotch heather	29/04		*0.8(0.5-**1.1**)*	**0.512**(0.205-0.819)	***0.12***(0.1-0.3)	**0.061**(0.020-0.246)
	02/05			**0.591**(0.286-0.895)		**0.071**(0.029-0.268)
	04/05			**0.643**(0.341-0.945)		**0.077**(0.034-0.284)
Scotch heather/grass	29/04		*0.8(0.5-**1.1**)*	**0.351**(0.259-0.443)	***0.12***(0.1-0.3)	**0.042**(0.026-0.133)
	02/05			**0.433**(0.322-0.544)		**0.052**(0.032-0.163)
	04/05			**0.488**(0.364-0.611)		**0.059**(0.036-0.183)

maximum values of these parameters in addition to a model run where all parameters were set to their respective 'uni'/average values (referred to 'uc model run' hereafter).

Secondly, ideal values for H_R and τ_{NAD} for each land cover class (depicted in bold in Table 5.3) were determined by means of a set of model runs for all possible combinations of min, max and 'uni'/avg values of these two parameters (referred to 'H_R-τ_{NAD} model run' hereafter).

Third, the model was run with this 'optimal' set of parameters per land cover class (referred to 'opt model run' hereafter). Thereby, the results obtained using the Mironov dielectric mixing model were checked against model output using Dobson. Moreover, two sets of N_{RH}-N_{RV} pairs were tested against each other. Finally, the patch means of the modeled T_Bs obtained by simple averaging were compared with weighted patch averages. The latter were generated by allocating a weight to each ground sampling point's data based on the EMIRAD antenna pattern (*Skou et al.*, 2010a).

Choice of parameter settings and related uncertainties

For input to L-MEB average, maximum and minimum (+/- one standard deviation) values of the three calibrated mineral soil moisture probe readings were calculated per sampling point and date.

For the estimation of T_{EFF} surface (0-5 cm depth) and deep soil temperatures (50-55 cm depth) recorded at the time of the soil moisture sampling were extracted from three network stations situated within the respective patches. Coincident air temperature and pressure data at 2 m height was taken from the four closest DMI climate stations. Canopy temperature T_V was approximated by either 0-5 cm soil temperature or 2 m air temperature in case of low and tall vegetation ('coniferous forest' and 'trees') classes, respectively.

With respect to soil texture, the different scenarios (avg. sand-%/avg. clay-%, min. sand-%/max. clay-%, max. sand-%/min. clay-%) were defined on the basis of the site-specific texture analysis of the campaign samples.

For sampling points where a gravimetric sample was taken dry soil bulk density was calculated from the latter while in all other cases the average per patch and sampling date was applied. The solid particle density was set to the constant default value of 2.664 g/cm^3.

At L-band scattering effects are generally low. In all model runs the scattering albedo ω was set to the default values 0 and 0.08 for low vegetation and forest, respectively, according to e.g. *Pardé et al.* (2004); *Grant et al.* (2008).

'Uni' values and min-max ranges for τ_{NAD} are compiled in Table 5.3. In case of forest land cover classes they were based on *Ferrazzoli et al.* (2002); *Grant et al.* (2008). For all other classes with available VWC measurements, using Eq. (5.4) min-max ranges of τ_{NAD} were calculated by means of corresponding ranges of VWC and b values, while the 'uni' values of τ_{NAD} were estimated by the respective average VWC and 'uni' values of b. The VWC data (Table 5.2) was linearly interpolated between the two sampling dates to obtain a value range (avg. and min/max from interpolated standard deviation) per flight date (Table 5.3). In case of agriculture grass an average of the two available samples was taken. The b value ranges for crops and native grass (with litter) were based on *Jackson and Schmugge* (1991); *Van de Griend and Wigneron* (2004); *Schwank et al.* (2005); *Wigneron et al.* (2002, 2007); *Saleh et al.* (2007, 2009); *Panciera et al.* (2009a,b). For the not regularly cut agricultural grass as well as for heather the values of native grass were applied. Generally, the computed τ_{NAD} values seem to agree well with literature values for similar plant types and VWC at this time of the year. For example, the τ_{NAD}, b and VWC of 0.08, 0.114 and 0.7 kg/m^2, respectively, for winter rye in *Jackson and Schmugge* (1991) fit very well with our winter cereal data. The τ_{NAD} of 0.1 for mediterranean bushland in *Cano et al.* (2010) is within the range of our scotch heather values. For grass the VWC-τ_{NAD} relations in *Jackson and Schmugge* (1991) and *Saleh et al.* (2006b) (VWC ~0.2-0.8 kg/m^2 and τ_{NAD} ~0.1-0.3) match our maximum τ_{NAD} values very well, while the ones described in *Saleh et al.* (2007) for alfalfa and seeded clover grass without litter (VWC ~0.5-1.3 kg/m^2 and τ_{NAD} ~0.04-0.11) are in agreement with our 'uni' τ_{NAD} values.

Assuming polarization and incidence angle independence of the optical depth, tt_H and tt_V were both set to 1 throughout this study.

The soil moisture-dependent parametrization of H_R was neglected (i.e. H_R=H_{R_Min}) as it remains controversial (*Escorihuela et al.*, 2010). For the agricultural land cover classes with available surface roughness measurements, using Eq. (5.6) an average H_R value and a min-max range were computed by means of the average and min/max (-/+1 standard deviation) S_D values, respectively (Table 5.3). These values were adapted for the remaining agricultural classes based on similar appearance in terms of roughness. The calculated H_R values are higher than the SMOS L2 default for crops (0.2) which is in good agreement with recent studies by *Panciera et al.* (2009a,b); *Saleh et al.* (2009). For the heath classes ('natural grass', 'scotch heather', and 'scotch heather/grass') values were chosen based on *Saleh et al.* (2007, 2009); *Panciera et al.* (2009a); *Cano et al.* (2010). In case of the forest classes ('coniferous forest','forest clearing','young forest','trees') we adapted the findings of *Grant et al.* (2008).

In accordance with various studies (e.g. *Mo and Schmugge*, 1987; *Wigneron et al.*, 2001, 2011) Q_R was constantly set to 0.

No clear relation has yet been found between N_{RH} and N_{RV}. Generally, they lie between -2 and 2 with N_{RH} larger N_{RV}. *Wigneron et al.* (2011) pointed out that the N_R parameters may have strong impact on the emissivity at large θ. In agreement with previous studies they stated a ΔN_R (N_{RH}-N_{RV}) in the order of 2 for smooth fields. *Mialon et al.* (Accepted) recently discovered an inverse relationship between S_D and ΔN_R, as well as a trend towards lower N_R values with increasing S_D. Accordingly, N_{RH}=0 and N_{RV}=-1 were chosen for our sites with a tendency towards rough surface conditions. To span the range of reasonable assumptions this combination was tested against N_{RH}=2 and $N_{RV} = 0$ (SMOS L2 default) in the 'opt model runs'.

5.4.2. Comparison at SMOS pixel scale (44x44 km)

For T_B comparison at SMOS pixel scale, the airborne data of all ten flight tracks within the SMOS pixel was averaged per sampling day. Beside a simple mean, a weighted mean was created by taking the average SMOS antenna pattern into account (*Kerr et al.*, 2011). From the modeled T_B patch averages a weighted average over the SMOS pixel was estimated per sampling day by means of the SMOS radiometric land cover fractions. Using 'FNO' with shares of 90% and 10% for agriculture and heath, and 'FFO' for forest resulted in portions of 76.8%, 8.5% and 14.7%, respectively (see Sections 5.2.1 and 5.2.2). For the only campaign day with available 'clean' SMOS data, May 2, mean EMIRAD and modeled T_Bs were compared with the L1C product over the entire incidence angle range. Precedent, curves were fitted through all available H and V SMOS T_Bs (best-fit second-order polynomial forced to meet at 0° θ) in order to represent the actual angular signature of the pixel and to have complete data over all angles.

5.5. Results and Discussion

5.5.1. Comparison at ground patch scale (2x2 km)

uc model run

Fig. 5.4 shows the results of the modeled T_Bs from the 'uc model run' for all patch types, sampling dates, H and V pol., 0 and 40° θ, respectively. The small temporal variability of soil moisture conditions during the campaign is reproduced in the modeling results as well as in the EMIRAD data with T_Bs in a very narrow interval. Also, the stronger precipitation-moisture response on the agricultural site without the presence of a dampening organic layer can be recognized in the figure despite the lack of distinct rain events during the studied period. As mentioned in Section 5.2.2 one can observe a differing behavior of the 40V channel over all patch types. In fact, this is the case for all results presented in this subsection. As all other channels consistently show similar performance, we legitimate to solely base our findings on the latter. However, to be exhaustive the results of the 40V channel will be included.

Fig. 5.4 illustrates that indeed a vast range of modeled T_Bs emanates from pronounced spatial variability in the geophysical input parameters (soil moisture and texture) as well as the large uncertainty in the choice of the tuning parameters (H_R and τ_{NAD}). This spread is observable throughout all patch types, sampling dates, polarizations and incidence angles. It is constantly smaller in case of forest (around 5-15 K) compared to the heath and agriculture

patches (around 10-20 K), and least pronounced for the 40° V pol. (around 5-10 K) while strongest in the 40° H pol. (around 10-20 K). The smaller T_B-range in case of forest can be explained by the higher degree of homogeneity in terms of land cover - while the agriculture patch consists of a pattern of fields with varying crop types at altering development stages, and the heathland includes some forested clusters, the forest patch is mostly made up of a closed structure of the same tree type (Fig. 5.1c-e). The fact that H_R and τ_{NAD} are chosen as a function of land cover for each point leads to a broader parameter range in case of agriculture and heath compared to forest (see Table 5.3).

Beside the spread, particularly striking in Fig. 5.4 is the clear tendency of the model to underestimate the EMIRAD T_Bs in case of agriculture and to a smaller extent in the heath data while the opposite trend is observed for the forest. This issue will be resumed shortly. Meanwhile, we would like to point out that despite the large spread in T_Bs, apparently the modeled ground data can be brought into agreement with the EMIRAD data under certain parameter constellations throughout all sampling patches, dates, and configurations. To locate 'ideal' H_R-τ_{NAD} combinations was the goal of the 'H_R-τ_{NAD} model runs'.

$\mathbf{H_R - \tau_{NAD}}$ model run

Table 5.4 summarizes the runs with smallest RMSE values between modeled and EMIRAD T_Bs for each polarization, θ and patch type. It stands out that combinations of $H_R$max-τ_{NAD}max, $H_R$min-τ_{NAD}min, and $H_R$max-τ_{NAD}uni clearly give best results in case of agriculture, forest and heath, respectively.

Table 5.4.: 'H_R-τ_{NAD} combinations of 'H_R-τ_{NAD} model runs' with smallest RMSE [K] compared to EMIRAD T_Bs (from all possible combinations of min, max and 'uni'/avg values of the two parameters) for all respective configurations of incidence angles, polarizations and patch types.

Configuration	Parameter combi	RMSE
0H Agricult	$H_R$max-τ_{NAD}max	5.82
40H Agricult	$H_R$max-τ_{NAD}max	4.63
0V Agricult	$H_R$max-τ_{NAD}max	4.86
40V Agricult	$H_R$uni-τ_{NAD}max	2.74
0H Forest	$H_R$min-τ_{NAD}min	3.14
40H Forest	$H_R$min-τ_{NAD}min	2.12
0V Forest	$H_R$min-τ_{NAD}min	3.23
40V Forest	$H_R$min-τ_{NAD}max	6.67
0H Heath	$H_R$max-τ_{NAD}uni	1.21
40H Heath	$H_R$max-τ_{NAD}uni	1.85
0V Heath	$H_R$max-τ_{NAD}uni	1.16
40V Heath	$H_R$uni-τ_{NAD}min	1.43

In case of the agriculture classes high H_Rs are concordant with literature findings (e.g. *Panciera et al.*, 2009a,b; *Saleh et al.*, 2009) which even propose higher values than the ones used in this study. Further increasing H_R in our case would actually counteract the tendency of underestimating EMIRAD T_Bs. At the same time the SMOS L2 default H_R value for crops is much lower (0.2) indicating smoother conditions. The fact that the surface could appear significantly less rough from the large-distance perspective of SMOS compared to

the much shorter one of airborne radiometers is plausible and suggests scale-dependency of the roughness parameter.

Apart from the 40V channel, RMSEs between modeled and measured T_Bs are markedly smaller in case of heath and forest than for the agriculture site. Indeed, we would expect the opposite since in case of the agriculture site data and model parameters correspond best to true conditions as a results of: (1) most accurate ThetaProbe calibration due to less spatial variability in the underlying data and significantly more data points (denser sampling spacing and additional sampling day), (2) the most important tuning parameters were parameterized from in situ measurements while for some forest and heath classes even literature values were sparse or unavailable, (3) presence of much more pronounced vegetation layers superimposing soil emission as well as distinct moss/organic layers with significantly higher water contents on top of the mineral soil (*Bircher et al.*, 2010) at the heath and forest sites. Recalling L-band signal penetration depths of < 5 cm for wet soils implies that emissions captured by radiometers originate with maximum likelihood solely from these overlying layers. This suggests that our model runs are driven by too low soil moisture which should result in too high modeled T_Bs compared to the EMIRAD data. As yet, we are obtaining a very good fit for some of the model runs, certain model parameters must compensate the bias resulting from these not considered effects. It might stand to reason that H_R and/or b/τ_{NAD} are taking over this role as smallest RMSEs between modeled and EMIRAD T_Bs for the forest and heath patches were achieved by setting both or either of the two to minimum or 'uni' instead of maximum values as in case of agriculture. The effect is most pronounced for the forest patch, where densest vegetation and thickest organic layers are found. It will be of high interest to investigate this further by taking the organic layer data into account and not only run L-MEB in forward mode, but retrieve parameters using the knowledge gained so far to constrain the model.

opt model run

Fig. 5.5 presents the results of the 'opt model runs' with H_R and τ_{NAD} set to the 'optimal' values depicted in bold in Table 5.3. The first and second columns show EMIRAD T_Bs plotted against modeled T_Bs for 0 and 40° θ, H and V pol., respectively, using either the Dobson or Mironov dielectric mixing models. The better performance using Mironov for the environemental conditions prevalent in our study area clearly stands out, with significantly smaller RMSE values over all patch types of 4.25/3.45/3.77 K compared to the ones using Dobson of 12.11/11.01/11.27 K for the 0H, 40H and 0V channels, respectively.

The third column of Fig. 5.5 shows EMIRAD T_Bs plotted against modeled T_Bs for the 40° θ, H and V pol., respectively, using either N_{RH}=2/0 or N_{RV}=0/-1. At nadir the RMSE over all patches remains unchanged between the two scenarios (not shown). In the 40° H pol. it improves significantly from 15.67 K for N_{RH}=2/N_{RV}=0 to 3.45 K for N_{RH}=0/N_{RV}=-1, clearly confirming our choice of the latter.

Furthermore, we can see in Fig. 5.5 that the errorbars resulting from averaging the point-wise modeled T_Bs are significantly larger than in case of the averaged EMIRAD samples. Unlike in the 'uc model run', in the 'opt model run' T_B data the spread is not taking uncertainty inherent in the input parameters into account, but only reflects spatial variability of environmental conditions encountered at point-scale. The latter is larger than the spatial variability in T_Bs recorded by EMIRAD at patch scale.

Finally, an impact of a simple versus a weighted mean (by means of the EMIRAD antenna pattern) could not be detected. Resulting RMSE values of 4.25/3.45/3.77/6.72 and 4.43/3.37/3.93/6.85 K for H0, H40, V0, and 40V simple/weighted mean, respectively, show no significant change between the two.

The pronounced spread in the modeled T_Bs certainly complicated the comparison between the ground and airborne data. However, we were able to overcome this constraint by the chosen approach which, to our believe, augmented the probability of a plausible data set and parameter choice due to the following reasons: (1) Based on preceding spatial analysis the ground sampling patches were carefully selected to represent prevailing environmental conditions, and in turn the patches were sampled as densely as possible under given financial and temporal constraints. This should result in trustful spatial averages to typify respective patch conditions. (2) A well-established forward model that has been validated several fold in other regions was applied point-wise to our solid data with model and parameter settings based on up-to-date literature and (where available) in situ measurements plus state-of-the-art parameterizations. After locating a reliable parameter combination for each land cover class the EMIRAD T_Bs could be reproduced well throughout all patch types and sampling dates. This clearly demonstrates the advantages of a stepwise validation over spatial scales, as the approach would not have been feasible with a direct jump from point to SMOS pixel scale.

5.5.2. Comparison at SMOS pixel scale (44x44 km)

Table 5.5 lists EMIRAD T_Bs per sampling day averaged over all ten flight tracks within the SMOS pixel by means of a simple and weighted average (SMOS antenna pattern) for 0° and 40° θ and H and V pol., respectively. As in case of the modeled ground data the application of the weighted mean did not alter the results for any of the measurement configurations on either of the dates. Thus, in the following comparison only the EMIRAD simple mean was considered.

Table 5.5.: EMIRAD-2 brightness temperatures [K] of all 10 flight tracks within the SMOS pixel around grid node 2002029: simple and weighted average (standard deviation) per sampling day, for H and V pol., 0 and 40° incidence angles, resp.

	0 H		0 V		40 H		40 V	
	Simple	Weighted	Simple	Weighted	Simple	Weighted	Simple	Weighted
29/04	249.03(6.75)	248.88(4.29)	248.85(6.66)	248.67(4.22)	238.35(7.23)	238.46(4.62)	257.55(5.08)	257.55(2.71)
02/05	244.11(6.93)	243.86(4.33)	243.96(6.96)	243.73(4.35)	234.13(7.88)	233.96(5.35)	252.95(5.22)	252.83(3.06)
04/05	248.13(6.12)	248.03(3.64)	247.95(6.08)	247.82(3.59)	238.73(6.57)	238.66(3.98)	255.66(4.78)	255.6(2.36)
09/05	244.87(7.14)	244.8(4.21)	244.9(7.02)	244.81(4.19)	235.55(8.14)	235.6(5.26)	253.8(5.08)	253.8(2.76)

Fig. 5.6 depicts all available T_B data (H and V pol.) at SMOS pixel scale on the only RFI-free campaign day, May 02: EMIRAD T_Bs recorded over all ten flight tracks within the Danish validation site (integrated to 1 second and overall average for 0° and 40° θ, respectively), the weighted mean of the modeled patch average T_Bs (0°-60° θ) as well as the SMOS L1C TOA (ascending overpass) data of node 2002029 (all observed θ including fitted curves). With respect to SMOS data the deviations from the actual angular signature of the pixel (fitted lines) reflect the aforementioned unresolved image reconstruction issues and potentially still present soft RFI, especially pronounced in the low incidence angles originating from the only

near alias-free part of the field of view. The issue is under investigation and ameliorations can be expected in the future.

In the figure it stands out that the EMIRAD T_B data has a scatter in the order of 20 K in both polarizations and incidence angles representing the encountered spatial variability of land surface conditions within the SMOS pixel. The measured SMOS and EMIRAD data lie in comparable range. Comparison between the fitted SMOS curves and EMIRAD data reveals RMSE values of 8.56, 9.30 and 12.85 and 8.27 K for 0° H, V and 40° H, V, respectively, with a positive bias of the airborne data. The comparison at nadir has to be taken with care as the SMOS data is extrapolated at this point. A much more distinct positive bias is observed for the averaged modeled patch T_Bs with respect to the SMOS data. RMSE calculated between the fitted SMOS curves and the modeled patch data over the 0-60° θ range gives values of 16.60 and 15.14 K for H and V pol., respectively.

The observed biases for both, modeled patch and EMIRAD T_Bs must arise from a combination of various error sources inherent in the different measurements and the model. Partly, they can be explained by scale effects. The patches chosen for the campaign ground sampling are representative for the entire SMOS pixel in terms of land cover, but to less extent in terms of prevailing soil types: All three patches exhibit very high sand fractions while in the eastern-most part of the SMOS pixel soils with significantly higher clay fractions and consequently increased moisture contents are met. An average of the modeled patch T_Bs weighted by means of the prevailing land cover fractions results in a too high value at SMOS pixel scale indicating too dry moisture conditions. Another fraction of the large bias in case of the modeled data could also be provoked by scale-dependency of the H_R value as suggested in the previous section. Under this assumption, creating a SMOS pixel scale average of our modeled data based on the high H_R values applicable for patch scale would then naturally result in T_B overestimation at the larger scale. With the airborne data 35% of the SMOS pixel could be covered per sampling day given the temporal and financial constraints. Flight tracks were chosen to cover a maximum number of network stations, which in turn were spatially distributed according to respective fractions of prevailing land cover and soil types within the pixel. Thus, T_Bs were also measured over parts of the more clayey eastern areas. *Rüdiger et al.* (2011a) found that for a heterogeneous land surface typically a minimum of 50% airborne coverage of the SMOS pixel were required for an expected sampling error of less than 4 K (design sensitivity of SMOS). Our deviations exceeding the 4 K error band might thus partly be explicable by a spatial coverage of the SMOS pixel with EMIRAD data below this requisite. However, the bias between SMOS and EMIRAD T_Bs is clearly reduced compared to the one observed for the modeled patch average. Once more this underlines the advantage of a stepwise comparison through spatial scales over a direct jump from the ground data to SMOS pixel scale.

Evidently, no sound conclusions about SMOS data quality for this area can be drawn from this single-day comparison. An attempt was made to relate the L1C data of the other six 'clean' SMOS overpasses (April 19 and 27, and May 10, 12, 15 and 17) to airborne and ground campaign data (not shown). Unfortunately, this turned out to be of limited significance as all of the available SMOS data sets stem from days at the margin or outside the campaign period. At first glance, SMOS T_Bs seem to generally reflect the precipitation/soil moisture conditions throughout this month, but as the dynamic is weak this needs to be analyzed more closely. Certainly, this is a promising start for investigations currently ongoing by means of the long-term soil moisture network observations available for the area.

The network data will help to overcome the constraints encountered through the temporal limitations of the campaign approach, i.e. small temporal soil moisture variability and RFI contamination. Profiting by the important findings from the airborne campaign data of high spatial coverage and density, the network data can support the link throughout spatial and temporal scales: The data of each overflown station can be compared with EMIRAD data, while the network average should be directly relatable to SMOS time series as the stations were distributed to serve this purpose.

5.6. Conclusions and outlook

Within the framework of HOBE an airborne SMOS Cal/Val campaign with the passive L-band radiometer EMIRAD-2 was carried out in the Skjern River Catchment, Denmark, between April 26 and May 9, 2010. Four flights centered at SMOS ascending overpass were conducted within one selected SMOS pixel (44x44 km). Surface soil moisture of the mineral as well as the organic layers, vegetation water content and roughness were measured within three 2x2 km patches (~EMIRAD footprint) of differing land cover. By means of this data set the objective of this article was to present the validation of SMOS L1C T_B data of one pixel. Data was compared at different spatial scales: (1) averaged modeled ground data and EMIRAD data at patch scale (2x2 km), (2) averaged modeled ground data, EMIRAD data and SMOS data at SMOS pixel scale (44x44 km). L-MEB was used to point-wise model T_Bs from in situ soil moisture (mineral soils only) with parameter choice based on literature as well as parameterization using campaign measurements.

Three sets of model runs were conducted to (1) assess the spread in the modeled T_Bs as a result of parameter uncertainties and variability, (2) to determine 'ideal' values for H_R and τ_{NAD}, and (3) to test the performance of the Mironov dielectric mixing model against the one of Dobson, as well as two different N_{RH}/N_{RV} pairs using an 'optimal' set of model parameters. At both scales, the benefit of a weighted average by means of the EMIRAD/SMOS antenna patterns, respectively, over a simple mean were investigated. The 'uc model run' resulted in a considerable range of T_Bs up to ~20 K. Nevertheless, under certain parameter constellations our modeled ground data agreed with the EMIRAD data on all sampling patches, campaign dates, for both polarizations and incidence angles, respectively. The 'H_R-τ_{NAD} model run' showed that combinations of $H_R$max-τ_{NAD}max, $H_R$min-τ_{NAD}min, and $H_R$max-τ_{NAD}uni gave smallest RMSEs (5.1, 2.8 and 1.4 K on average) between modeled and EMIRAD T_Bs for agriculture, forest and heath, respectively. Lowering the values from the maximum in case of forest and heath compensates for the not considered wet organic material on top of the mineral layers. Modeled T_Bs from the 'opt model run' could be brought in good agreement with EMIRAD data when the Mironov dielectric mixing model was used (RMSE of 3.8 K on average), while applying Dobson gave significantly higher RMSE values of 11.5 K on average. Using an N_{RH}/N_{RV} combination of 0/-1 instead of 2/0 decreased the RMSE in the 40° H channel from 15.7 to 3.4 K.

As the SMOS data turned out to be heavily RFI-contaminated throughout the campaign, SMOS pixel scale comparison could only be carried out for May 2. For this day SMOS and EMIRAD T_Bs lie in comparable range with average RMSE of 9.7 K, while the RMSE between SMOS and averaged modeled patch T_Bs is 15.9 K on average. The clearly larger

positive bias of the latter can be explained by scale effects as the SMOS pixel average is estimated from three 2x2 km patches only.

Neither using the EMIRAD antenna pattern to weight the average of the modeled T_Bs nor the SMOS antenna pattern to estimate a weighted mean of EMIRAD data over the SMOS pixel did improve the results over applying simple means.

Beside the ability to reproduce EMIRAD measurements by means of modeled T_Bs, we can similarly claim that EMIRAD and SMOS data show good accordance on May 2. This study gives evidence for the suitability of a stepwise SMOS validation approach and demonstrates the advantages of solid data sets of high spatial coverage and density throughout spatial scales. At the same time the limitations of the approach due to temporal constraints (weak soil moisture dynamic and heavy RFI-contamination during the short time window) become apparent. At this point no final statement on SMOS data quality over the Danish Cal/Val site can be drawn. Investigations on the SMOS L1C data as well as L2 soil moisture data are ongoing by means of the soil moisture network observations. Profiting by the important findings from the airborne campaign the network data can further support the link throughout spatial scales while at the same time bridging longer temporal scales. Once the confidence in the reliability of SMOS data at the studied grid node is more firmly established, the validation activities will also be expanded to surrounding nodes with higher open water fractions. Furthermore, the attempt of retrieving currently unavailable model parameters for the organic layer is planned by means of the collected ground data and the knowledge gained so far.

Acknowledgments The project is funded by the Villum Kann Rasmussen Foundation and the Technical University of Denmark. Special thank goes to the HOBE members involved in the campaign organization and the ground sampling teams who did an excellent job. We would also like to thank the SMOS team at CESBIO for valuable discussions and providing codes for modeling and data processing, as well as CESBIO and AALTO University for the supply of ThetaProbes.

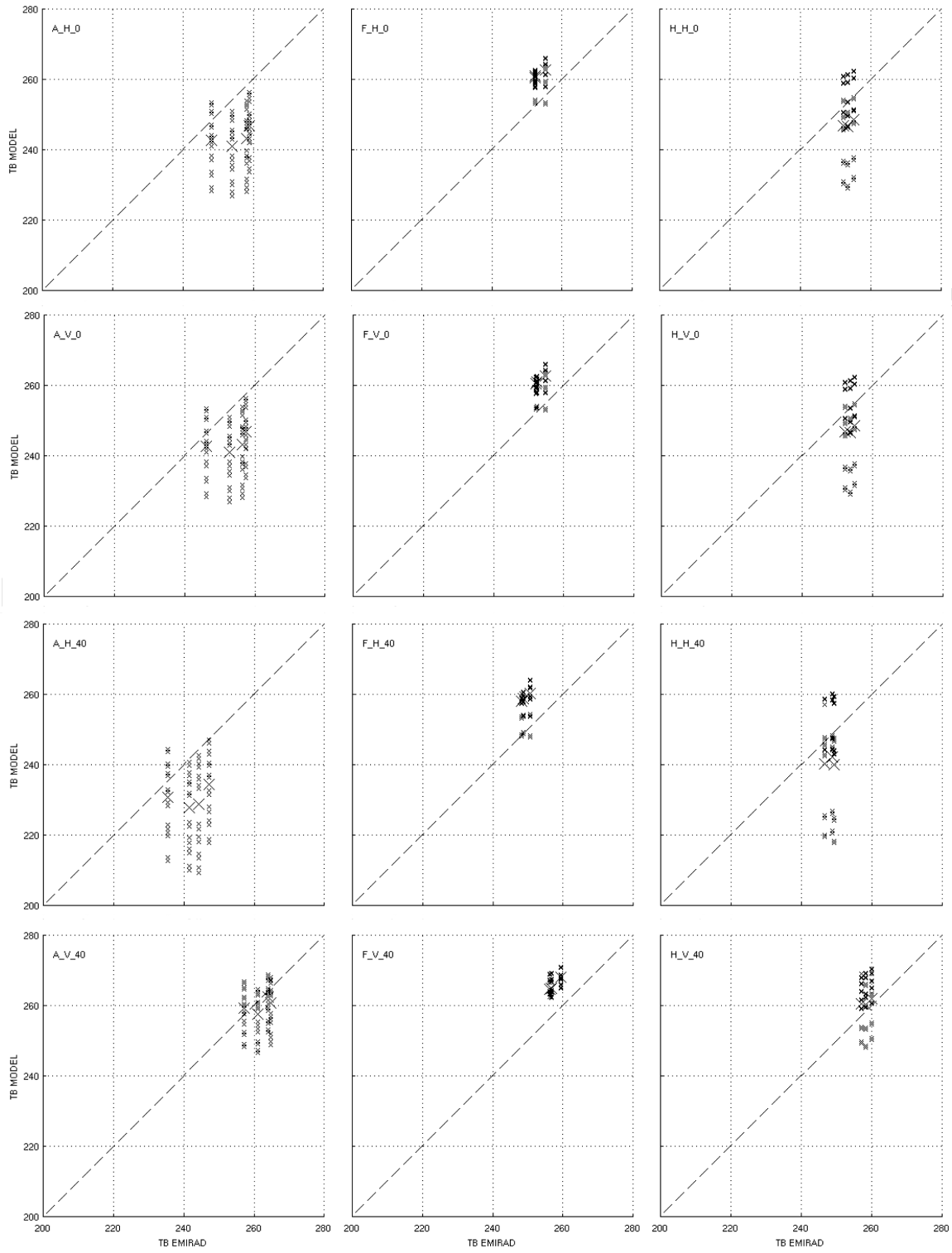

Figure 5.4.: Modeled ground data vs. EMIRAD brightness temperatures [K], 'uc model runs' using all possible combinations of min/max values (black x) for 4 selected parameters (soil moisture, texture, H_R and τ_{NAD}) including the 'uni/avg-run' (black X) for all patch types and sampling dates. First labeling letter of individual plots: A=Agriculture, F=Forest, and H=Heath; second labeling letter: polarization; Number in labels: incidence angle.

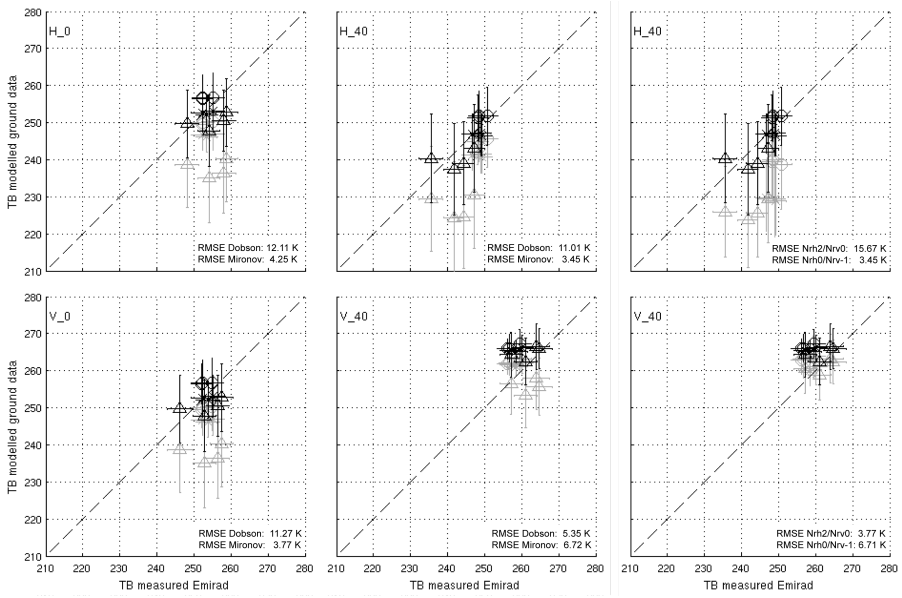

Figure 5.5.: Modeled brightness temperatures T_B [K] from the 'opt model runs' averaged per patch vs. EMIRAD T_Bs for all sampling dates and patch types, resp., using the Mironov(black)/Dobson(grey) dielectric models and N_{RH}=0/N_{RV}=-1 at 0 and 40° θ (1st and 2nd columns, resp.), as well as N_{RH}=2/N_{RV}=0(grey)/N_{RH}=0/N_{RV}=-1(black) and the Mironov model at 40° θ (3rd column), for H and V pol. (top and bottom row, resp.): agriculture (△), forest (◯), heath (X); errorbars depict standard deviations of the point-wise modelled and EMIRAD T_Bs averaged over the corresponding patches and dates, resp.

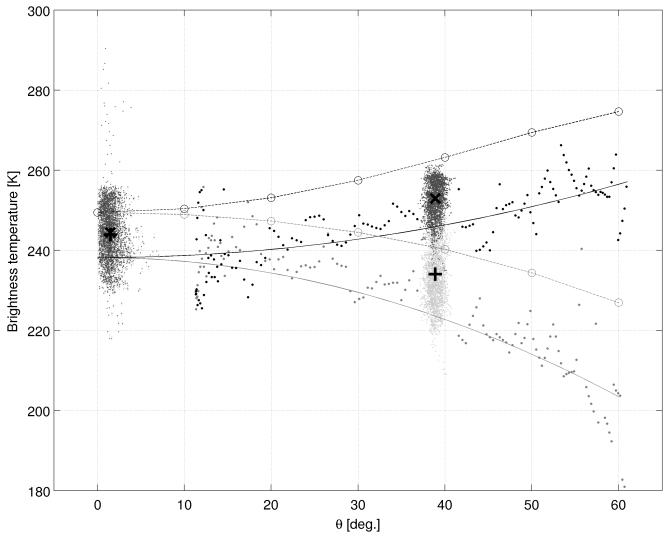

Figure 5.6.: All available brigthness temperature (T_B) [K] data over all incidence angles (θ) [°] on May 2: SMOS L1C TOA (ascending overpass) T_B of grid node 2002029 H/V pol. (grey/black dots) including fitted curves H/V pol (grey/black –), EMIRAD T_Bs of all 10 flight tracks integrated to 1 sec. H/V pol. (grey/black clusters), simple mean H/V pol. (black +/x), and weighted mean (76.8% agriculture, 14.75% forest, 8.5% heath) of modeled patch average T_Bs H/V pol. (grey/black -○-).

6. A soil moisture and temperature network for SMOS validation in Western Denmark (Paper 3)

Bircher, S., Skou, N., Jensen, K. H., Walker, J. P. and Rasmussen, L.

Paper submitted to: Hydrology and Earth System Sciences, October 2011

AbstractThe Soil Moisture and Ocean Salinity Mission (SMOS) acquires surface soil moisture data globally, and thus product validation for a range of climate and environmental conditions across continents is a crucial step. For this purpose, a soil moisture and temperature network of Decagon ECH2O 5TE capacitance sensors was established in the Skjern River Catchment, Denmark. The objectives of this article are to describe a method to implement a network suited for SMOS validation, and to present sample data collected by the network to verify the approach. The design phase included (1) selection of a single SMOS pixel (44x44 km), which is representative of the land surface conditions of the catchment and with minimal impact from open water (2) arrangement of three network clusters along the precipitation gradient, and (3) distribution of the stations according to respective fractions of classes representing the prevailing environmental conditions. Overall, measured moisture and temperature patterns could be related to the respective land cover and soil conditions. Texture-dependency of the 0-5 cm soil moisture measurements was demonstrated. Regional differences in 0-5 cm soil moisture, temperature and precipitation between the north-east and south-west were found to be small. A first comparison between the 0-5 cm network averages and the SMOS soil moisture (level 2) product is in range with worldwide validation results, showing comparable trends for SMOS retrieved/initial soil moisture and initial temperature (R^2 of 0.49/0.67 and 0.97, respectively). While retrieved/initial soil moisture indicate significant under-/overestimation of the network data (biases of -0.092/0.057 m^3/m^3), temperature is in good agreement (bias of -0.2 °C). Consequently, the network performs according to expectations and proves to be well-suited for its purpose. The discrepancies between network and SMOS soil moisture will be subject of subsequent studies.

6.1. Introduction

The assessment of water resources is vital under changing climate and land use, especially when coupled with a steadily increasing population (e.g. *FAO-Aquastat*, 2003). Climate and hydrological models constitute important tools for such investigations, but their reliability is constrained due to uncertainty in important input parameters. One of the key variables is soil moisture, as it significantly impacts water and energy exchanges at the land surface-atmosphere interface, and it represents the main source of water for agriculture and natural vegetation. However, soil moisture is highly variable in space and time and across scales, as a result of spatial heterogeneity in soil and land cover properties, topography and climatic drivers (*Famiglietti et al.*, 1998; *Mohanty et al.*, 2000; *Western et al.*, 2002) rendering it very difficult to assess. Thus, observations of soil moisture at appropriate spatial and temporal scales are urgently needed.

The Soil Moisture and Ocean Salinity satellite (SMOS, *Kerr et al.*, 2001) is the first mission dedicated to soil moisture measurements. A multi-angle, fully polarimetric passive L-band microwave radiometer (1.4 GHz) on board the satellite offers unprecedented possibilities for retrieving surface soil moisture data (∼0-5 cm depth) of global coverage every three days at a spatial resolution of ∼44 km. However, SMOS data quality is potentially affected by Radio Frequency Interferences (RFI), unresolved image reconstruction issues, errors in both the retrieval algorithm and related input. Thus, it is important that the SMOS algorithm and its associated products be validated by independent in situ measurements across a range of climatic regions.

Generally, such comparisons are complicated by scale-mismatch between the large satellite footprints and the point measurements on the ground (*Cosh et al.*, 2004), entailing the necessity of a high number of distributed observations of the latter to accurately represent the satellite scale. Continuous soil moisture networks have recently evolved across all continents and constitute a core activity in the validation of SMOS data: e.g. USA (*Bosch et al.*, 2006; *Schaefer et al.*, 2007; *Jackson et al.*, 2010); Canada (*Champagne et al.*, 2010); Australia (*Walker et al.*, 2001; *Merlin et al.*, 2008); Africa (*de Rosnay et al.*, 2009); Europe - Spain (*Martinez-Fernandez and Ceballos*, 2003), France (*Calvet et al.*, 2007), Germany (*Krauss et al.*, 2010; *Bogena et al.*, 2010). Many of them can be found in the International Soil Moisture Network Database (*Dorigo et al.*, 2011). These networks often face constraints with respect to their density or spatial extent (*Cosh et al.*, 2004). Various upscaling techniques have evolved to derive spatial patterns at large scales, e.g. interpolation (*Bardossy and Lehmann*, 1998), time/rank stability (*Vachaud et al.*, 1985), statistical transformation (*Reichle and Koster*, 2004; *De Lannoy et al.*, 2007), and land surface modeling (*Crow et al.*, 2005). However, these methods are sometimes themselves vulnerable to coarse spacing or limited extent of in situ data, often requiring costly long-term pre-studies. Methods to a priori design networks in a spatially representative manner would be beneficial. *Friesen et al.* (2008) presented an approach of area-weighted sampling by means of landscape units (hydrotopes) with internally more consistent hydrologic behavior, whereby variance and bias in the large-scale in situ soil moisture average can be reduced. The method was successfully applied in two short-term campaigns in West Africa. However, it is both region-dependent and quite complex.

Several studies have focused on the number of samples required to estimate the satellite footprint-scale mean. It was noted that soil moisture variability increases with the spa-

tial extent of a footprint, implying an increase in the necessary number of measurements (*Western and Bloeschl*, 1999; *Famiglietti et al.*, 1999, 2008). *Brocca et al.* (2007) found that a minimum of 15 to 35 point samples were required for terrain of negligible to significant topography and an extent of around 5000-10000 m^2. *Famiglietti et al.* (2008) found a maximum of 30 samples to be required at the 50 km scale assuming independent and spatially uncorrelated data.

A SMOS validation site has been established in the Skjern River Catchment in Western Denmark (*Bircher et al.*, Accepted). In the framework of the Hydrological Observatory (HOBE, `www.hobe.dk`, *Jensen and Illangasekare*, 2011), a soil moisture and temperature network with 30 stations was installed in fall 2009 within one SMOS pixel (44x44 km) covering large parts of the catchment. In this context, the objectives of this article are (1) to describe a method for the design and implementation of a soil moisture network suited for SMOS validation, and (2) to present the network data set and some analysis including a first comparison with SMOS data to verify the feasibility of our approach, as well as the reliability of the collected data.

The design is split into the selection of (1) an appropriate SMOS pixel, (2) three network clusters within the pixel, and (3) suitable network locations within the clusters. In step 3, a method similar to *Friesen et al.* (2008) is applied with distribution of the individual stations according to the respective fractions of the prevailing environmental conditions. *Friesen et al.* (2008) defined the main landscape units a priori, which introduces a risk to exclude important features from the start. In our much simpler method all environmental information is going into the analysis unchanged, whereupon the most important landscape units of the region are detected. Following this approach, it is anticipated that a priori the likelihood of obtaining a representative large-scale in situ soil moisture average for comparison with SMOS data is strongly enhanced.

6.2. Study area

The Skjern River Catchment is situated in Western Denmark and covers an area of approximately 2500 km^2 (Fig. 6.1). The climate in the region is temperate-maritime with winter and summer mean temperatures of around 2 and 16 °C, respectively, and an approximate annual precipitation between 800 to 900 mm. The eastern margin of the catchment is situated at the rim of the ice sheet during the latest glacial advance with mainly loamy soils on undulating calcareous tills. The remaining part comprises the primal fluvioglacial outwash plain consisting of low-relief sandy soils and sediments, while poorly drained basins have been filled with organic material (*Greve et al.*, 2007).

The predominant naturally occurring soil type is podsol with a bleached quartz-rich eluviation zone (topsoil) and an illuvation zone (subsoil) usually composed of a hardpan with a black humus-rich band and a subjacent orange-brown layer of sesquioxides with often distinct mottling (*Scheffer and Schachtschabel*, 2002). While water drains quickly through the sandy topsoil, this very firm hardpan is almost water tight causing ponding of water at its surface. When fertilized, limed and irrigated high-yield cultivation is possible; this is the case in the major part of the Skjern River Catchment. Intermixed are patches of natural vegetation, i.e. grassland, heath and spruce plantations with pronounced raw humus lay-

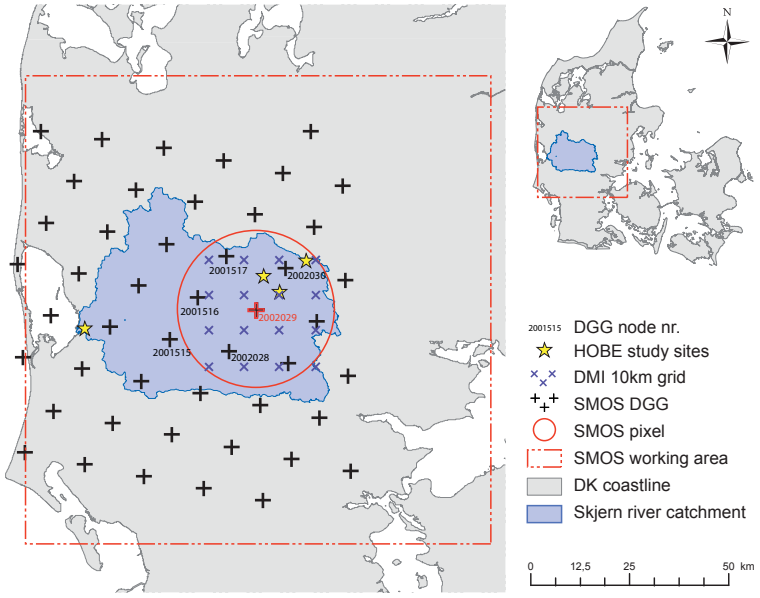

Figure 6.1.: Skjern Catchment in Western Denmark, HOBE study sites, SMOS Discrete Global Grid (DGG) nodes including numbers of eligible nodes, selected SMOS pixel and corresponding working area around grid node 2002029, and DMI 10 km precipitation grid within SMOS pixel.

ers (typically found on podsols). The area is sparsely populated with scattered farms and villages.

Within the catchment four study sites were chosen for the HOBE project (*Jensen and Illangasekare*, 2011, Fig. 6.1) to assess a wealth of hydrological parameters. The catchment is well-covered with climate and weather stations operated by the Danish Meteorological Institute (DMI). The 24-hour precipitation sums presented in this article are extracted from the DMI 10x10 km precipitation grid nodes (*Scharling*, 1999) contained within the SMOS pixel (Fig. 6.1). For each day the shelter correction factor of the corresponding month (category B) is applied to the data (*Vejen et al.*, 2000).

6.3. Data

6.3.1. Network data

A total of 30 Decagon ECH2O data loggers (*Decagon Devices*, 2002) were installed, each holding three ECH2O 5TE capacitance sensors measuring soil moisture, temperature, and electrical conductivity (*Decagon Devices*, 2008)[1]. The 5TE sensors were considered to be a cost-effective solution for large network applications. They are well-suited for measurements in the near-surface layer and they provide integrated measurements over approximately 5-6 cm when installed horizontally (0.3 l measurement volume). Accuracies in mineral soils are +/- 0.03 and +/- 1 °C for water content and temperature, respectively. Using the empirical

[1]Mention of manufacturers is for the convenience of the reader only and implies no endorsement on the part of the authors

calibration equation of *Topp et al.* (1980) volumetric water content is derived from dielectric permittivity, which in turn results from a 5 point dielectric calibration.

The TE sensors (predecessors of 5TE) were excessively tested in soils ranging from 3-100% sand/0-53% clay and salt-water solutions of electrical conductivities from 1 to 12 dS/m by *Kizito et al.* (2008). They found little probe to probe variability and sufficiently small sensitivity to temperature and electrical conductivity so that one single calibration curve was applicable for all studied conditions. Similarly, for the 5TE sensor type *Vasquez and Thomsen* (2010) found the Topp equation to be accurate within +/-0.02 in the 0-0.5 m depth range at the HOBE agriculture site Voulund (where one network station was placed).

Famiglietti et al. (2008) pointed out, that though site-specific calibration is ideal it is impractical for studies with large sensor numbers distributed over a considerable spatial extent. In their 50km-scale survey they applied a generalized calibration method with an accuracy of +/-0.03 to the entire set of probes, and likewise, this was done by *Brocca et al.* (2010).

Given the above findings, the Decagon 5TE calibration equation (*Topp et al.*, 1980) has been applied to the network. The given accuracy has been confirmed by some independent testing (addressed in Sections 6.4.3 and 6.5.1).

6.3.2. SMOS data

The SMOS measurement and soil moisture retrieval concept is complex and will be described to the extent required for understanding the presented work. For further information reference is made to *Kerr et al.* (2001, 2011).

The radiation collected by the SMOS radiometer is emitted from the area illuminated by the antenna directional gain pattern (working area, ∼123x123 km). Measurements are made at horizontal and vertical polarizations (H and V) and incidence angles ranging from around 0 to 60° as the satellite passes over the terrain. The working area is characterized by a weighting function resulting in a -3 dB footprint of approximately 44x44 km (SMOS pixel).

To derive the level 2 (L2) soil moisture product, brightness temperatures T_B as acquired by SMOS (proportional to the measured radiation) are modeled for both polarizations at each incidence angle by means of the L-band Microwave Emission of the Biosphere (L-MEB) forward model (*Wigneron et al.*, 2007). An initial soil moisture guess and auxiliary parameters (e.g. soil properties, land cover information, leaf area index, topography, temperature and other climate parameters) are required as input. The soil moisture and temperature initial guesses presented in Section 6.5.3 both originate from the European Centre for Medium-range Weather Forecasting (ECMWF) product spatially and temporally aggregated over the working area (both contained in the L2 product). Modeled and measured T_Bs are compared, and by minimizing a cost function, soil moisture is iteratively retrieved for each node of a fixed earth surface grid (Discrete Global Grid DGG) with uniform spacing (∼15 km). Fig. 6.1 illustrates the locations of the DGG nodes in the Skjern River Catchment, including the working area and corresponding SMOS pixel around one grid node.

L-MEB is based on the relationship between T_B, physical temperature and the land surface emissivity/reflectivity, which in turn is related to the soil's dielectric constant after segregating atmosphere, vegetation and surface roughness contributions using the multi-angular and dual-polarized information. Taking advantage of the large contrast between

the dielectric properties of water and solid soil particles at L-band, soil moisture is linked to the dielectric constant via the Dobson dielectric mixing model (*Dobson et al.*, 1985; *Peplinski et al.*, 1995).

L-MEB is built for uniform scenes with certain model characteristics and calibration parameters. However, the above-mentioned auxiliary input parameters are mostly heterogeneous at significantly smaller spatial scales than SMOS pixels. To account for this, the retrieval algorithm aggregates the estimated contributions from several elementary land cover classes derived from ECOCLIMAP (*Masson et al.*, 2003). This data set is previously grouped into eight generic classes (bare soil and low vegetation covers, forests, open water, barren rocks, frozen soils, snow covered areas, ice, and urban areas) and interpolated on a 4x4 km reference grid (Discrete Flexible Fine Grid, DFFG) centered on each DGG node. Within the working area radiometric fractions of each generic land cover class are estimated by means of the antenna weighting function. For the class with the highest radiometric fraction soil moisture is retrieved using the respective elementary model as well as auxiliary input (provided at the DFFG scale), while the other classes contribute with fixed default values.

6.4. Methodology

6.4.1. Network design

Selection of SMOS pixel

Two criteria were taken into account when selecting the SMOS pixel to be validated: (1) The spatial overlap between the SMOS pixel and the Skjern River Catchment including the HOBE study sites should be maximized, and (2) the open water fraction within the working area affiliated with the SMOS pixel should be minimized. The latter is of importance as water bodies exhibit very different brightness temperatures than those observed over land, which can significantly impact the soil moisture retrieval result. Eligible SMOS nodes are shown in Fig. 6.1. Corresponding radiometric open water fractions contained in the respective working areas of DGG nodes 2001515, 2001516, 2001517, 2002028, 2002029 and 2002030 are 1.85, 0.51, 0.29, 0.25, 0.24 and 0.56%, respectively. While all these amounts are very small, the SMOS pixel around node 2002029 provides the best coverage of the catchment including the HOBE study sites and was thus chosen for validation.

Selection of network clusters

To minimize maintenance costs the network was designed by dividing the 30 monitoring stations into three clusters with diameters of up to ∼10 km (Fig. 6.2). One cluster was centered on the SMOS grid node as this represents the area from which the highest radiation fractions originate. A second cluster was allocated to the north-east of the SMOS pixel, around the HOBE agriculture site Voulund with one network station at the study site to render the data connectable to other geophysical measurements. For the same reason one network station was assigned to the HOBE forest site Gludsted, situated some kilometers east of this cluster. The third cluster was placed in the south-west to account for the small spatial gradient observed in the mean annual precipitation for the period 1990 to 2005 (10x10 km grid, *Scharling*, 1999) from south-west (∼900 mm/yr) to north-east (∼800 mm/yr).

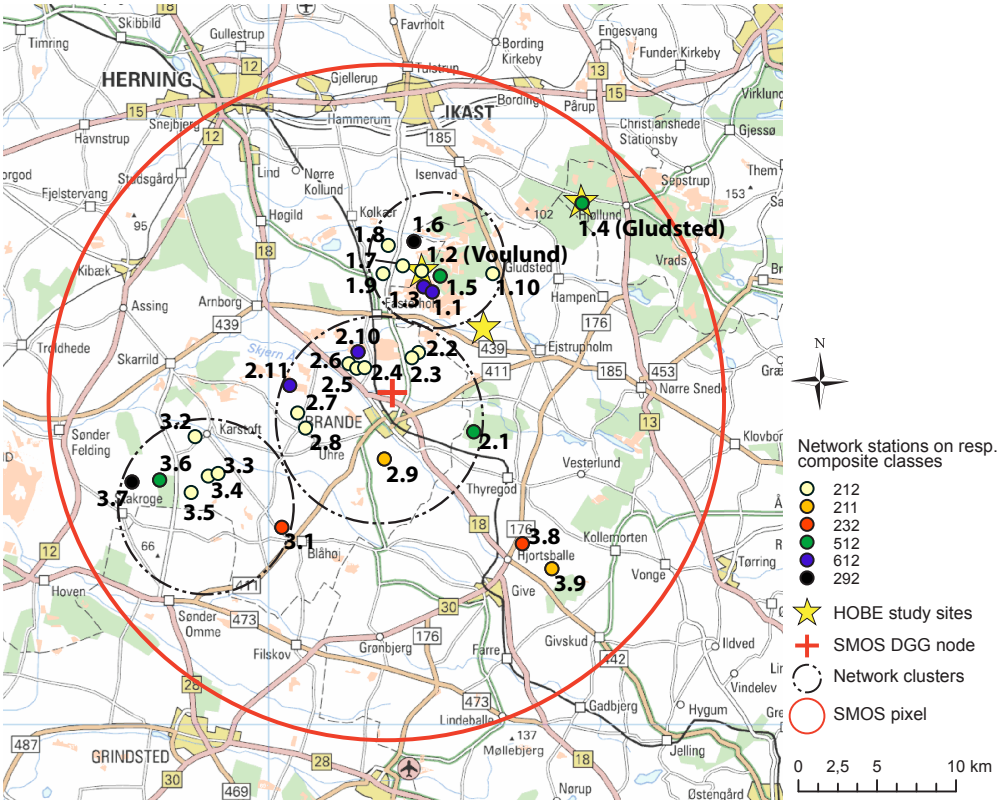

Figure 6.2.: Overview of the 30 soil moisture network stations installed in the Skjern River Catchment, Western Denmark, within three clusters in the selected SMOS pixel around Discrete Global Grid node 2002029.

Selection of theoretical station locations

For positioning the station locations within these cluster areas, a Geographic Information System (GIS) analysis was performed, thus determining the most representative combinations of environmental conditions (topography, land cover and soil type) within the SMOS pixel. Elevations span from 0 m at the western coastline to around 180 m a.s.l. in the eastern part of the Skjern River Catchment with 99.8 and 98.5% of the derived slopes $< 5°$ for the SMOS pixel and working area of DGG 2002029, respectively (90 m digital elevation model of the Shuttle Radar Topographic Mission, *Jarvis et al.*, 2008). No SMOS topography flags are set for node 2002029. Consequently, topographical effects were neglected in the successive analysis.

Table 6.1 summarizes soil types with respective grain size distribution and organic matter content of the 0-20 cm topsoil layer (250 m Danish topsoil grid, *Greve et al.*, 2007). Accordingly, Table 6.2 shows the subsoil composition below 30 cm depth (clay versus sand) with corresponding clay contents based on a map from *Bornebusch and Milthers* (1935), *Smed* (1979), *Schou* (1949), and *DGU* (1945). In both tables respective soil type fractions contained in the SMOS pixel and working area around node 2002029 are given. While the pixel comprises almost 80% coarse sand in the topsoil and 89% sand in the subsoil, these

Table 6.1.: Topsoil information (0-20 cm depth): Soil type, class numbers used in the sum-up to composite classes, textural fractions [%] of clay (< 2 μm), silt (2-20 μm), fine sand (20-200 μm) and total sand (20-2000 μm), organic matter content (humus 58.7% C) [%], and respective fractions [%] of soil type contained in the SMOS pixel and working area around node 2002029.

Soil type	Recl. val.	Clay	Silt	Fine sand	Total sand	Humus	SMOS pixel	Working area
Coarse sand	10	0-5	0-20	0-50	75-100	< 10	79	46
Fine sand	20			50-100			0	3
Coarse loamy sand	30	5-10	0-25	0-40	65-95		13	17
Fine loamy sand	40			40-95			2	13
Coarse sandy loam	50	10-15	0-30	0-40	55-90		0	4
Fine sandy loam	60			40-90			0	9
Clay loam	70	15-25	0-35		40-85		0	2
Humus	90					> 10	6	6

Table 6.2.: Subsoil composition (> 30 cm depth): Soil type, class numbers used in the sum-up to composite classes, clay fractions (< 2 μm) [%] and respective fractions [%] contained in the SMOS pixel and working area around node 2002029.

Soil type	Recl. val.	Clay	SMOS pixel	Working area
Clay	1	> 15	11	30
Sand	2	< 10 (mostly < 5)	89	70

percentages are lowered to 46% and 70% for the entire working area due to a fractional shift towards more loamy soils concurring with the position of the latest glacial ice margin.

Table 6.3 illustrates land cover fractions (CORINE Land Cover 2000 100 m grid, level 2, *EEA*, 2005; *Bossard et al.*, 2000) within the SMOS pixel and working area around node 2002029, respectively. They are comparable for the two spatial scales with agriculture taking the major parts, followed by forest (mainly coniferous) and shrub/grassland (heath). In agreement with the corresponding SMOS radiometric fractions, water bodies only exhibit marginal parts. Land cover exerts strong influence on the SMOS soil moisture algorithm through both choice of the retrieval model and high non-linearity of vegetation parameters. Thus, it is of importance that the area for which the network delivers soil moisture data is representative for the entire working area in terms of land cover, while this is less relevant in case of soil types.

To find the most representative combinations of topsoil, subsoil, and land cover types within the SMOS pixel, the individual data sets were re-sampled and snapped to the land cover 100m-grid (Fig. 6.3a-c). Using the nearest neighbor re-sampling technique merely changed the cell size while all categorical information was conserved. The land cover, top- and subsoil data sets were reclassified to values of 100s, 10s and 1 digits ('reclass values' in Tables 6.1-6.3), and summed up to one grid containing all possible combinations of the original layers (referred to 'composite class map' hereafter, Fig. 6.3d). Fig. 6.4 displays the composite class fractions revealing five classes (212, 232, 412, 512 and 612) with individual shares of > 5%. Together they constitute approximately 75% of the SMOS pixel and all have a tendency towards very sandy soils. Including the most frequent classes with humus in the topsoil (292) and clay in the subsoil (211), ∼82% of the prevailing environmental conditions in the validation area are incorporated, which is regarded as a good overall representation. As CORINE land cover class 400 (heterogeneous agriculture) contains all prevailing land

Table 6.3.: Land cover information: land cover type, class numbers used in the sum-up to composite classes, and respective fractions [%] contained in the SMOS pixel and working area around node 2002029.

Land cover descr		Recl. val.	SMOS pixel	Working area
Artificial surfaces	Urban	100	2	3
	Industry, transport		1	1
	Artificial vegetation		0	1
Agricultural areas	Arable land	200	57	63
	Pastures	300	1	1
	Heterogeneous agriculture	400	16	13
Forest and semi natural areas	Coniferous forests	500	14	11
	Shrub and grassland	600	7	5
Wetlands	Inland wetlands	700	2	1
Water bodies	Inland waters	800	0	1

Table 6.4.: Selected composite classes for the SMOS pixel around node 2002029: Class number, land cover, top- and subsoil descriptions, respective class fractions [%], corresponding recalculated fractions after redistribution of class 412 and omitting all other classes [%], and numbers of allocated network stations

Class nr.	Land cover	Topsoil	Subsoil	Fract.	Redist. fract.	Nr. stats.
211	Arable land	Coarse sand	Clay	4.3	5.2	2
212	Arable land	Coarse sand	Sand	39.4	55.3	16
232	Arable land	Coarse loamy sand	Sand	5.5	6.7	2
292	Arable land	Humus	Sand	2.9	3.5	2
412	Heterog. agricult.	Coarse sand	Sand	12.1		
512	Forest	Coarse sand	Sand	12.4	15.1	4
612	Heath/shrubs	Coarse sand	Sand	5.6	14.2	4
Others				17.8		

cover types (arable land intermixed with forest and shrub/grassland, *Bossard et al.*, 2000), the composite class 412 was repartitioned equally to the classes 212 and 612 (same soil type, Table 6.4). The 30 network stations were then distributed among these six classes according to their respective fractions.

Plant structure has an influence on vegetation parameters in the SMOS soil moisture algorithm. Thus, the predominant crop types were estimated based on the field plan 2005 (*FVM*, 2005) as well as areal cultivation statistics 2006 - 2008 (*Danmarks Statistik and Service*, 2009, Table 6.5) for Central Western Denmark. The 22 agricultural network stations were allocated to fields with the three most frequent crops barley, grass and winter wheat, and additionally to maize and potatoes (differing plant structure) according to respective fractions.

6.4.2. Network implementation

Field inspection/final decision on station locations

Provisionally, the stations were distributed among the three network clusters using the composite class map (Fig. 6.3d). Final decisions on the locations were taken after field inspection. Due to an extensive road network, access did not constrain the choice.

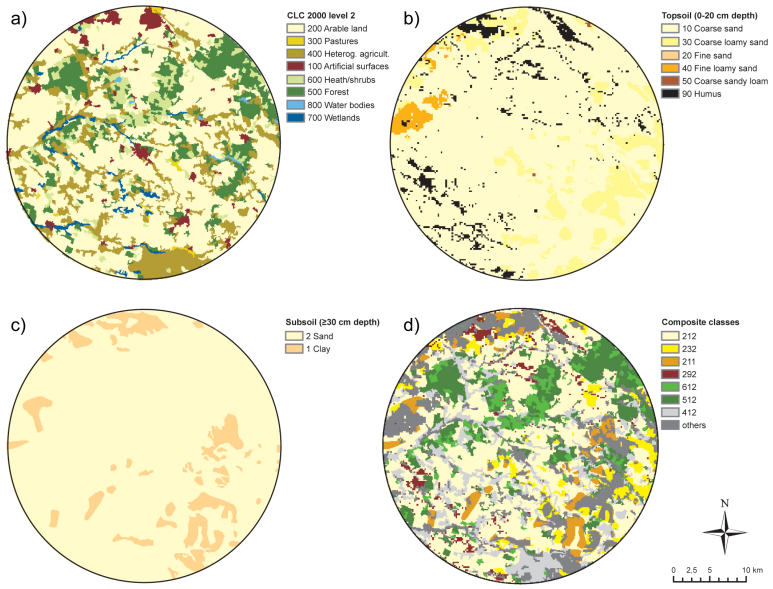

Figure 6.3.: Land cover type (a), topsoil types (b), subsoil types (c) and composite classes, combining land cover type, topsoil and subsoil types (d) within the selected SMOS pixel around SMOS Discrete Global Grid node 2002029.

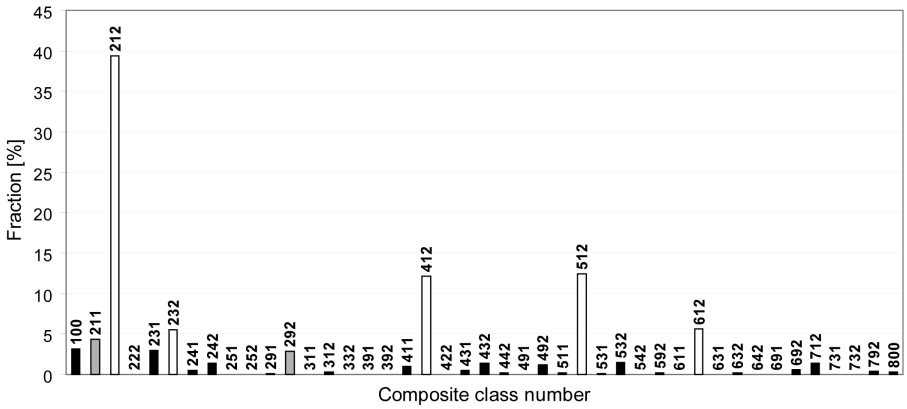

Figure 6.4.: Fractions [%] of the composite classes (combining land cover, topsoil and subsoil data) contained within the SMOS pixel around node 2002029. Classes selected for the placement of network stations with fractions > 5 % (212, 232, 412, 512 and 612) are in white, the most frequent classes with humus in topsoil (292)/clay in subsoil (211) are in grey, and the remaining (not considered) classes are in black.

For forest and heath (composite classes 512 and 612), no reallocation of the pre-selected points was necessary, as theoretically estimated land cover and soil types were in good agreement with actual conditions. Three stations were placed under scotch heather, one under natural grass, and four under spruce plantations characterized by pronounced row

Table 6.5.: Predominant crop types in the Skjern River Catchment, respective estimated fractions [%], number of allocated network stations per crop type and per composite class individually (theoretical and actual distribution).

Crop type	Fractions	Nr. of stations	Nr. stat. 211	Nr. stat. 212	Nr. stat. 232	Nr. stat. 292
Spring barley	28	8	2(1)	2(4)	2(1)	2(1)
Winter barley	7	2	0(0)	2(2)	0(0)	0(0)
Grass	20	5	0(1)	5(3)	0(1)	0(0)
Winter wheat	15	3	0(0)	3(2)	0(0)	0(1)
Maize	5	2	0(0)	2(2)	0(0)	0(0)
Potatoes	4	2	0(0)	2(2)	0(0)	0(0)
Winter rape	4					
Oats	2					
Fallow land	5					
Others	10					

structure, scarce understory and moss carpets. All these locations exhibit distinct organic surface layers.

The estimated occurrence of agricultural areas and crop types was also encountered in reality, and in case of the composite class 212 the expected very sandy top- and subsoils were clearly perceived at the preselected locations. However, the distinction between classes 212 and 292 (sand and humus in the topsoil, respectively) was almost impossible, as the upper soil layer exhibited a very dark color at all investigated locations, due to intermixed organic matter as a result of agricultural practices. Likewise, for locations where classes with higher clay fractions were indicated on the composite class map (i.e. class 211 with clay in the subsoil or class 232 with loamy sand in the top soil) we could solely notice that soils clearly exhibited greater clay contents than the sandy classes. In situ discrimination between class 211 and 232 turned out to be difficult. Furthermore, at locations where an increased clay fraction was noticed, it persisted usually throughout the entire depth profile. As classes 211, 232 and 292 only account for a small fraction of the entire SMOS pixel (∼13%), these inaccuracies were accepted when placing the corresponding stations. We resigned the labor-intensive determination of texture and organic amounts for the localization of spots with the exact soil properties inherent in the respective composite classes. Two of the four more clayey stations were placed outside of the third cluster in the south-east to account for the region where the main fraction of more clayey soil conditions within the SMOS pixel occurs as a result of the geomorphological evolution in the area (see 6.2).

The estimated number of stations per crop type could be maintained, even though some adjustments had to be made between the composite classes (Table 6.5). This was accepted since crop rotations change throughout the years. An overview of the final network locations is given in Fig. 6.2 and Table 6.6.

Installation

Sensor installation took place in fall 2009. At each station, three 5TE sensors were placed at respective depths of 2.5, 22.5 and 52.5 cm (corresponding to measurement intervals of ∼0-5, 20-25 and 50-55 cm) from the soil surface after removal of the litter/organic layer

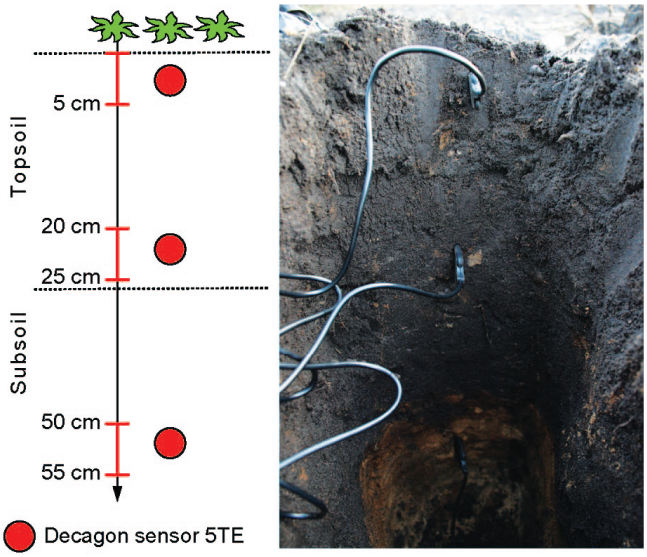

Figure 6.5.: Schematic sensor configuration at individual network stations (left) using three Decagon 5TE sensors integrating soil moisture over ∼5 cm depth intervals, respectively, and photo of soil profile with sensors installed according to the theoretical scheme (right).

(Fig. 6.5). The sensors were horizontally inserted with the blade in the vertical position to avoid ponding.

While for SMOS validation the 0-5 cm data is of most importance, the profile measurements suit the needs of hydrological modeling activities in the HOBE project, possibly in combination with assimilated SMOS data. With respect to heath and forest stations, one 5TE sensor was additionally installed in the organic layer in summer 2010. This is crucial as the signal measured by SMOS over these areas most probably originates exclusively from this moist layer (*Bircher et al.*, 2010).

Sensor readings are logged in 30 minute intervals. Stations placed in crops have to be temporarily removed during cultivation practices (seed/plantation and harvest) - twice for summer crops (spring and fall) and once for winter crops (late summer).

Soil samples were taken at each sensor depth during installation. Sand (2000-20 μm), silt (20-2 μm) and clay (< 2 μm) fractions (International Society of Soil Science, ISSS, 1929) of the 0-5 cm depth were determined for all network locations using sedimentation and sieve analysis, and soil bulk density was calculated (Table 6.6). Additionally, soil samples were collected from 0-5 cm depth on agricultural land, forest and heath (composite classes 212, 512 and 612, resp.) during an airborne campaign (*Bircher et al.*, Accepted). These samples were used for calibration checks over the entire wetness range in the laboratory.

6.4.3. Network data analysis

To check the feasibility of our approach as well as the reliability of the network data, several analyses were conducted:

The sensor output - sample water content couples from the lab calibration were compared to the Decagon 5TE default calibration curve (*Topp et al.*, 1980). By means of the texture

Table 6.6.: Overview of the 30 network stations: Station number, latitude, longitude, composite class number, total sand, fine sand, silt, and clay fractions at 0-5 cm depth [%], bulk density (BD) at 0-5 cm depth [g/m^3], land cover, and vegetation 2009/10 and 2010/11, respectively.

Station Nr.	Lat	Lon	Class Nr.	Sand total	Fine sand	Silt	Clay	BD	Land cover	Vegetation 09/10	Vegetation 10/11
log1.01	56.02	9.18	612	94.3	18.9	3.5	1.2	1.29	Heath	Grass	Grass
log1.02	56.04	9.16	212	91.7	21.4	5.4	2.3	1.32	Agriculture	Grass/barley	Grass/barley
log1.03	56.03	9.17	612	91.5	11.1	2.4	4.1	1.43	Heath	Scotch heather	Scotch heather
log1.04	56.07	9.33	512	87.3	7.0	4.2	3.0	1.04	Forest	Spruce	Spruce
log1.05	56.03	9.19	512	82.5	15.3	4.4	3.6	1.02	Forest	Spruce	Spruce
log1.06	56.05	9.16	292	90.0	16.1	4.6	2.8	1.20	Agriculture	Spring barley	Potato
log1.07	56.04	9.14	212	90.0	20.3	5.4	3.5	1.31	Agriculture	Grass	Grass
log1.08	56.05	9.12	212	82.2	8.9	5.3	3.3	1.21	Agriculture	Potato	Winter barley
log1.09	56.04	9.13	212	89.5	13.3	4.6	3.2	1.30	Agriculture	Winter barley	Spring barley
log1.10	56.03	9.24	212	93.2	14.6	3.6	2.7	1.19	Agriculture	Maize	Maize
log2.01	55.94	9.22	512	95.8	9.3	1.8	1.3	1.33	Forest	Spruce	Spruce
log2.02	55.98	9.16	212	90.5	8.9	4.0	2.4	1.04	Agriculture	Grass	Grass
log2.03	55.98	9.15	212	86.7	7.9	3.6	1.0	1.28	Agriculture	Potato	Spring barley
log2.04	55.98	9.1	212	87.3	20.9	4.9	7.1	1.21	Agriculture	Potato	Spring barley
log2.05	55.98	9.1	212	87.3	22.6	7.3	4.9	1.22	Agriculture	Spring barley	Potato
log2.06	55.98	9.09	212	93.7	27.7	2.7	3.2	1.41	Agriculture	Grass	Grass
log2.07	55.95	9.03	212	74.9	20.8	7.5	4.6	1.26	Agriculture	Maize	(Winter) Rye
log2.08	55.94	9.03	212	86.3	52.1	7.2	6.4	1.04	Agriculture	Winter wheat	Spring barley
log2.09	55.93	9.12	232	51.1	27.1	28.3	20.6	0.78	Agriculture	Grass	Grass
log2.10	55.99	9.09	612	85.4	5.4	3.5	2.5	1.33	Heath	Scotch heather	Scotch heather
log2.11	55.97	9.02	612	95.7	11.1	2.0	1.7	1.35	Heath	Scotch heather	Scotch heather
log3.01	55.88	9.01	211	79.0	26.2	8.7	5.7	1.30	Agriculture	Spring barley	Potato
log3.02	55.94	8.92	212	90.9	9.4	5.8	3.1	1.31	Agriculture	Spring barley	Spring barley
log3.03	55.91	8.95	212	88.2	23.5	4.3	4.8	1.09	Agriculture	Spring barley	Grass
log3.04	55.91	8.94	212	91.0	39.0	3.2	3.7	1.07	Agriculture	Winter barley	Winter barley
log3.05	55.9	8.92	212	95.0	21.2	3.1	1.6	1.35	Agriculture	Winter wheat	Spring barley
log3.06	55.91	8.88	512	88.9	14.2	5.0	4.8	1.16	Forest	Spruce	Spruce
log3.07	55.91	8.85	292	92.1	15.7	3.8	4.0	0.99	Agriculture	Winter wheat	Spring barley
log3.08	55.88	9.27	211	65.6	36.2	21.0	13.3	1.51	Agriculture	Grass	Grass
log3.09	55.86	9.29	232	85.1	42.9	5.7	5.2	1.26	Agriculture	Spring barley	Grass

data the actual soil type distribution among the network stations was compared with the one based on the composite class map. Per station the measured soil moisture and temperature data of all depths for the year 2010 was checked for the expected behavior as a function of land cover and soil types.

Further network data analyses focused on the 0-5 cm depth only:

(1) The soil moisture data of five selected agricultural stations (2.09, 3.08, 3.01, 1.09, and 3.05, Fig. 6.2/Table 6.6) with vegetation types of comparable plant structure but decreasing clay (21-2%)/increasing sand (51-95%) fractions was compared with the 30 station network average in order to study the influence of texture for the time period January - August 2010 (to assure continuous data coverage).

(2) To study regional variability and potential influence of the long-term precipitation gradient, soil moisture and temperature of three selected stations of similar texture and land cover in the north-east (1.02, 1.06, 1.09) and south-west part (3.02, 3.04, 3.07) of the SMOS pixel as well as precipitation data of the two closest 10 km grid nodes, respectively, were averaged and compared over the year 2010.

(3) Soil moisture and temperature averaged over all 30 network stations were compared with SMOS L2 soil moisture (initial guess and retrieved) and temperature (initial guess) data for the year 2010. Furthermore, to avoid deviations that may arise from the applied petrophysical relationship (*Topp et al.*, 1980), this comparison was also conducted at the dielectric constant level. The 5TE sensor output was transformed to the real part of the dielectric constant by both the Decagon conversion (output/50) as well as an empirical relationship (real dielectr.=0.0234*output-1.2917, *Rosenbaum et al.*, 2010), and averaged over all 30 network stations. With respect to SMOS, the real part of the dielectric constant from the L2 product (retrieved with a non cardioid model, *Bengoa et al.*, 2010) computed

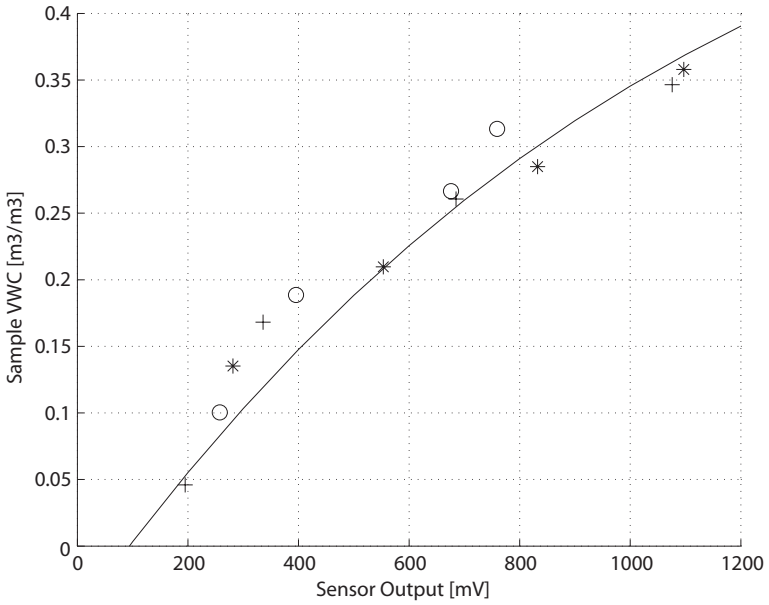

Figure 6.6.: 5TE sensor output [mV] against volumetric moisture content $[m^3/m^3]$ derived from surface soil samples (0-5 cm depth) of agricultural land (o), forest (+) and heath (∗) (composite classes 212, 512 and 612, respectively) including the Decagon 5TE default calibration curve.

from the retrieved soil moisture data by means of the Dobson dielectric mixing model was used.

6.5. Results and discussion

6.5.1. Calibration and soil texture checks (0-5 cm)

Fig. 6.6 shows the 5TE sensor output compared to the volumetric moisture content derived from 0-5 cm soil samples collected on agricultural land, forest and heath (composite classes 212, 512 and 612, resp.) as well as the Decagon 5TE default calibration curve. Corresponding Root Mean Square Error (RMSE) values are 0.030, 0.026 and 0.022. Thus, for all three classes RMSEs are within the declared sensor accuracy (0.030).

In Fig. 6.7 the 0-5 cm depth texture data (sand-% vs. clay-%) for the network are shown and compared to the composite classes used in the Danish soil grid (*Greve et al.*, 2007). As the organic content was not measured it is not possible to classify the two stations representing class 292. For the remaining 28 stations it can be seen that: (1) all forest and heath stations (classes 512 and 612) are correctly allocated to the soil type sand, while two of the agriculture class 212 (stations 2.04 and 2.08) exhibit slightly higher clay fractions than expected; (2) the agriculture class 211 is expected only to show more clay conditions in the subsoil, but in fact slightly and significantly higher clay fractions in the topsoil are found for stations 3.01 and 3.08, respectively; (3) with respect to agricultural class 232 station 3.09 is correctly classified whereas station 2.09 shows significantly higher clay fractions than expected. Overall, five out of 28 stations are misclassified. However, overall

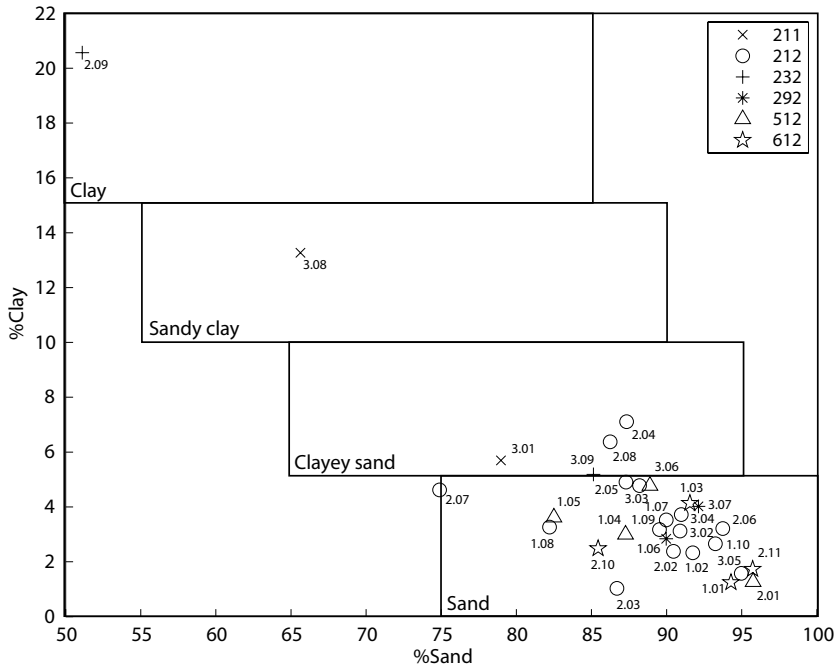

Figure 6.7.: Soil texture data (sand-% vs. clay-% of 0-5 cm depth) per network station according to the composite classes. Discrimination of zones corresponding to the Danish soil grid (*Greve et al.*, 2007) is also shown.

the predetermined number of stations per soil type (Table 6.4) is more or less maintained in the final network setup.

6.5.2. Profile soil moisture and temperature (all depths)

Fig. 6.8 shows soil and temperature data of all depths acquired during the year 2010 for five selected stations representing the majority of encountered patterns throughout the entire network data set: 2.11 (heath, class 612), 1.04 (forest, class 512), 1.02 (agriculture, class 212, HOBE site Voulund), 2.05 (agriculture, class 212), and 2.09 (agriculture, class 232). Additionally, in case of the heath and forest stations (2.11 and 1.04) data from the sensors installed in the organic layers are depicted. It should be noted that for the organic material, site-specific calibration will be a crucial issue. Thus, at the point of writing this paper these measurements should only be considered in a relative term.

Typically, for all network locations in agricultural fields and with coarse sand in the topsoil, a homogeneous mixture of loose sand and organic material is found in the plow layer with a pronounced hardpan just below (∼30-45 cm depth), and with sand appearing at around ∼35-50 cm depth. Litter is absent or scarce, never covering the surface as a whole. In most cases the 0-5 cm and 20-25 cm sensors were installed in the plow layer. As water infiltrates quickly through the sandy material and the water content in the surface layer is reduced by evapotranspiration, the 0-5 cm sensors generally show drier conditions than the 20-25 cm sensors located just above the hardpan, which restricts the further downward movement of water. Moreover, the 50-55 cm sensors measure high water contents if located

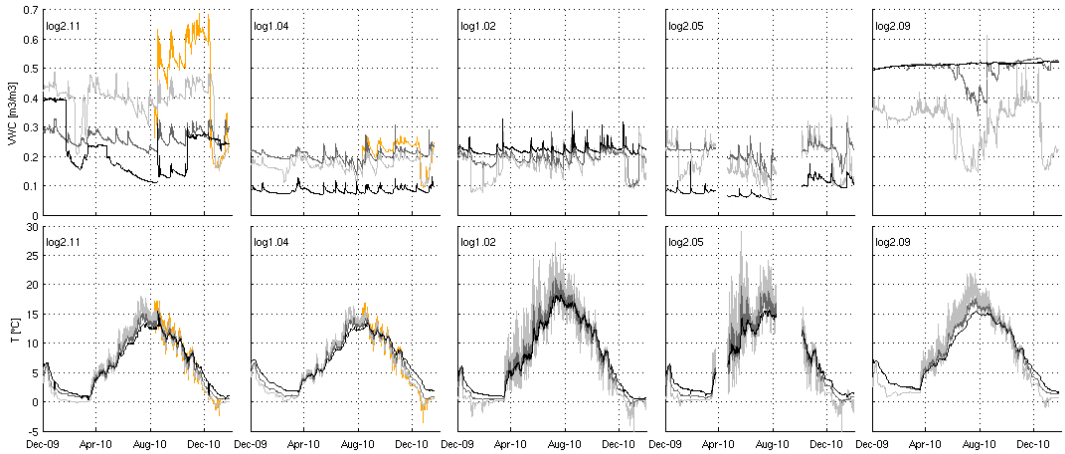

Figure 6.8.: Profiles of soil moisture (top row) and temperature (bottom row) for the year 2010: for stations 2.11 (heath, class 612), 1.04 (forest, class 512), 1.02 (agriculture, class 212, HOBE site Voulund), 2.05 (agriculture, class 212), and 2.09 (agriculture, class 232); organic layer (orange), mineral soil: 0-5 cm (light grey), 20-25 cm (dark grey), and 50-55 cm (black) depths.

close to the upper hardpan boundary (station 1.02) and show much drier conditions when installed within or below the hardpan (station 2.05).

In contrast, a pronounced litter layer of moss/organic material exists (∼5-20 cm) for the sandy soils under natural vegetation. Due to absence of plowing, the topsoil down to the hard pan is leached and quartz-rich as expected for a typical podsol, and the hardpan starts at around 20-25 cm depth. While all four forest stations show similar soil moisture patterns throughout time, the conditions at the four heath stations are very variable. Station 2.11, for instance, is situated in a very wet area where standing water was observable around the station during installation. The 0-5 cm sensor at this station shows high moisture values as it is nourished by the very moist moss/organic layer on top. At the time of installation the 50-55 cm sensor was mounted below the water table. However, when the water table later during the season was lower the effect of the dry sand below the hardpan became evident in the data from the 50-55 cm sensor. In comparison, the sensors in the moss/organic layer as well as the 0-5 cm mineral layer of the forest station 1.04 show much drier conditions. This can be attributed to their placement on a small hill. The 20-25 cm sensors of both stations 2.11 and 1.4 were installed at the upper hardpan boundary and show similar behavior. Generally, the pattern of the forest stations is more related to the one met at agriculture sites where the 50-55 cm sensor is located in the dry sand below the hardpan (station 2.05).

At station 2.09 the sensors were installed in clayey material with much higher water holding capacity throughout the entire depth profile, and with a firm hardpan at 20-25 cm depth. During installation the water table was at 20 cm depth. Later during the summer the soil at the 20-25 cm sensor location became drier while the 50-55 cm sensor remained below the water table.

The different values for porosity of sandy and clayey soils are well-reflected in the measurements of the 50-55 cm sensors situated below the water table with saturated moisture contents of ∼0.4 and 0.5 in case of the sandy station 2.11 and the clayey station 2.9, re-

spectively. Even higher values are found in the organic material. Furthermore, the effect of texture is also reflected in the seasonal variation of soil moisture for the different soil types. Sandy soils have a smaller water holding capacity compared to clayey and organic materials and as a result the seasonal variation is relatively small. Apart from the drop of moisture content in the organic and 0-5 cm mineral layers during freezing in the winter months this behavior is evident for the two sandy agricultural stations (1.02 and 2.05) as well as for the forest station (1.04). In contrast, the clayey agricultural station (2.09) and the heath station (2.11) show a much higher seasonal variability. Irrigation has obviously a distinct imprint as seen for the agricultural stations 1.02 and 2.05, and in case of the forest site, tree interception must exert a balancing effect.

At all sites the temperature profiles show the expected diurnal and seasonal patterns, as well as a slight time lag and amplitude decrease with increasing depth. Furthermore, the presence of vegetation and moss/organic layers (heath and forest stations) insulating the mineral soil becomes apparent. The isolation effect is reflected in both the diurnal and seasonal temperature amplitudes and is most pronounced for the forest station.

All in all the observed moisture and temperature patterns are clearly related to land cover and soil conditions. Soil moisture seems to be mostly affected by soil characteristics while soil temperature is mostly dependent on land cover.

6.5.3. Surface soil moisture and temperature (0-5 cm)

Texture comparison

Fig. 6.9 illustrates the 0-5 cm soil moisture measurements of the agricultural stations 2.09, 3.08, 3.01, 1.09 and 3.05 with similar vegetation and decreasing clay/increasing sand fractions (Table 6.6), respectively, in comparison with the 0-5 cm average over all 30 stations between January and August 2010. The mean of daily precipitation of the 10 km grid nodes contained within the SMOS pixel (Fig. 6.1) is also plotted.

Over the major part of the chosen time span, increasing clay content complies with higher moisture content, resulting in significant overrepresentation with respect to the overall network average, and vice versa in the case of high sand contents. Thus, the influence of soil texture is clearly demonstrated and also reflected in the biases (average residuals from expected value) ranging from 0.146 for the clay station 2.09 to -0.057 for station 3.05 with highest sand fractions. The larger absolute bias (relative to other stations) of the clay station is reasonable, as the 30 station average contains a much larger fraction of sandy sites. The moisture pattern also follows the precipitation trend well, and in March, snow melt is observable throughout all stations.

Regional comparison

Fig. 6.10 shows average and standard deviation (shaded region) of the 0-5 cm soil moisture and temperature of three selected stations of similar texture and land cover in the north-east (1.02, 106, 1.09) and south-west part (3.02, 3.04, 3.07) of the SMOS pixel, as well as 24h precipitation accumulations of the two closest 10 km grid nodes, respectively, for the year 2010.

Regional differences are most pronounced for soil moisture and least for temperature. However, in any case they are small with low RMSE/biases (0.034/0.010, 0.86/0.11 °C and

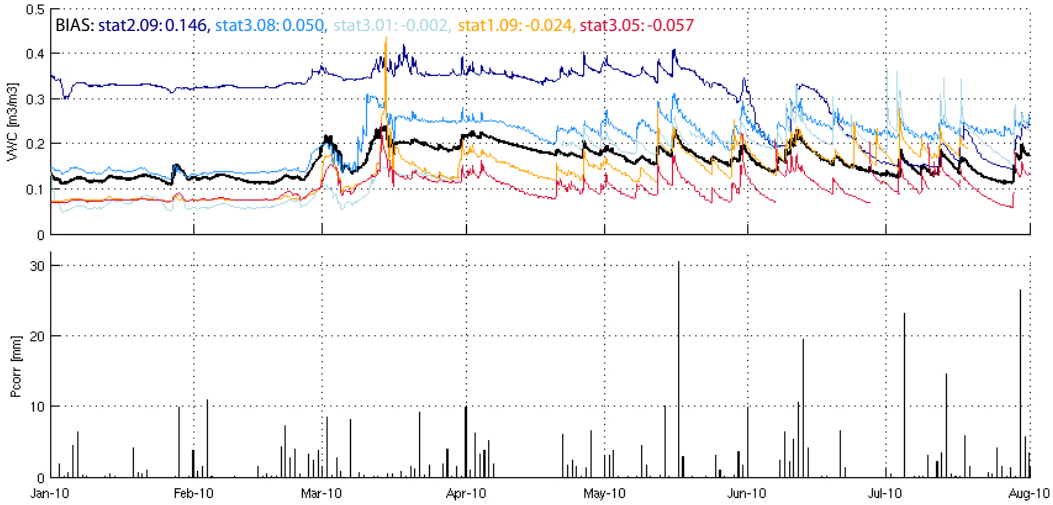

Figure 6.9.: Surface soil moisture (0-5 cm) with decreasing/increasing clay/sand fractions, respectively, between January and August 2010: agricultural stations 2.09 (dark blue), 3.08 (blue), 3.01 (light blue), 1.09 (orange) and 3.05 (red) compared to the average of all 30 network stations (black) (top row) including corresponding biases; and mean of daily precipitation of the DMI 10 km grid nodes contained within the SMOS pixel (bottom row).

3.72/-0.39 mm for soil moisture, temperature and precipitation, respectively), with considerable correlations reflected in corresponding R^2 values of 0.57, 0.99 and 0.86. Moreover, with temporal mean standard deviations of 0.024 and 0.041 (soil moisture) and 0.37 and 0.5 °C (temperature) for the north-eastern and south-western stations, respectively, the variability between the two areas is in the same order as within them.

SMOS L2 comparison

Fig. 6.11 displays 0-5 cm average network and SMOS soil moisture and temperature data (L2 product) for the year 2010, as well as the corresponding mean of daily precipitation of the DMI 10 km grid nodes contained within the SMOS pixel (Fig. 6.1).

Also network soil moisture spatial variability (standard deviation, blue-shaded region) and in situ sensor accuracy are shown (grey-shaded region). For SMOS retrieved values including the associated Data Quality indeX (DQX) reflecting the retrieval error induced by the model (red-shaded region) as well as the initial guess are shown. Mean network soil moisture fluctuates around a temporal average of 0.176 and with a standard deviation of 0.041. The spatial variability between the individual stations is larger with a temporal average of 0.070, which is in the same order as found by *Famiglietti et al.* (2008) for a site in the United States at the same spatial scale. Network and SMOS soil moisture follow the precipitation dynamics well. Correlations (R^2) between network and SMOS retrieved and initial guess soil moisture respectively are 0.49 and 0.67. However, remarkable offsets are visible. While the SMOS soil moisture initial guess approximately corresponds to the upper boundary of the network variability region, the retrieved data follows more or less its lower boundary, or even below (bias values of 0.057/-0.092 for initial/retrieved

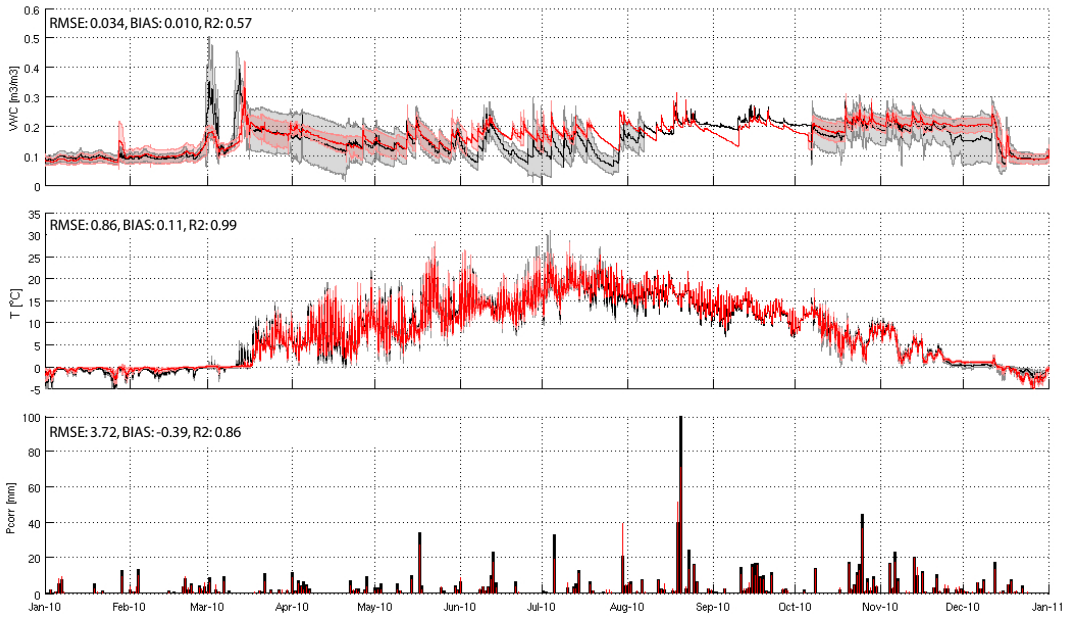

Figure 6.10.: Regional surface soil moisture and temperature (0-5 cm) for the year 2010: Average and standard deviation (shaded regions) of the 0-5 cm soil moisture (top row) and temperature (center row) of three selected stations of similar texture and land cover in the north-east (1.02, 106, 1.09, red) and south-west part (3.02, 3.04, 3.07, black) of SMOS pixel 2002029 as well as daily precipitation of the two closest 10 km grid nodes, resp., (bottom row) including corresponding RMSE, bias and R^2 values. During periods where the shaded regions are absent, only one sensor was operational per area.

SMOS soil moisture compared to the network average, respectively). Furthermore, SMOS soil moisture shows higher amplitude compared to the network data. These findings are consistent with results from various validation sites across continents: Australia (*Rüdiger et al.*, 2011b), Germany (*Dall'Amico et al.*, Accepted), USA (*Jackson et al.*, Accepted; *Al Bitar et al.*, Accepted; *Leroux et al.*, Submitted) report positive biases in the order of 0.05-0.15 and negative biases around 0.02-0.2 for SMOS initial and retrieved soil moisture, respectively. The temporal trends encountered at the individual sites are followed by the retrieved SMOS soil moisture (R^2 ~0.4-0.62), and tendencies of the latter to overestimate the dynamics (larger amplitudes) have also been noted. Only in Africa constant soil moisture overestimation by SMOS was found (*Gruhier et al.*, Submitted).

In case of temperature, the average of the 30 network stations and the SMOS initial guess surface temperature are in good agreement with corresponding RMSE, bias and R^2 values of 1.1 °C, -0.2 °C and 0.97, respectively. Thus, no significant error seems to be introduced from this parameter.

The comparison of the real dielectric constant averaged from the network and for SMOS over the year 2010 reveal RMSE, bias and R^2 values of 3.95/4.30, 2.30/3.33 and 0.49/0.49 for the Decagon/Rosenbaum et al. sensor output-dielectric constant relations, respectively. Consequently there is no distinct difference between the two dielectric models with R^2s equal to that for the soil moisture comparison. As the SMOS dielectric constant is computed from retrieved soil moisture by means of the Dobson model, this implies that at both comparison

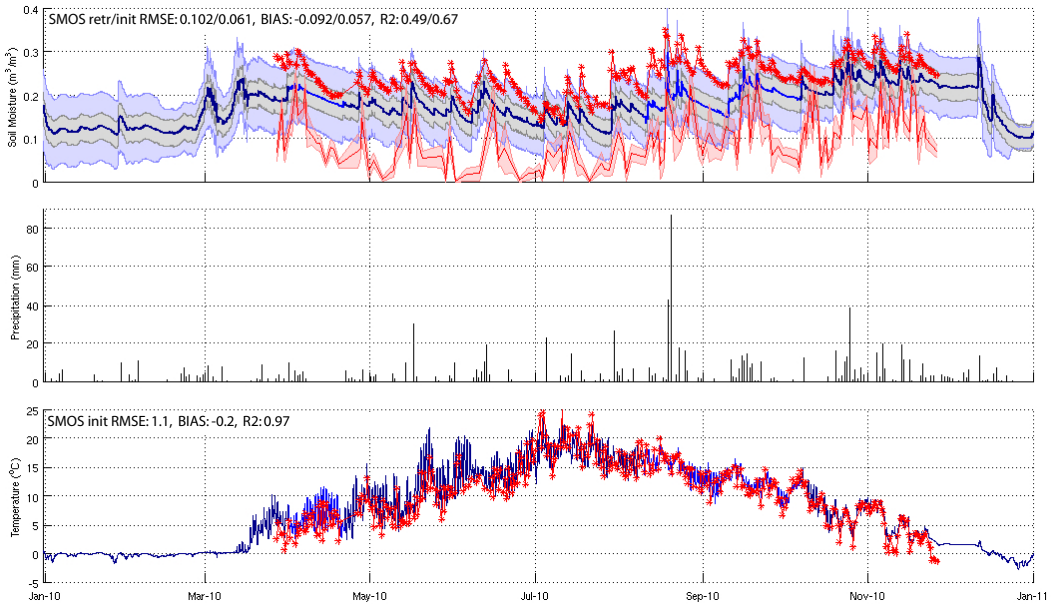

Figure 6.11.: Surface soil moisture and temperature (0-5 cm) comparison between network and SMOS for the year 2010: Surface soil moisture network average and standard deviation (blue lines* and shaded region) including sensor accuracy (grey-shaded region), and retrieved SMOS soil moisture (red line) including the associated retrieval error estimate (DQX, red-shaded region) and corresponding initial guess (red stars, top row); mean of daily precipitation of the DMI 10 km grid nodes contained within the SMOS pixel (center row); temperature network average (blue lines*) and SMOS initial guess (red stars, bottom row). RMSE, bias and R^2 of the in situ versus retrieved/initial SMOS data for soil moisture and temperature are indicated. *dark blue where > 20, royal blue where < 20 stations operational.

levels the uncertainty is consistent and remains on either the network or the SMOS data side.

Based on the results of the presented network data analyses together with the fact that our findings from the comparison with SMOS data are well in range with worldwide validation results, we consider the network to operate according to expectations and to be well-suited for SMOS validation. The discrepancies between network and retrieved SMOS soil moisture data need to be more closely investigated. Currently, numerous explanations are under discussion: (1) a mismatch between sampling depth of conventional soil moisture sensors (∼5-7 cm) and the depth contributing to L-band soil emission ($<$ 5 cm, *Escorihuela et al.*, 2010), (2) scale effects due to the large disparity in spatial scale between the SMOS and in situ measurements, (3) inaccuracies in the SMOS retrieval algorithm and related input, (4) inacurracies in the in situ measurements, and (5) RFI contamination. It is likely, that the observed deviations result from a combination of these factors with variable contributions depending on a validation site's environmental conditions as well as the chosen measurement setup. At the Danish validation site, for example, we believe to reduce the probability of scaling effects by means of the carefully chosen network setup. Meanwhile, we see RFI contamination and inaccuracies in the SMOS retrieval algorithm as probable causes for the bias. Currently, the replacement of the Dobson dielectric mixing model with the one of

Mironov (*Mironov et al.*, 2004) is for example under investigation. *Bircher et al.* (Accepted) showed that Mironov performed better at the Danish validation site to bring brightness temperatures modeled from in situ soil moisture data in agreement with airborne brightness temperature measurements at the 2x2 km scale. Thus, it is also likely that the deviances between SMOS and in situ soil moisture could be lowered by using Mironov in the SMOS retrieval algorithm. With respect to the high amplitudes in the retrieved SMOS data, there is generally consensus that they are likely to be attributed to the mismatch in sampling depth. Generally, the very top layer shows a rapid soil moisture increase immediately following rain events, succeeded by a fast decrease as a result of evaporation and infiltration processes. At deeper depths this response is delayed and somewhat less. The wetter and the more sandy the soils, the more pronounced this effect is. However, at this point, this remains a hypothesis. Further investigations are needed to separate the respective contributions to the deviations between in situ data and SMOS and thus clarify these issues.

6.6. Conclusions

A soil moisture and temperature network with 30 stations (sensors at 0-5, 20-25 and 50-55 cm depths plus in the organic layer in the case of heath/forest locations) has been established within one SMOS pixel (44x44 km) in the Skjern River Catchment, Western Denmark

The design of the network included the following phases: (1) the selection of SMOS pixel 2002029 with minimal water fraction and maximal catchment coverage, (2) the arrangement of three network clusters along a long-term precipitation gradient centered at the SMOS node, and (3) the distribution of the stations according to respective fractions of six classes combining 82% of the prevailing land cover, top- and subsoil conditions. In case of agriculture, additionally crop type frequency was considered. Using this method, it was possible to obtain a representative large-scale in situ soil moisture average for comparison with SMOS data.

Analysis of the collected network data during the year 2010 showed that soil moisture generally follows the precipitation trend. Furthermore, soil moisture and temperature patterns were relatable to the respective land cover and soil conditions. The high soil moisture variability throughout the stations seems to be a strong function of texture/structure while to a less extent influenced by land cover. At the same time the variability in soil temperature is less pronounced and merely a function of the latter. Regional differences in 0-5 cm soil moisture, temperature and precipitation between the north-east and south-west turned out to be small.

A first comparison between 0-5 cm network averages and the SMOS L2 product showed comparable trends with R^2 of 0.49/ 0.67 and 0.97 for SMOS retrieved/initial soil moisture and initial temperature, respectively. The two former indicate significant under-/overrepresentation of the network data (biases of -0.092/0.057 m^3/m^3) as well as faster and stronger wetting/dry-downs (larger amplitudes). Correlation with precipitation is traceable in both, network and SMOS soil moisture data. Average network and SMOS soil temperatures are in good agreement with a bias of -0.2 °C. Thus, this parameter should not introduce errors in the soil moisture retrieval process.

Based on these findings together with the fact that our SMOS data comparison is well in range with worldwide validation results, we consider the network to operate according

to expectations and to be suitable for SMOS validation. Extensive validation activities are currently ongoing at the Danish validation site. It is likely that the discrepancies between network and SMOS soil moisture result from a combination of several factors. The investigation of these potential error sources and their respective contributions is subject of subsequent studies. Furthermore, the influence of the organic layers under natural vegetation is planned to be addressed.

Acknowledgments The project was funded by the Villum Foundation and the Technical University of Denmark. Special thank goes to Yann Kerr and his team at CESBIO, and Jean-Pierre Wigneron for constructive discussions. We also gratefully appreciate various support of the HOBE project members throughout this work.

7. Validation of SMOS L1C and L2 products and important parameters of the retrieval algorithm in the Skjern River Catchment, Western Denmark (Paper 4)

Bircher, S., Skou, N., Kerr, Y. H.

Paper submitted to: IEEE Transactions on Geoscience and Remote Sensing, October 2011

AbstractThe Soil Moisture and Ocean Salinity (SMOS) satellite with a passive L-band radiometer is dedicated to surface soil moisture monitoring. In addition to soil moisture, vegetation optical thickness τ_{NAD} is retrieved (L2 product) from the acquired brightness temperatures (L1C product). The objective of this article is to present the validation work carried out in the Skjern River Catchment, Denmark. L1C/L2 data and the most sensitive parameters in the retrieval algorithm were analyzed by in situ data sets collected within one SMOS pixel (44 km diameter), including network and airborne campaign data. Consistent with worldwide findings, the retrieved soil moisture captures the precipitation dynamics well, but with too large amplitudes and a significant dry bias. The retrieved τ_{NAD} exhibits too high values and day-to-day variability. A filter based on L2 criteria removed RFI affected data and improved the R^2 between retrieved and in situ soil moisture from 0.49 to 0.61, while the bias remained (-0.092/-0.087 m^3/m^3, resp.). Likely error sources for the bias were located as (1) still present RFI, (2) potential link between low soil moisture and high τ_{NAD} and/or low roughness parameter (H_R), (3) $\sim$18/8% lower sand/higher clay fractions and $\sim$0.35 g/cm^3 lower bulk density in SMOS algorithm than in situ, and (4) caveats in the Dobson dielectric mixing model. Substitution with the Mironov model and SMOS processor runs with site-specific input are planned. Differences in sampling depth between SMOS and in situ sensors (held responsible for too large SMOS amplitudes) and the role of organic surface layers will be investigated.

7.1. Introduction

Soil moisture is one of the key variables in the water balance and thus, of high importance in a large range of applications from hydrologic, weather/climate modeling to water resources

management or flood monitoring. Launched in November 2009 the Soil Moisture and Ocean Salinity satellite (SMOS, *Kerr et al.*, 2001, 2010) is the first space mission dedicated to global surface soil moisture (∼0-5 cm depth) monitoring using the technique currently believed to be most effective (*Kerr*, 2007; *Wagner et al.*, 2007). With a passive L-band (1.4 GHz) microwave radiometer on board SMOS has been acquiring data with global coverage every three days at a spatial resolution of ∼44 km. From an initial soil moisture guess and other auxiliary input, soil moisture and vegetation optical thickness (L2 product) are retrieved for each node of a fixed grid (Discrete Global Grid, DGG *Kerr et al.*, 2011) with ∼15 km spacing, using multi-angular and full polarization information. The retrieval is done by a complex algorithm based on the inversion of the L-band Microwave Emission of the Biosphere (L-MEB) radiative transfer model (*Wigneron et al.*, 2007) for an optimized fit with brightness temperatures (T_B) acquired by SMOS (L1C product). At this point, an important step is SMOS Calibration/Validation (Cal/Val) across a range of climatic regions (*Delwart et al.*, 2008), which will steadily improve product quality.

Two complementary approaches have been widely used to attain the required data for SMOS validation: (1) short-term airborne campaigns with intense ground sampling (e.g. *Schmugge et al.*, 1988; *Jackson et al.*, 1995, 1999; *Panciera et al.*, 2008; *Merlin et al.*, 2008; *Peischl et al.*, In Prep.; *Dall'Amico et al.*, 2010; *Kainulainen et al.*, 2010; *Albergel et al.*, 2011; *Kontu et al.*, 2010), and (2) soil moisture networks (e.g. *Bosch et al.*, 2006; *Schaefer et al.*, 2007; *Jackson et al.*, 2010; *Champagne et al.*, 2010; *Walker et al.*, 2001; *Merlin et al.*, 2008; *de Rosnay et al.*, 2009; *Martinez-Fernandez and Ceballos*, 2003; *Calvet et al.*, 2007; *Krauss et al.*, 2010; *Bogena et al.*, 2010). Via the airborne measurements with a footprint of few kilometers the first method offers the advantage of stepwise validation across spatial scales, as well as direct comparison at brightness temperature level. The second method allows long-term monitoring at high temporal resolution. All of these features are relevant for the assessment of a parameter that is highly variable in both space and time and across scales (*Famiglietti et al.*, 1998; *Mohanty et al.*, 2000; *Western et al.*, 2002).

One of the SMOS Cal/Val sites is situated in the Skjern River Catchment, Denmark. The northernmost intensely cultivated area in Europe features latitude-specific environmental conditions such as heathland and very sandy soils with large organic deposits, and is located at short distance to the coast line. With respect to satellite validation it benefits from temporally increased data acquisition at this latitude and pronounced flatness. In the framework of the Danish Hydrological Observatory and Exploratorium (HOBE, *Jensen and Illangasekare*, 2011), the area of ∼44 km diameter around the selected SMOS DGG node 2002029 (refered to 'SMOS pixel' hereafter) was equipped with a soil moisture and temperature network (*Bircher et al.*, Submitted). Additionally, an airborne campaign with the L-band radiometer EMIRAD-2 and concurrent ground measurements was carried out (*Bircher et al.*, 2010, Accepted).

Up to this point, SMOS validation results from several Cal/Val sites including the Danish site report a fairly consistent picture(*Rüdiger et al.*, 2011b; *Dall'Amico et al.*, Accepted; *Jackson et al.*, Accepted; *Al Bitar et al.*, Accepted; *Leroux et al.*, Submitted; *Bircher et al.*, Submitted): SMOS initial/retrieved soil moisture overestimate/underestimate in situ soil moisture with biases in the order of 0.05-0.15 m^3/m^3 and 0.02-0.2 m^3/m^3, respectively. Meanwhile, temporal trends are well reproduced by the retrieved SMOS soil moisture (R ∼0.6-0.8) with a tendency of the latter to overestimate the dynamics (larger amplitudes). Only in West Africa constant overestimation by retrieved SMOS soil moisture was found

(*Gruhier et al.*, Submitted), while low temporal correlation (R mostly <0.5) was solely reported from Southern Germany (*Dall'Amico et al.*, Accepted). Possible explanations for the observed deviations currently under discussion include (1) a mismatch between sampling depth of conventional soil moisture sensors (∼5-7 cm) and the L-band soil emission depth (< 5 cm), (2) effects due to the large disparity in spatial scale between SMOS and in situ measurements (e.g. biased in situ network averages), (3) inaccuracies in the retrieval algorithm and related input, (4) inacurracies in the in situ measurements, and (5) Radio Frequency Interferences (RFI, *Daganzo et al.*, 2010; *Skou et al.*, 2010c). Depending on prevailing environmental conditions and measurement setups, the respective contributions of these potential error sources must be variable for the different Cal/Val sites.

So far, SMOS validation work has focused on SMOS L2 soil moisture and the L1C brightness temperature product (*Kontu et al.*, 2010; *Rüdiger et al.*, 2011b; *Montzka et al.*, Accepted; *Bircher et al.*, Accepted; *Schlenz et al.*, Accepted). However, to investigate uncertainties inherent in the SMOS retrieval algorithm, also the most sensitive input parameters should be checked. In this regard, only few studies seem to exist (*Jackson et al.*, Accepted; *Al Bitar et al.*, Accepted). The objective of this article is to present the comprehensive validation work carried out at the Danish validation site. This includes analysis of the SMOS L1C/L2 products as well as the most sensitive algorithm parameters by means of the network and airborne campaign data sets. Previous findings from *Bircher et al.* (Accepted,S) are picked up, and together with results of more in-depth analysis put in context with the studies at other Cal/Val sites. Based upon this, most likely error sources for the current discrepancies at the Danish site are located.

7.2. Study site/data

7.2.1. Location/environmental conditions

The Skjern River Catchment is situated in Western Denmark and covers approximately 2500 km^2 (Fig. 7.1). The climate is temperate-maritime with mean winter/summer temperatures of ∼2/16 °C, respectively, and an approximate annual precipitation of 800-900 mm. The eastern margin of the catchment is situated at the rim of the ice sheet during the latest glacial advance with mainly loamy soils on undulating calcareous tills. The major part comprises the primal fluvioglacial outwash plain with very sandy soils and sediments (75-100 % sand), while poorly drained basins have been filled with organic material (*Greve et al.*, 2007). The natural soil type is podsol covered by a pronounced moss and raw humus layer (∼5-20 cm thick). Nearly 80% of the land is under intensive cultivation, intermixed with patches of spruce forest (∼10%), as well as heath/grassland (∼6%). The area is sparsely populated. Within the catchment four HOBE study sites (*Jensen and Illangasekare*, 2011, Fig. 7.1b) have been maintained to assess a wealth of hydrological parameters. The catchment is well-covered with climate and weather stations operated by the Danish Meteorological Institute (DMI). The daily precipitation data presented in this article are extracted from the DMI 10x10 km precipitation grid nodes (*Scharling*, 1999) contained within the SMOS pixel (Fig. 7.1). For each day the shelter correction factor of the corresponding month (category B) is applied (*Vejen et al.*, 2000). The SMOS pixel around DGG node 2002029 (55.957 N, 9.131 E) was chosen for validation as it features minimal open water fraction while covering a substantial part of the catchment (Fig. 7.1a+b *Bircher et al.*, Submitted).

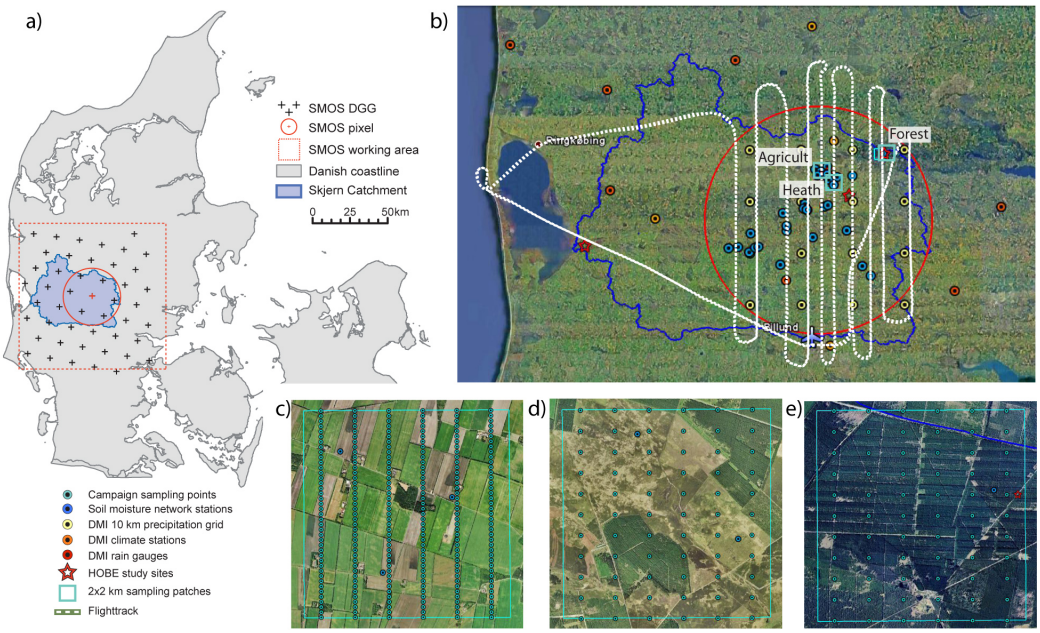

Figure 7.1.: Overview over the validation site: a) Danish coastline, Skjern River Catchment, SMOS pixel (44 km diameter) and working area (123x123 km) around grid node 2002029, b) HOBE study sites, campaign flight tracks and sampling patches, soil moisture network stations, DMI climate stations, rain gauges and 10 km precipitation grid, c) agriculture, d) heath, and e) forest campaign ground sampling transects within respective 2x2 km patches.

7.2.2. Soil moisture and temperature network

A soil moisture and temperature network with 30 stations spatially distributed within SMOS pixel 2002029 was installed during fall 2009. To a priori enhance the likelihood of a representative large-scale network average for comparison with SMOS data, the individual stations were distributed according to the respective fractions of six so-called composite classes combining 82% of the prevailing land cover, top- and subsoil conditions (*Bircher et al.*, Submitted). Crop type frequency was also considered, and the network was aligned with the long-term mean annual north-east - south-west precipitation gradient (Fig. 7.1b). Per station, soil moisture and temperature within the 0-5 cm, 20-25 cm and 50-55 cm depth ranges of the mineral soil, and in the organic layer in case of the sites with natural vegetation (forest and heath), are measured by means of ECH2O 5TE capacitance sensors[1] and logged at 30 minute intervals. Soil moisture calibration checks for the 0-5 cm layer showed that sensor accuracy was within the declared +/-0.03 m^3/m^3 range, which is in line with sensor accuracies of other large scale studies (e.g. *Brocca et al.*, 2010; *Albergel et al.*, 2011). From soil samples taken at the 0-5 cm depth of each network station, percentages of sand, silt and clay were determined using standard procedures, and soil bulk densities calculated.

[1]Mention of manufacturers is for the convenience of the reader only and implies no endorsement on the part of the authors

7.2.3. Airborne campaign

The HOBE airborne campaign (*Bircher et al.*, 2010, Accepted) took place in spring 2010. Four flights with the passive L-band microwave radiometer EMIRAD-2 (*Skou et al.*, 2010a) were carried out around SMOS ascending overpasses (∼06:30 a.m. local time) as shown in Fig. 7.1b. Simultaneously, ground measurements were taken within three 2x2 km patches (agricultural land, heath/grassland and forest, Fig. 7.1c-e). The -3dB swath width was ∼1.4 km resulting in ∼35/75% coverage of the SMOS pixel/ground patches, respectively. Measurements were acquired at 0 and 40° incidence angles and in full polarization mode. The EMIRAD data was calibrated, RFI-filtered and georeferenced to the ground using standard procedures (*Bircher et al.*, Accepted).

Moisture of the mineral soil was measured with hand-held Delta T ML2x ThetaProbes[2] (0-6 cm depth) along several transects and at some locations gravimetric samples were taken. The data was recalculated using site-specific calibration curves. In case of heath and forest, readings/samples were also acquired from the moss/organic layers at the cost of less sampling points. Land cover information was recorded for each sampling point. At the beginning and towards the end of the campaign destructive vegetation sampling for vegetation water content (VWC) estimation was carried out on agricultural land and heath. Surface roughness transects were measured on a flat barley field as well as on a potato field with pronounced row structure (spanning the expected conditions) and standard deviations of the height, S_D calculated. At the beginning the majority of agricultural fields were of bare appearance. During the campaign a significant increase in vegetation water content was observed within heath and agricultural land, along with an increase in overall roughness due to the ongoing plantatation of potatoes.

7.2.4. SMOS

The SMOS measurement and soil moisture retrieval concept is described in detail in *Kerr et al.* (2010, 2011, Submitted). The received radiation (proportional to T_B) used for the retrieval at each DGG node per SMOS overpass originates from the so-called working area (∼123x123 km). It integrates observations ('snapshots') made at horizontal and vertical polarizations (H and V) and a range of incidence angles (∼0-60°)/view directions, and is weighted by the shape of the SMOS antenna pattern. Thus, ∼80-90% of the signal are emitted from the center area with a diameter of ∼44 km.

The auxiliary parameters to initiate the algorithm are provided on a 4x4 km grid (Discrete Flexible Fine Grid, DFFG) spanning the working area of each DGG node. They include land cover information (ECOCLIMAP), soil property data (% sand and clay from the Food and Agriculture Organization of the United Nations (FAO) data set, soil bulk density from the Global Gridded Surfaces of Selected Soil Characteristics for International Satellite Land Surface Climatology Project, ISLSCP), Leaf Area Index (LAI from the MODerate Resolution Imaging Spectroradiometer, MODIS), as well as the first soil moisture guess, temperature and other climate parameters (European Centre for Medium-range Weather Forecasting, ECMWF, products) (*Bengoa et al.*, 2010). The SMOS L2 processor uses different forward model versions with specific parameters for different land covers to account

[2]Mention of manufacturers is for the convenience of the reader only and implies no endorsement on the part of the authors

for mixed land cover pixels at large spatial scales. The ECOCLIMAP database is grouped into few generic classes. Non-permanent land cover classes (e.g. frost and snow) are successively updated based on the ECMWF product. Radiometric land cover fractions (referred to 'FMO fractions' hereafter) are estimated for the working area by means of the antenna weighting pattern. The class with the highest radiometric fraction determines the choice of the forward model and auxiliary input, while the other classes contribute with fixed default values.

L-MEB is based on the relationship between T_B, physical temperature T and emissivity e/reflectivity Γ, which in turn is related to the soil's dielectric constant after segregating atmosphere, vegetation and surface roughness contributions (Fig. 7.2). Taking advantage of the large contrast between the dielectric properties of water and solid soil particles at L-band, soil moisture is linked to the dielectric constant via the Dobson dielectric mixing model (*Dobson et al.*, 1985; *Peplinski et al.*, 1995). The replacement with the Mironov model (*Mironov et al.*, 2004) is currently under discussion. While Dobson is empirically-derived from data sets with sand fractions $< 50\%$, Mironov is physically-based and built upon data sets spanning the entire soil type range up to pure quartz sand. Dobson requires soil moisture and temperature, clay and sand %, dry soil bulk density and solid particle density as input, Mironov only uses the first three. Atmospheric attenuation of L-band emissions is generally low. Several parameters are used in L-MEB to describe the vegetation transmissivity, namely the single scattering albedo of the canopy (ω), vegetation optical depth at nadir (τ_{NAD}) and its incidence angle correction for non-nadir views at both polarizations (tt_H/tt_V). The correction of surface roughness is done by parameters representing the intensity of the effects (H_R), polarization mixing effects (Q_R), and modulation of the reflectivity as a function of the incidence angle for both polarizations (N_{RH}/N_{RV}). In addition to soil moisture, the soil characteristics (temperature, texture and bulk density) and the choice of τ_{NAD} and H_R have most impact on the modeled T_Bs (highlighted in red in Fig. 7.2, e.g. *Pardé et al.*, 2004; *Grant et al.*, 2008; *Panciera et al.*, 2009a; *Cano et al.*, 2010).

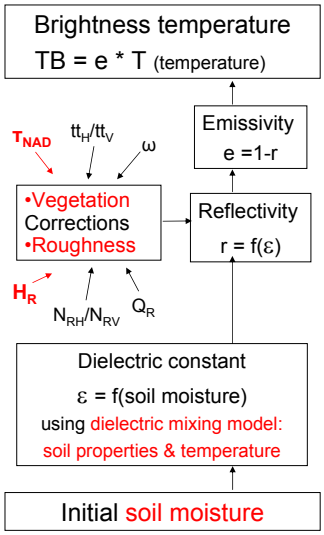

Figure 7.2.: Simplified schematic illustration of the L-band Microwave Emission of the Biosphere, L-MEB, forward model.

7.3. Previous SMOS validation results

7.3.1. Soil moisture and temperature network (*Bircher et al.*, Submitted)

A first comparison between the 0-5 cm network averages and the SMOS soil moisture (L2) product over the year 2010 showed comparable trends with R^2 of 0.49/0.67 for SMOS retrieved/initial soil moisture. The corresponding RMSE and biases (average residuals from expected value) are 0.102/0.061 m^3/m^3 and -0.092/0.057 m^3/m^3, indicating significant under-/overestimation of the network data. The precipitation seemed well reflected over time in both network and SMOS soil moisture, but with larger amplitudes in case of the retrieved L2 product. The agreement between the 0-5 cm network temperature average and the initial SMOS surface temperature is very good with RMSE, bias and R^2 of 1.1 °C, -0.2 °C and 0.97, which is in accordance with findings from *Jackson et al.* (Accepted). Likewise, we assume that no uncertainty is introduced in the retrieval algorithm by this parameter. The comparison of the dielectric constant's real part (direct sensor output) network average and the SMOS dielectric constant's real part derived from a non cardioid model revealed RMSE, bias and R^2 of 3.95 F/m, -2.30 F/m and 0.49. As the SMOS dielectric constant is computed from retrieved soil moisture using the Dobson model, an R^2 equal to the one of the soil moisture comparison implies that at both comparison levels the uncertainty is consistent and remains either on the network or the SMOS data side.

7.3.2. Airborne campaign (*Bircher et al.*, 2010, Accepted)

Constantly small rain events occurred before and during the campaign, leading to low temporal soil moisture variability, while the spatial variability was generally high. In agreement with data recordings in Northern Germany (*Montzka et al.*, Accepted) driest conditions were found in the mineral soils of the agriculture patch. Highest moisture contents were clearly found in the organic layers in the heath and forest patches, implying that with maximum likelihood L-band emissions originate from this substrate (*Bircher et al.*, 2010).

From the mineral soil moisture data T_Bs were point-wise estimated by means of L-MEB using land-cover specific settings, and patch-wise averaged for comparison with EMIRAD. (*Bircher et al.*, Accepted). The uncertainty in the modeled T_Bs turned out to be very high (5-20 K) when the most sensitive model parameters were varied within most likely value ranges. However, for each land cover class a combination of parameters could be selected to bring modeled and EMIRAD data in good agreement. Replacing Dobson with the Mironov model decreased the overall RMSE from 11.5 K to 3.8 K, which is plausible given the high sand contents in the Skjern River Catchment. RMSEs were largest in case of agricultural land, which is consistent with results of *Montzka et al.* (Accepted). They explain it with higher variability within the intensely cultivated area. However, we found the spatial variability in agriculture to be significantly smaller than in forest and heath. We rather attribute the good fit in the two latter to parameter tuning. Considering only the mineral soils, resulted in compensation of the τ_{NAD} and H_R parameters for the neglected wet organic substrate (lower values within the uncertainty range compared to agriculture). Still, the chosen H_Rs for all land covers were significantly higher than the SMOS default, which is concordant with literature findings(e.g. *Panciera et al.*, 2009a,b; *Saleh et al.*, 2009). Using an N_{RH}/N_{RV} combination of 0/-1 instead of the SMOS default 2/0 further increased the agreement.

EMIRAD data averaged at SMOS scale and corresponding SMOS T_Bs were also in the same range with a positive offset of the airborne data (mean RMSE=9.7 K). However, strong RFI limited this comparison to one day (May 2). The bias clearly increased when comparing the mean modeled patch T_Bs averaged over the SMOS pixel using the respective FMO fractions as weights (average RMSE of 15.9 K). This issue will be resumed in Section 7.5. Neither using the EMIRAD antenna pattern to weight the average of the modeled T_Bs nor the SMOS antenna pattern to estimate a weighted mean of EMIRAD data over the SMOS pixel did improve the results over simple averaging.

7.4. Methods

7.4.1. SMOS data preparation

All SMOS data used in this work stems from consistent data sets reprocessed by means of the state of the art L1/L2 prototype algorithm (V3.46/V4.00) in case of the L1C/L2 products, respectively. L1C data was transferred from antenna to Top Of Atmosphere (TOA) level (XY to HV) by applying Faraday and geometric rotations. L1C and L2 data were filtered using two criteria from the L2 product (*Bengoa et al.*, 2010): (1) absolute abscissa of dwell line (X_SWATH) < 10000 (corresponding to ∼320 km out of max. 1000 km swath width), (2) probability that no anomaly occurred about the fit ($CHI2\_P$) > 0.5. If the X_SWATH is too large, only a limited number of snapshots were available for the retrieval. There could also be image reconstruction issues at the edge of the swath (*Jackson et al.*, Accepted). A high enough $CHI2\_P$ makes sure that retrievals where the modeled and measured T_Bs fully disagree (e.g. RFI) or fit too well (only few snapshots) are discarded. Two additional criteria previously applied in *Bircher et al.* (Accepted) turned out redundant. In case of the L1C data only one month around the airborne campaign was used. Filtered T_Bs were further cut off at 300 K. After filtering the L2 product of DGG node 2002029 for the entire year 2010 41% of the data, from ascending (morning) overpasses only, were left. At the U.S. validation sites *Leroux et al.* (Submitted); *Jackson et al.* (Accepted) both reported less good validation performance of the descending (evening) overpasses. A clear advantage of the ascending overpasses is the nearly thermal equilibrium state between atmosphere, vegetation and ground in the early morning, which favors the retrieval. *Jackson et al.* (Accepted) further suggested a disturbing impact of convective rainfall during the times of the descending overpasses at the studied watersheds. However, at the Danish site we assigned the majority of the filtered data to RFI contamination. For a test period (April - June 2010) our filtering was checked against an RFI detection scheme based on SMOS level 1A data developed by *Anterrieu* (2011). This pointed to the same overpasses being affected by RFI when using the number of snapshots affected by RFI $<$ 35% and the total number of available snapshots > 140 as thresholds.

7.4.2. Further SMOS data validation

Refined soil moisture comparison

For each SMOS overpass (filtered data) during the year 2010, the two nearest half-hourly network measurements were extracted and averaged. This data was compared with the initial and retrieved SMOS soil moisture, and put in relation with the original network -

retrieved SMOS soil moisture comparison using unfiltered data (*Bircher et al.*, Submitted). To check whether certain subgroups could possibly better explain the SMOS data than the entire network, the comparison was also performed with the network data set grouped into (1) soil type classes after *Greve et al.* (2007) according to the estimated network texture data, (2) land cover classes as recorded at each station, and (3) composite classes (jointed land cover and soil type information) as used to place the network stations (see 7.2.2 and *Bircher et al.*, Submitted). Specifications about these subgroups are given in Table 7.1. It was also investigated whether the agreement was depending on seasons by grouping the data accordingly (winter: January-February and December, spring: March-May, summer: June-August, autumn: September-November).

Refined brightness temperature comparison

An attempt was made to model brightness temperatures from the soil moisture data of the mineral soil of each network station during a month centered on the campaign window (April 18 - May 18, 2010). The modeled network T_Bs at 40° incidence angle were averaged over all stations for H and V, respectively, and compared to the corresponding SMOS L1C data (average between 35 and 45° incidence angles), the EMIRAD T_Bs as well as the modeled campaign in situ data. With respect to the last, the mean modeled patch T_Bs were averaged over the SMOS pixel using the respective FMO fractions as weights (bare soil and low vegetation 'FNO' with 90/10% for agriculture and heath, respectively., and forest 'FFO' fractions: 77% agriculture, 8% heath and 15% forest, referred to 'weighted model patch averages' hereafter).

Taking advantage of the findings from the analysis on the solid airborne campaign data sets of high spatial coverage, the L-MEB settings were adopted from *Bircher et al.* (Accepted). Thus, parameters not mentioned in the following are set to values congruent with the one of the previous study. The Mironov dielectric mixing model was applied and N_{RH}/N_{RV} set to 0/-1, respectively. Soil temperatures were extracted from the respective network station measurements and the clay percentages estimated from the respective network texture data.

In case of H_R constant values were chosen for the entire month. For heath and forest classes 1.1 and 1.0 were applied while in case of the agriculture classes distinction was made between flat conditions (spring/winter cereal and grass) and rough conditions (bare potato fields) with assigned values of 0.58 and 1.17, respectively. The soil moisture-dependent parameterization of H_R was neglected (i.e. H_R=H_{R_Min}) as it remains controversial (*Escorihuela et al.*, 2010).

A constant τ_{NAD} of 0.2 was chosen for the entire month in case of coniferous forest. For the heath and agricultural land classes τ_{NAD} was derived from the vegetation water content estimations during the campaign. As there was a significant increase in VWC, it was interpolated between the two sampling dates (April 28 and May 06) and extrapolated to span the entire month. The only exception was agriculture grass where only one measurement was available per sampling day so that an average value of 0.274 was constantly used. From these monthly VWC data sets τ_{NAD} values were calculated using the linear relationship developed by *Jackson and Schmugge* (1991): $\tau_{NAD} = b \cdot VWC$, where b is a vegetation parameter, amongst others dependent on canopy type/structure. b was defined per land cover class based on literature: 0.15 for cereal and 0.3 for agriculture grass (e.g. *Jackson*

and Schmugge, 1991), and 0.12 for scotch heather and natural grass (e.g. *Saleh et al.*, 2007)). This resulted in τ_{NAD} values (April 28/May06) of 0.039/0.073 for natural grass, 0.058/0.083 for scotch-heather, 0.002/0.021 for spring cereal, and 0.090/0.185 for winter cereal, respectively. Due to the extrapolation at the beginning of the time span some of the values were negative and thus, adjusted to 0. This is reasonable as the fields were just prepared and sown in this period. The comparably low values in case of forest and heath classes result from the compensation for the not considered organic layers (see 7.3.2 and *Bircher et al.*, Accepted).

Comparison of initial/retrieved SMOS τ_{NAD} with in situ modeling τ_{NAD}

The SMOS initial τ_{NAD} is originally obtained from the MODIS LAI data product.

For each retrieval the SMOS initial τ_{NAD} is either updated with the retrieved value of the previous overpass if its reliability is high enough according to the Data Quality Index (DQX, retrieved standard deviation), or anew derived from the MODIS LAI data product, where it first originates from. For comparison with the SMOS initial and retrieved τ_{NAD} the in situ τ_{NAD} values used for the modeling of each campaign sampling point were aggregated over the respective patches (agriculture, forest and heath). The average was weighted by the fractions of the respective land cover classes within each patch (noted for each point during the sampling). As these fractions were temporally variable for the agriculture patch, they were again estimated for each day by interpolating/extrapolating between/around the campaign days, and where negative adjusted to 0. We are aware of the fact that such an averaging might not correspond to the full truth as the vegetation optical depth exhibits nonlinear effects over scales. However, we believe it still gives an impression of the expected order of magnitude of this parameter at larger scales.

Comparison of SMOS soil properties (FAO/ISLSCP) with in situ samples

The SMOS FAO soil texture (% clay and sand) and ISLSCP soil bulk density of DGG node 2002029 at 4 km grid spacing were aggregated by computing (1) simple averages (geometric mean) for the working area and the SMOS pixel, and (2) a weighted average for the working area by means of the SMOS antenna weighting pattern (radiometric mean). For comparison the corresponding in situ soil property data (0-5 cm depth) were aggregated (1) by averaging the respective values from the individual network samples, and (2) by averaging the respective values from all campaign samples within each sampling patch (agriculture, forest and heath). Again, these three patch means were averaged over the SMOS pixel using the FMO fractions as weights (see Section 7.4.2).

Comparison of SMOS FMO land cover fractions (ECOCLIMAP) with CORINE Land Cover 2000

Finally, land cover fractions of the CORINE Land Cover Classification 2000 (*EEA*, 2005) at 100 m grid spacing were averaged over both the working area as well as the SMOS pixel (geometric mean) of DGG node 2002029. These averages were then compared with the correpsonding SMOS FMO fractions (ECOCLIMAP) at 4 km grid spacing (radiometric mean over working area).

7.5. Results and discussion

7.5.1. Refined soil moisture comparison

Fig. 7.3 displays the comparison of the 0-5 cm network soil moisture average over all 30 stations with the initial and filtered retrieved SMOS soil moisture data for the year 2010. The corresponding average mean of daily precipitation of the DMI 10 km grid nodes contained within SMOS pixel 2002029 as well as the FMO fractions are plotted along. The last one show that no retrieval was performed when the soil was frozen or snow covered. Precipitation seems to be well reflected by both SMOS and in situ data and we can see a clear trend between the soil moisture data sets. Still, the dynamic of the retrieved SMOS data is stronger and the significant overestimation/underestimation of SMOS initial/retrieved soil moisture compared to the network data clearly visible. RMSEs, biases and R^2s between network and SMOS are 0.061/0.094 m^3/m^3, 0.057/-0.087 m^3/m^3 and 0.67/0.61 for initial/retrieved SMOS soil moisture, respectively.

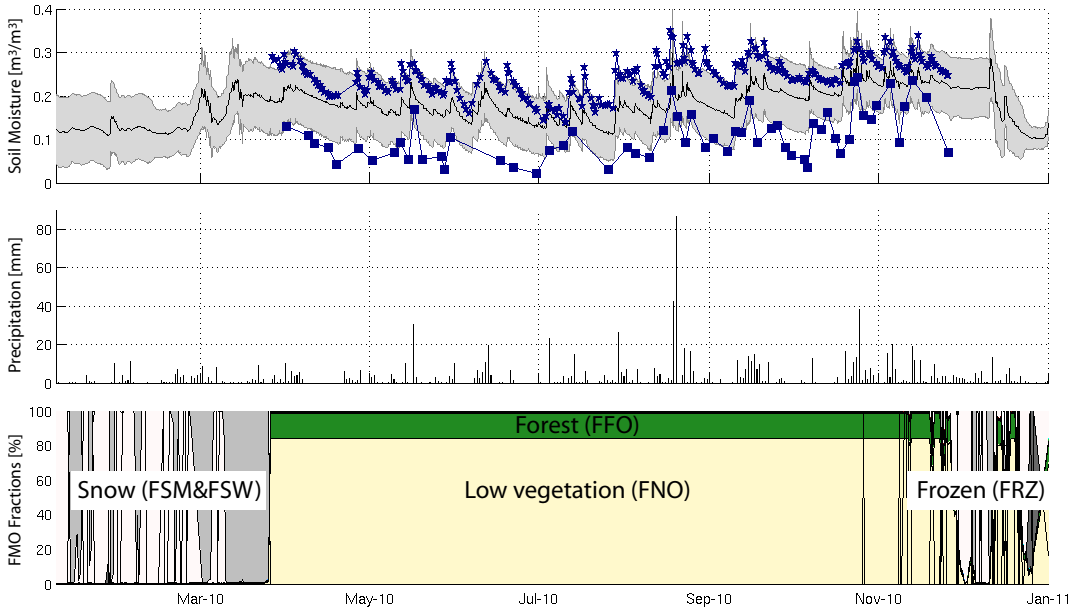

Figure 7.3.: Soil moisture (top panel): Average and standard deviation of 0-5 cm network soil moisture (black line and grey-shaded region), and initial/filtered retrieved SMOS L2 soil moisture (dark blue star/square) of grid node 2002029; mean of daily precipitation of 10 km precipitation grid nodes contained within the SMOS pixel (center panel); SMOS FMO fractions (bottom panel); January - December 2010.

Fig. 7.4 depicts a scatter plot of the 0-5 cm soil moisture network average and the filtered as well as the unfiltered retrieved SMOS data for the entire year 2010. The corresponding statistics (Table 7.1) demonstrate a clear improvement in the R^2 from 0.49 to 0.61 and a slight decrease in the RMSE/bias from 0.102/-0.092 to 0.094/-0.087 m^3/m^3 for the unfiltered/filtered SMOS data, respectively. Likewise, the statistics of the dielectric constant's real part comparison improved when using the filtered SMOS data from the non Cardioid model with RMSE, bias and R^2 of 3.5 F/m, -2.5 F/m and 0.62 (not shown).

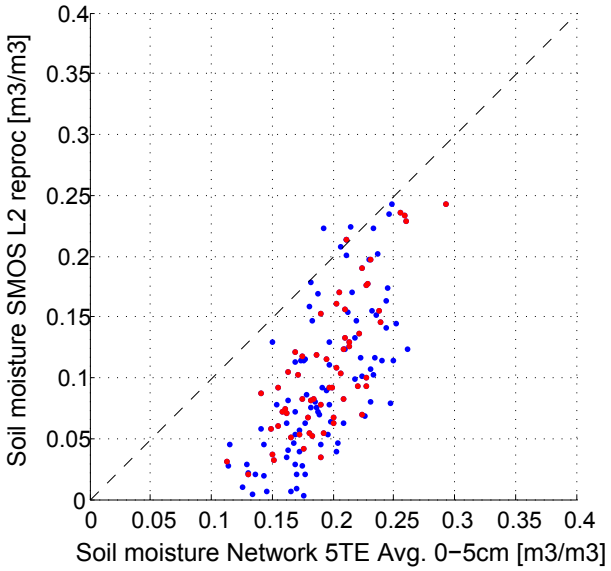

Figure 7.4.: Average 0-5 cm network soil moisture plotted against the filtered (red) and unfiltered (blue) retrieved SMOS data of grid node 2002029 for the entire year 2010.

Fig. 7.5 shows the comparison of the filtered retrieved SMOS data with 0-5 cm soil moisture network data grouped into (a) soil types, (b) land cover classes, (c) composite classes, and (d) four seasons. The statistics (Table 7.1) indicate that overall only the sand class and the summer period by itself achieve as good statistical results as the entire network average. It is not surprising that the sand class behaves very similarly as it includes 80% of the stations. Furthermore, a slightly smaller bias for the comparably dry sand stations only is logic given the SMOS dry bias. The better agreement over the summer months is in line with *Rüdiger et al.* (2011b) who reported a more pronounced bias in winter compared to the summer at the Australian SMOS Cal/Val site. The fact that none of the subgroups performs significantly better enhances our confidence in the representativeness of the chosen network setup.

7.5.2. Refined brightness temperature comparison

Fig. 7.6 shows surface soil moisture measured by the network, by means of the campaign readings and filtered initial/retrieved SMOS data, the mean of daily precipitation of the DMI 10 km grid nodes contained within SMOS pixel 2002029, and corresponding brightness temperatures at 40° incidence angle and for H and V polarizations, respectively, for a month centered at the airborne campaign (April 18 - May 18, 2010). In terms of brightness temperatures filtered SMOS L1C data is depicted together with the EMIRAD data, weighted model patch averages of the campaign data, and the modeled network average. The soil moisture network data includes the 0-5 cm average over all stations as well as data of one station within each campaign sampling patch (agriculture, heath and forest). In case of the campaign data the three patch means and their weighted average over the SMOS pixel using the FMO fractions are shown.

Table 7.1.: Statistics (RMSE, bias, R^2) of comparison between average 0-5 cm network soil moisture and retrieved SMOS data of grid node 2002029 for the entire year 2010, for unfiltered and filtered SMOS data, and network data grouped into soil type classes, land cover classes, composite classes, and four seasons, for filtered SMOS data. Specifications on the subgroups and respective fractions [%] are indicated. TS = topsoil, SS = subsoil.

Network data	Subgroups	Specification	Fraction	RMSE	BIAS	R^2
All unfiltered				0.102	-0.092	0.49
All filtered				0.094	-0.087	0.61
Soil types	Sand	75-100% sand, 0-5% clay	80	0.087	-0.079	0.61
	Loamy sand	65-95% sand, 5-10% clay	13.3	0.103	-0.089	0.35
	Sandy loam	55-90% sand, 10-15% clay	3.3	0.152	-0.148	0.62
	Clay	40-85% sand, 15-25% clay	3.3	0.226	-0.217	0.26
Land cover	Heath		13.3	0.144	-0.138	0.5
	Forest		13.3	0.071	-0.057	0.55
	Agriculture winter cereal		16.7	0.085	-0.077	0.55
	Agriculture grass		16.7	0.122	-0.117	0.59
	Agriculture potato		10	0.057	-0.034	0.5
	Agriculture spring cereal		30	0.076	-0.061	0.41
Composite classes	612	Heath, topsoil sand, subsoil sand	13.3	0.144	-0.138	0.5
	512	Forest, topsoil sand, SS sand	13.3	0.071	-0.057	0.55
	211	Agriculture, TS sand, SS clay	6.7	0.150	-0.146	0.66
	212	Agriculture, TS sand, SS sand	53.3	0.068	-0.058	0.59
	232	Agriculture, TS loamy sand, SS sand	6.7	0.190	-0.179	0.19
	292	Agriculture, TS organic-rich, SS sand	6.7	0.098	-0.090	0.47
Seasons	Spring			0.102	-0.098	0.39
	Summer			0.085	-0.078	0.63
	Fall			0.095	-0.086	0.6
	Winter			NaN	NaN	NaN

The figure assembles previous findings and shows that the pattern prevails throughout the added data from the one month period. The weighted model patch averages are constantly drier than the network averages as the campaign sampling patches only exhibit very sandy soils with comparably dry conditions, while the network also observes the 'wetter' more clayey soils. Likewise, the more pronounced SMOS L1C data T_B overestimation by the weighted model patch average compared to the one by EMIRAD is probably attributable to these scale effects. In contrast, the average modeled network T_Bs show a consistent underestimation of the SMOS T_Bs, which would actually be expected to explain the higher network soil moisture values compared to the ones retrieved by SMOS. Indeed, several studies report a warm bias of SMOS T_Bs compared to tower-based and airborne radiometer measurements as well as modeled in situ data (*Kontu et al.*, 2010; *Rüdiger et al.*, 2011b; *Montzka et al.*, Accepted). However, for short time periods the opposite trend with lower SMOS T_Bs was also discovered in the studies of *Kontu et al.* (2010) and *Montzka et al.* (Accepted). As we only have few campaign sampling days to compare with, it is thus likely that a differing pattern could persist over longer timeframes. The difference in modeled average network and campaign T_Bs seems too large to be solely explicable by the described scale effects. A major part is probably connected to the large uncertainties inherent in the T_B modeling (*Montzka et al.*, Accepted; *Bircher et al.*, Accepted), which can be especially pronounced at small spatial scales (*Schlenz et al.*, Accepted). In the network data modeling uncertainties are clearly enhanced compared to the campaign data modeling as we have less direct observations for each station/day (e.g. information on land cover and surface conditions). Due to persistent low rainfall variability during the observation period it is difficult to make statements about the temporal dynamics in the data. However, the modeled

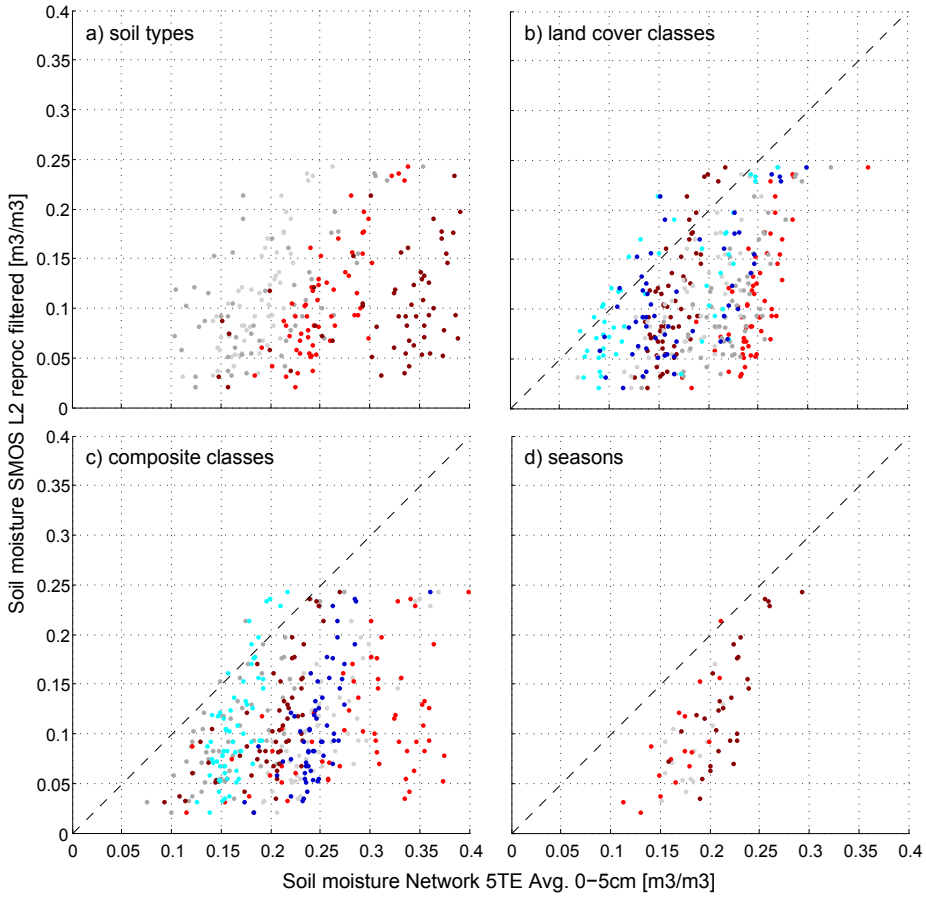

Figure 7.5.: Average 0-5 cm network soil moisture plotted against the filtered retrieved SMOS data of grid node 2002029 for the entire year 2010, with network data grouped into (a) soil type classes: sand (light grey), loamy sand (dark grey), sandy loam (red), clay (dark red);(b) land cover classes: heath (red), forest (dark red), winter cereal (light grey), agriculture grass (dark grey), potato (light blue), spring cereal (dark blue) ;(c) composite classes: 211 (light grey), 212 (dark grey), 232 (red), 292 (dark red), 512 (light blue), 612 (dark blue); (d) four seasons: spring (light grey), summer (red), fall (dark red), winter (no retrieval).

network data is clearly not able to capture the two more significant rain events towards the end of the studied time window, while they are well-reflected in the respective soil moisture data. A further comparison between modeled T_Bs of individual overflown network stations with corresponding EMIRAD data also pointed to quite large deviations between the two, especially in case of stations within cereal fields and less sandy soils (not shown). But the reliability of such a comparison of two measurements integrating over very different spatial scales is again questionable.

7.5.3. Comparison of initial/retrieved SMOS τ_{NAD} with in situ modeling τ_{NAD}

The lowest panel in Fig. 7.6 shows the initial and filtered retrieved SMOS τ_{NAD} and the corresponding τ_{NAD} values on average used for the in situ modeling within the agriculture, heath and forest patches, respectively.

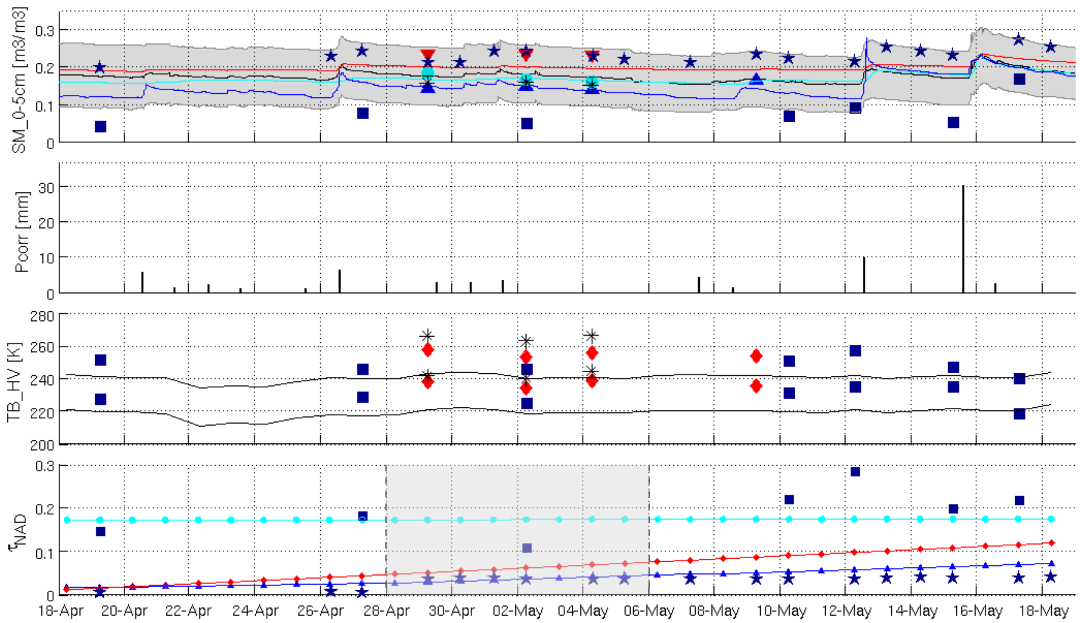

Figure 7.6.: Surface soil moisture (top panel): 0-5 cm network average and standard deviation (black line and grey-shaded region), 1 network station/campaign sampling patch average in agriculture (medium blue line/triangle), forest (light blue line/circle) and heath (red line/triangle), weighted model patch average over SMOS pixel (black asterix), SMOS L2 initial/filtered retrieved (dark blue star/square); mean of daily precipitation of 10 km precipitation grid nodes contained within the SMOS pixel (second panel); brightness temperatures, H/V polarization (lower/upper data), at 40° incidence angle (third panel): EMIRAD (red diamond), weighted model patch average (black asterix), model network average (black line), SMOS L1C (dark blue square); τ_{NAD} (bottom panel): campaign sampling patch average in agriculture (medium blue line/triangle), forest (light blue line/bullet) and heath (red line/triangle) SMOS L2 initial/filtered retrieved (dark blue star/square), period between vegetation sampling dates is marked as grey-shaded region; April 18 - May 18, 2010.

The SMOS initial τ_{NAD} follows the mean agriculture τ_{NAD}, especially between the two vegetation sampling days, with a likewise increasing trend. During the entire month, the S_TREE_1 parameter in the SMOS L2 product was set to 12, meaning that retrieval based on the FNO settings (low vegetation) was triggered. This is in accordance with the FMO fractions depicted in Fig. 7.3. Thus, the applied initial τ_{NAD} seems to be in the right order of magnitude. The retrieved SMOS τ_{NAD} values lie in considerably higher range which is meaningful as the retrieved value should now also account for the forest contribution (high vegetation opacity). However, as they are actually in the order of the mean forest τ_{NAD}, we assume them to be too high. Also, the data is very noisy, though an increasing tendency is visible.

The observation period is too short for a final statement on the behavior of the vegetation optical depth. However, our findings are in good agreement with the ones of *Jackson et al.* (Accepted) who studied longer time frames at some watersheds in the U.S. They suspect the large day to day variability (not relatable to changes in vegetation) to be associated with the shift between using the updated retrieved τ_{NAD} value of the previous overpass and the estimates from the MODIS LAI data as model input. They also report a positive bias as

Table 7.2.: Soil properties (sand and clay fractions [%], bulk density [g/cm^3]) of SMOS grid node 2002029: FAO/ISLSCP data used in the SMOS retrieval algorithm, geometric and radiometric mean of the working area (= geometric mean pixel), and 0-5 cm in situ data, average of network samples and weighted average of campaign patch samples (77% agriculture, 9% heath, 15% forest).

	Sand	Clay	Bulk density
SMOS geometric mean working area	58	17	1.05
SMOS radiometric mean working area	71	11	0.88
Network samples 0-5 cm average	87	4	1.22
Campaign samples 0-5 cm weighted average	90	3	1.24

well as a lack of seasonal response and point out that at this stage the retrieved parameter is not a reliable indicator of VWC. Similarly, *Al Bitar et al.* (Accepted) reported for other U.S. validation sites that the retrieved SMOS τ_{NAD} did not exhibit a clear correlation with the MODIS LAI.

7.5.4. Comparison of SMOS soil properties (FAO/ISLSCP) with in situ samples

Table 7.2 lists the average fractions (geometric mean of working area and SMOS pixel and radiometric mean for the former) of the SMOS FAO/ISLSCP soil properties for DGG node 2002029 as well as the network and campaign 0-5 cm sample averages derived for the corresponding SMOS pixel. As expected, the percentages of the geometric SMOS pixel mean turned out to be congruent with the respective radiometric averages over the working area. Compared to the pixel the sand fraction is lowered for the entire working area, while clay fraction and bulk density increase. The fractional shift in the soil texture is in line with the Danish soil grid by *Greve et al.* (2007), though this soil type classification is not directly comparably with the absolute values of the FAO texture grids. The averages of the two in situ data sets are in comparable range, though naturally the network average shows a bit less sandy conditions. What clearly stands out is that the SMOS average sand fraction and bulk density values for the pixel are about 18% and 0.35 g/cm^3 lower than the in situ values, while for clay fraction it is about 8% higher.

7.5.5. Comparison of SMOS FMO land cover fractions (ECOCLIMAP) with CORINE Land Cover 2000

Table 7.3 shows the FMO fractions (radiometric mean of the working area) of DGG 2002029 together with the land cover fractions of the CORINE Land Cover Classification 2000 averaged over the working area and the SMOS pixel (geometric mean). There are no distinct differences between the average CORINE land cover fractions for the working area and the SMOS pixel. As in case of soil properties, we expect the radiometric mean of the working area to be congruent with the pixel geometric mean. The FMO fractions assume a slightly higher portion of low vegetation and lower urban land and wetland parts than CORINE2000. However, these fractional shifts seem to be insignificant. Water body and wetland fractions which could significantly impact the emission only exhibit marginal parts. We thus conclude that the FMO fractions used in the SMOS retrieval are in good agreement with the average CORINE land cover fractions.

Table 7.3.: Land cover fractions [%] of SMOS grid node 2002029: FMO fractions (ECOCLIMAP) used in the SMOS retrieval algorithm, radiometric mean of the working area, and CORINE LAND COVER 2000 fractions, geometric mean of working area and pixel.

	FMO/ECOCLIMAP Working area	CORINE2000 Working area	Pixel
Low vegetation (FNO)	84.16	82.32	80.36
Forest (FFO)	14.45	10.5	14.36
Urban land (FEU)	0.55	4.78	3.21
Wetlands (FWL)	0.43	1.47	1.81
Open water (FWO)	0.4	0.87	0.26

7.5.6. Synthesis

All findings from the extensive SMOS validation at the Danish site are compiled in Table 7.4. In the following they are discussed in a synthesized fashion in order to determine the most likely error sources for the encountered deviations out of the list of possible explanations introduced in Section 7.1.

Preliminary inspection of the network and campaign measurements gave confidence in reliable data sets. The network subgroup analysis further consolidated our trust in a representative setup for large-scale applications. Furthermore, our results are well in range with worldwide Cal/Val findings. Thus, we do not believe that the major discrepancies between the SMOS products and in situ data originate from pronounced faultiness of the latter.

With respect to the larger amplitudes in the retrieved SMOS soil moisture data, different measurement depths between in situ sensors (∼0-5 cm) and SMOS (<5 cm), and the corresponding faster and stronger response to wetting and drying at shallower depth, are a plausible explanation (e.g. *Jackson et al.*, Accepted; *Al Bitar et al.*, Accepted). As suggested by *Rüdiger et al.* (2011b) ponding water on vegetation after excessive rain events could further contribute. This is to be investiaged at the Danish site. Meanwhile, distinct rain events not captured by individual network stations but integrated into the SMOS data are not expected to constitute a significant error source as the spatial rain variability turned out to be small within the Danish validation area.

Spatial scaling effects constitute a further issue. A too small amount or not representative set of in situ measurements can easily provoke a bias when aggregated at larger scales. *Montzka et al.* (Accepted) addressed the deviations when comparing airborne radiometer data with different footprints as were likewise encountered for the Danish site when comparing aggregated modeled in situ, EMIRAD and SMOS data. *Gruhier et al.* (Submitted) noted that averaging in situ data over several stations clearly improved the temporal correlation with retrieved SMOS soil moisture compared to single stations. However, there was no significant change in the associated RMSE. Similarly, we found for our in situ network that none of the subgroups could explain the temporal dynamics significantly better than all stations together which increases the trust in the representatives of our data set. The bias became smaller for some subgroups (at the cost of lower correlation), but it remained notable in all cases. Furthermore, more sophisticated data averaging by using the EMIRAD antenna pattern to weight the average of the modeled in situ T_Bs nor the SMOS antenna pattern to estimate a weighted mean of EMIRAD data over the SMOS pixel did not im-

prove the results over applying simple data averaging. Thus, while some scaling effects are certainly inherent in the data comparison, we believe that their contributions are of subordinate relevance to explain the deviances between SMOS and the in situ data.

The severe RFI contaminations reported for many sites constitute a further potential error source. In that case, the source of the biases would already be inherent in the corresponding L1 data rather than being caused somewhere within the retrieval. Beside the Danish Cal/Val site, the significant dry bias in soil moisture has also consistently been reported for other areas known to be heavily RFI-contaminated, such as the sites in Southern and Northern Germany. In our case the strong impact of RFI on data quality was demonstrated by the filtering of data which was independently detected as RFI. It significantly improved the agreement in the dynamics, while the significant dry bias persisted over the Danish site. Permanent low energy RFI sources that constantly superimpose the naturally emitted signal, but cannot clearly be identified individually could be a possible cause. This is suggested by *Montzka et al.* (Accepted) in case of the Northern German site, and would coincide with the fact that no such significant dry bias is detected at RFI 'free' sites, such as West-Africa or the U.S. On the contrary, the dry bias is also observed in Australia where no heavy RFI impacts are expected. There, a presumption is that the SMOS retrieval is struggling with the extremely dry soils. Again, then it is inexplicable why the phenomenon is not likewise observed over the dry sites in Western Africa. At the Danish Cal/Val site the short campaign observation window accompanied by small temporal variability in soil moisture conditions as well as heavy RFI disturbances limited the extent of possible validation work at the brightness temperature level. Furthermore, model runs over longer time frames are confronted with large uncertainties inherent in the parameter settings. This renders this issue difficult to be tackled and requires more work to clarify the picture at the 1C level.

Finally, inaccuracies in the SMOS retrieval algorithm and related input could cause errors in the retrieved data products. As the retrieval is only based on the predominant land cover fraction while default contributions are assigned for the remaining fractions, it stands to reason that the overestimation of the initial soil moisture guess (ECMWF) could introduce bias in the retrieval. However, a sensitivity study by *Jackson et al.* (Accepted) showed the same retrieval results when the initial estimates were varied between 0 and 0.6 m^3/m^3. Likewise, *Al Bitar et al.* (Accepted) did not see a change in the bias between DGG nodes of significantly differing forest fractions with wetter conditions at the cost of the low vegetation fraction. Thus, a contribution to the retrieval offset is not expected.

There is a chance that the discrepancies between retrieved soil moisture/τ_{NAD} and in situ data, respectively, are interlinked as they are simultaneously retrieved by an optimization approach. If they were correlated, then the observed overestimation of the vegetation optical depth could lead to underestimation in soil moisture. Indeed, over one U.S. watershed *Jackson et al.* (Accepted) found correspondence in the dynamic of SMOS retrieved soil moisture and τ_{NAD} along with a dry bias of the former. However, this particular watershed is situated in a mountainous area with topographical effects and very dry conditions. For the other watersheds they could not detect the same linkage between the retrieved parameters.

The H_R roughness parameter is consistently set to a value way below the values reported from the Cal/Val studies including the Danish site for all individual land cover types. Spatial scale dependency of H_R was brought up as possible explanation for the lower SMOS values, as surfaces could appear significantly less rough from the large-distance perspective from space. Instead, *Jackson et al.* (Accepted) suggest that the too low H_R could compensate the

Table 7.4.: Summary of validation results for SMOS L1C, L2 initial and retrieved data in comparison with in situ data: T_B, soil moisture, real part of dielectric constant, surface temperature, τ_{NAD}, H_R, N_{RH}/N_{RV}, soil properties, dielectric mixing model, and land cover fractions. Potential error sources are depicted in bold, cases with short comparison period in italic letters.

	SMOS L1C	SMOS L2 inital	SMOS L2 retrieved
T_B	***offset, large uncertainty, scale effects?***		
Soil moisture		clear trend, too high	clear trend, too low
Real dielectric constant			clear trend, too low
Surface temparature		clear trend, same range	
τ_{NAD}		*clear trend, same range*	***trend, too high, noisy***
H_R		**too low or f(scale)?**	
N_{RH}/N_{RV}		0/-1 better 2/0	
Land cover fractions		in accord with CORINE2000	
Soil properties		**sand%/bulk density too low, clay% too high**	
Dielectric mixing model		***Mironov better Dobson (2x2 km scale)***	

high τ_{NAD} values, and lead to low soil moisture. However, the soil moisture dry bias which is variable from one validation site to the other can probably not be explained by this constant parameter alone. In this context also the N_{RH}/N_{RV} roughness parameter pair should be mentioned, for which a combination of 0/-1 instead of the SMOS default 2/0 increased the agreement between modeled in situ and EMIRAD T_Bs. The complex interactions between these parameters accompanied by their non-linear behavior over spatial and temporal scales constitute severe challenges. Furthermore, our determined values currently compensate for the not considered impacts of the organic layer at the Danish site. Thus, the behavior of the parameters themselves as well as the role of the organic substrate clearly need further attention.

While the global surface temperature and land cover products used in the SMOS retrieval algorithm seem to be in good agreement with in situ data and regional information, respectively, the soil properties as well as the dielectric mixing model applied in the SMOS processor have to be considered as potential error sources. Replacing the Dobson with the Mironov dielectric mixing model is a good candidate for improvement as we obtained better agreement at the patch-scale. Likewise, the substitution of the soil property grids by local information could lead to advancement.

7.6. Conclusions/Outlook

Since launch, SMOS has been acquiring soil moisture and vegetation optical thickness data which is currently subject to validation with in situ measurements across a range of climatic regions. The objective of this article was to compile previous validation results as well as present more in-depth analysis from the Danish validation site, covering SMOS pixel 2002029 in the Skjern River Catchment. In addition to retrieved parameters, the most sensitive parameters input to the SMOS retrieval algorithm were studied.

The worldwide more or less consistent SMOS validation findings are likewise encountered at the Danish site. The retrieved soil moisture data is promising as it well-captures the precipitation dynamics. However, the retrieved SMOS soil moisture exhibits larger amplitudes and shows a significant dry bias compared to in situ data. The retrieved SMOS vegetation

optical depth seems to overestimate true conditions and is accompanied by too high day to day variability to be explained by vegetation changes, as well as a lack of seasonal trend.

Several possible error sources for the observed deviations are currently under discussion, and it is probable that their respective contributions depend on the prevailing environmental conditions and the measurement setups of the individual Cal/Val sites.

At the Danish site the most likely error sources were determined as the following:

- An applied SMOS data filter using two criteria from the L2 product ($X\_SWATH < 10000$ and $CHI2\_P > 0.5$) turned out to be in good agreement with an RFI detection scheme based on L1A data. This indicates that strong RFI contamination was eliminated prior to data comparison. The filtering improved the R^2 between retrieved soil moisture and the in situ network average from 0.49 to 0.61, while the bias did not change significantly (from -0.092 to -0.087 m^3/m^3). The remaining bias could be caused by RFI from permanent low energy sources still present in the data, suggesting that the error is already inherent in the L1C data.

- There is a chance that the high retrieved τ_{NAD} and the low retrieved soil moisture are linked. A further possibility is compensation of the high τ_{NAD} for the H_R roughness parameter, which could cause low soil moisture values. H_R was found to be significantly lower in the SMOS retrieval than estimated in situ within the studied SMOS pixel 2002029. Furthermore, up to this point, only in situ data from the mineral soils was considered in our validation activities, resulting also in compensation of the τ_{NAD} and H_R parameters for this significantly wetter substrate.

- Comparison between average in situ soil properties with the SMOS FAO/ISLSCP data sets for DGG node 2002029 revealed clear differences with average SMOS sand fraction and bulk density being about 18% and 0.35 g/cm^3 lower, while the clay fraction being about 8% higher. Furthermore, the Mironov dielectric mixing model outperformed the Dobson model in a small-scale comparison.

- With respect to the larger amplitudes in the retrieved SMOS soil moisture data, different measurement depths between in situ sensors and SMOS are currently the most plausible explanation.

The unsolved RFI issues as well as the complex interactions between SMOS algorithm parameters accompanied by non-linear behavior over spatial and temporal scales constitute notable challenges to be mastered and more work is needed to enhance clarification. Further investigations at the Danish SMOS Cal/Val site will concentrate on investigations of the SMOS L1C - L2 data relation over longer time frames as well as site-specific adjustments in the SMOS processor. Furthermore, the potential differences in sampling depth and the role of the organic matter will be studied.

Acknowledgments The project is funded by the Villum Foundation and the Technical University of Denmark. Special thank goes to the SMOS team at and Jean-Pierre Wigneron for providing model codes as well as constructive discussions.

Part III.

Conclusions and Perspectives

8. Discussion and Conclusions

The Soil Moisture and Ocean Salinity (SMOS) satellite with a passive L-band microwave radiometer is dedicated to global surface soil moisture monitoring at high temporal resolution, which is important for water management and climate predictions. Beside soil moisture, vegetation optical thickness τ_{NAD} is retrieved (L2 product) from the measured brightness temperatures (L1C product). The SMOS data products are currently subject to validation with in situ data across a range of climatic regions.

In this context, the overall objective of this dissertation was SMOS validation in the Skjern River Catchment, covering one SMOS DDG node (2002029) and the surrounding pixel of 44 km in diameter. A first goal was the acquisition of the required in situ data, including (1) the design and establishment of a soil moisture and temperature network, and (2) the planning and realization of an airborne campaign with the L-band radiometer EMIRAD-2 and concurrent ground measurements of soil moisture and auxiliary parameters. The second goal was then the comparison of the collected data with measured SMOS L1C brightness temperatures and retrieved L2 soil moisture and vegetation optical thickness. This also included investigations on the most sensitive parameters input to the retrieval algorithm in order to identify potential sources for inaccuracies inherent in the final data products.

From this dissertation one conference proceeding and three journal papers emanated. The most important findings shall now be discussed and final conclusions drawn thereupon. Furthermore, an outlook on future work will be given.

8.1. Data acquisition

8.1.1. Soil moisture and temperature network

As soil moisture is highly variable across spatial scales and soil moisture networks often face constraints of either limited network-density or spatial extent, the identification of spatially representative locations for the individual network stations is a crucial issue. For this reason, the network in the Skjern River Catchment was carefully planned under consideration of the SMOS retrieval concept and based on analysis of the prevailing environmental conditions within the studied SMOS pixel. The stations were distributed according to respective fractions of land cover and soil types as well as aligned with the long-term precipitation gradient. Using this approach, it was anticipated that a priori the likelihood of obtaining a representative large-scale in situ soil moisture average for comparison with SMOS data was strongly enhanced.

The theoretical network design could be implemented without considerable reallocations. Analysis of the collected network data showed that soil moisture generally follows the precipitation trend. Furthermore, soil moisture and temperature patterns were relatable to the respective land cover and soil conditions. The high soil moisture variability throughout the stations seems to be a strong function of texture/structure while to a less extent influenced

by land cover. At the same time the variability in soil temperature is less pronounced and merely a function of the latter. Regional differences in surface soil moisture, temperature and precipitation between the north-east and south-west turned out to be small. After these data checks, we considered the network to operate according to expectations and to be suitable for validation of SMOS data.

8.1.2. Airborne campaign

Airborne campaigns offer the advantage of bridging the large spatial scale difference between point-like in situ measurements on the ground and the large SMOS footprint stepwise. Furthermore, the airborne and satellite data can be compared at brightness temperature level excluding uncertainties inherent in the model-derived soil moisture product. The chosen strategy in the Skjern River Catchment included (1) densely spaced in situ measurements within selected patches corresponding to the approximate footprint size of the airborne sensor (EMIRAD-2), and (2) maximum possible coverage of the studied SMOS pixel with the airborne data. Again, the prevailing land cover conditions were taken into account in the choice of the campaign sampling patches.

A preliminary assessment of the campaign data set revealed concordance of the encountered weather and environmental conditions with the acquired in situ and airborne measurements: constantly small rain events occurred before and during the two-week campaign window, leading to low temporal soil moisture variability throughout the observation period. This is well-reflected in the in situ soil moisture measurements as well as in the corresponding EMIRAD brightness temperatures. The spatial variability of the moisture content was generally high for all investigated land cover types and campaign dates. In contrast, the spatial variability of brightness temperatures at the airborne scale within the SMOS pixel was comparably low. In case of natural land covers (heath and forest), the thick moss/organic layers clearly exhibited significantly higher moisture contents than the underlying mineral soils, as well as the highest spatial and temporal variability. The observed vegetation growth was recorded in the increasing vegetation water content estimates between the two sampling days. This first data inspection consolidated our trust in the reliability of the data set for SMOS validation.

8.2. SMOS Validation

In the following, results from the SMOS validation in the Skjern River Catchment are presented. They are generally in good agreement with the worldwide more or less consistent findings (*Kontu et al.*, 2010; *Rüdiger et al.*, 2011b; *Dall'Amico et al.*, Accepted; *Jackson et al.*, Accepted; *Montzka et al.*, Accepted; *Schlenz et al.*, Accepted; *Al Bitar et al.*, Accepted; *Leroux et al.*, Submitted; *Gruhier et al.*, Submitted).

8.2.1. Level 1C Data

The stepwise comparison of brightness temperatures from in situ (point) via airborne to SMOS scale turned out to be successful. The uncertainty in the modeled T_Bs from the campaign soil moisture sampling was very high (5-20 K) when the most sensitive model parameters were varied within their most likely value ranges. However, for each land cover

class a combination of parameters could be selected to bring modeled and EMIRAD data in good agreement over all campaign days, both polarizations and 0 and 40° incidence angles, respectively. Thereby, replacing the Dobson dielectric mixing model (currently used in the SMOS retrieval) with the Mironov model decreased the overall RMSE from 11.5 K to 3.8 K. This is meaningful given the encountered highly sandy conditions in the Skjern River Catchment along with the fact that the Mironov model is validated for soil conditions up to pure quartz sand, while Dobson only for sand fractions up to 50%. Furthermore, considering only in situ data from the mineral soils in the T_B-modeling, resulted in compensation of the τ_{NAD} and H_R parameters for this significantly wetter substrate in case of sampling locations with natural vegetation (heath and forest patches).

EMIRAD data averaged at SMOS scale and corresponding SMOS T_Bs were also in the same range with a positive offset of the airborne data (mean RMSE=9.7 K). However, the short campaign period together with strong RFI contamination limited this comparison to one day (May 2).

8.2.2. Level 2 Data

The retrieved soil moisture data is promising as it well-captures the precipitation dynamics. However, the soil moisture dynamics observed by SMOS seem to exhibit larger amplitudes, and in many regions show a significant dry bias compared to the in situ data. Meanwhile, in relation to the latter the first soil moisture guess (ECMWF forecast) used to initialize the retrieval is constantly wetter. Over the entire year 2010, the comparison between SMOS initial/retrieved soil moisture of DGG node 2002029 with the average 0-5 cm network data revealed RMSE of 0.061/0.094 m^3/m^3, bias (average residuals from expected value) of 0.057/-0.087 m^3/m^3, and R^2 of 0.67/0.61, respectively. The corresponding comparison of the dielectric constant's real part (direct sensor output) network average and the SMOS dielectric constant's real part derived from a non cardioid model revealed RMSE, bias and R^2 values of 3.5 F/m, -2.5 F/m and 0.62. The SMOS dielectric constant is computed from retrieved soil moisture by means of the Dobson model. This together with the fact that the R^2s is equal to the one of the soil moisture comparison implies that at both comparison levels the uncertainty is consistent and remains on either the network or the SMOS data side.

The retrieved SMOS vegetation optical depth generally seems to overestimate true conditions and is accompanied by too high day to day variability to be explained by vegetation changes, as well as a lack of seasonal trend. This was confirmed at DGG node 2002029, where for a period of a month spanning around the campaign window, the retrieved SMOS τ_{NAD} was found to be very noisy from observation to observation, and to lie in the order of the τ_{NAD} on average used for the modeling of the forest campaign data. This value is expected to be too high as approximately 85% of the SMOS pixel is covered with low vegetation. Meanwhile, the initial SMOS τ_{NAD} was in good agreement with the τ_{NAD} on average used for the modeling of the agriculture campaign data. This is meaningful as the retrieval was based on the low vegetation land cover class.

Numerous factors come into consideration to explain the observed deviations. Under dis-

cussion have been (1) inacurracies in the in situ measurements, (2) a mismatch between sampling depth of conventional soil moisture sensors and the depth contributing to L-band soil emission, (3) scale effects due to the large disparity in spatial scale between the SMOS and in situ measurements, (4) RFI contamination, and (5) inaccuracies in the SMOS retrieval algorithm and related input. Depending on prevailing environmental conditions and measurement setups, the respective contributions of these potential error sources must be variable for the different Cal/Val sites. In the following, they are addressed individually in the context of the results from the Danish validation activities carried out in the scope of this dissertation.

Quality of in situ measurements

Preliminary data inspection of both the collected network and campaign data as described in Section 8.1 gave confidence that they both constitute reliable data sets for SMOS validation. Furthermore, a study where the network data was split into subgroups based on soil texture, land cover and a composite of the prevailing land covers, revealed that none of these subgroups was able to explain the SMOS soil moisture data better than the overall network average. This clearly augments the probability of good representativeness of the network setup and proves the chosen design successful. Based on these findings together with the fact that our results are generally well in range with worldwide Cal/Val results, we do not believe that the major discrepancies between the SMOS products and our in situ data sets originate from pronounced faultiness of the latter.

Mismatch in sampling depth

The existence of a mismatch in sampling depth between conventional in situ soil moisture sensors ($\sim$5-7 cm) and the depth contributing to L-band soil emission ($<$ 5 cm), with increasing magnitude the wetter the conditions, is currently discussed within the SMOS validation community. The larger amplitudes in the temporal dynamic of the retrieved SMOS soil moisture are likely to be explicable as a result of faster and stronger response to wetting (precipitation) and drying (evaporation, infiltration) at shallower depth (e.g. *Jackson et al.*, Accepted; *Al Bitar et al.*, Accepted). This issue is to be investigated at the Danish Cal/Val site.

Scale effects

The high spatial soil moisture variability across scales can easily provoke biases when comparing point in situ measurements with large-scale SMOS data. This became apparent during the comparison with our campaign data set. The bias between SMOS and EMIRAD brightness temperatures averaged over the SMOS pixel was clearly reduced compared to the one observed for the corresponding modeled in situ data averaged over the pixel using land cover fractions as weights. While the latter originated from selected patches with limited extent, the airborne data covered a substantial larger area of the SMOS pixel. This clearly proves the usefulness of the airborne data with spatial resolution at intermediate scale to bridge spatial scales. Meanwhile, more sophisticated data averaging by using the EMIRAD antenna pattern to weight the average of the modeled in situ T_Bs or the SMOS antenna pattern to estimate a weighted mean of EMIRAD data over the SMOS pixel did not improve

the results over applying simple data averaging. Certainly, some scaling effects must be inherent in the data comparison. However, based on these findings, along with the fact that the soil moisture dry bias remained significant throughout the above-mentioned network subgroup study, we believe that scaling contributions are also of subordinate relevance to explain the deviances between SMOS and the in situ data.

RFI

An applied SMOS data filter using two criteria from the L2 soil moisture product, namely $X\_SWATH < 10000$ and $CHI2\_P > 0.5$, turned out to be in good agreement with an RFI detection scheme based on L1A data (*Anterrieu*, 2011). This indicates that strong RFI contamination was eliminated prior to data comparison, which indeed improved the R^2 between retrieved soil moisture and the in situ 0-5 cm network average substantially (from 0.49 to 0.61). However, at the same time, the bias did not change significantly (from -0.092 to -0.087 m^3/m^3). One possible explanation could be permanent low energy RFI pollution (soft RFI) still present in the data. This has been suggested by several SMOS Cal/Val members (e.g. *Montzka et al.*, Accepted; *Dall'Amico et al.*, Accepted) and would imply that the error causing the bias is already inherent in the L1C brightness temperature data. At the Danish Cal/Val site T_B comparison between SMOS and EMIRAD as well as modeled in situ data by means of the campaign and network data sets averaged over the SMOS pixel showed an ambivalent picture with higher and lower T_Bs of the two former and the latter, respectively. Unfortunately, the above-mentioned temporal constraints of the airborne campaign accompanied by high uncertainty in the network T_B modeling limited the extent of these investigations. This issue remains open for the time being.

Quality of the SMOS retrieval algorithm and related input

Finally, inaccuracies in the SMOS retrieval algorithm and related input could cause errors in the retrieved data products. By means of the campaign and network data sets, investigations on the most sensitive parameters input to the algorithm (soil moisture, soil temperature, soil texture and bulk density, land cover information, τ_{NAD}, H_R roughness parameter) as well as the applied dielectric mixing model to link between soil moisture and dielectric properties enabled the location of potential error sources to explain the dry bias while others could be mitigated:

- As the retrieval is only based on the predominant land cover fraction while default contributions are assigned for the remaining fractions, it stands to reason that the overestimation of the initial soil moisture guess (ECMWF) could introduce bias in the retrieval. However, sensitivity studies at other Cal/Val sites (*Jackson et al.*, Accepted; *Al Bitar et al.*, Accepted) have shown that a contribution to the retrieval offset is not expected.

- As pointed out by *Jackson et al.* (Accepted), there is a chance that the high retrieved τ_{NAD} (high vegetation water contribution), when used to initialize the consecutive retrieval, results in a low retrieved soil moisture content. Another possibility is compensation of the high SMOS τ_{NAD} for the H_R roughness parameter (describing the intensity of the roughness effects), which is significantly lower in the SMOS retrieval

algorithm (0.1-0.2) than what we estimated for any of the prevailing surface conditions within the studied SMOS pixel (0.58-1.17). This could again result in low retrieved soil moisture. A further discovered issue in this context is the N_{RH}/N_{RV} roughness parameter pair (allowing the modulation of the reflectivity as a function of the incidence angle for both polarizations). In the modeling of the campaign sampling data set for comparison with EMIRAD at the 2x2 km scale, a combination of 0/-1 instead of the SMOS default, 2/0, decreased the RMSE in the 40° H channel from 15.7 to 3.4 K. Finally, our determined values currently compensate for the not considered impacts of the organic layer at the Danish site. Thus, the behavior of the parameters themselves as well as the role of the organic substrate clearly need further attention.

- Comparison between average in situ soil properties with the FAO/ISLSCP data sets used in the SMOS retrieval algorithm for DGG node 2002029 revealed clear differences with average SMOS sand fraction and bulk density being about 18% and 0.35 g/cm^3 lower, while the clay fraction being about 8% higher. Furthermore, as was demonstrated at the 2x2 km scale, it is likely that the Dobson dielectric mixing model is not fully suited for the SMOS retrieval over the Danish site.

- The SMOS initial surface temperature (ECMWF forecast) is in good agreement with the average 0-5 cm network temperature (RMSE/bias/R^2 of 1.1 °C/-0.2 °C/0.97, respectively, over the year 2010), and thus not considered as substantial error source.

- Likewise, the FMO land cover fractions (ECOCLIMAP) used in the SMOS retrieval algorithm for DGG node 2002029 are in range with the corresponding fractions of the CORINE Land Cover Classification 2000. Thus, we do not believe that the major contribution to the deviations in the retrieved products is to be sought here.

8.3. Conclusions

Several valuable contributions to the validation of the SMOS retrieval algorithm and its associated products arise from the extensive work carried out in the scope of this dissertation:

- A method to design and implement an in situ network suitable for the validation of large-scale satellite products is presented and successfully applied. This can be supportive for the establishment of similar networks at other locations.

- The combination of two complementary data sets allowed for exhaustive validation over spatial and temporal scales: The temporally limited, but solid campaign data set of high spatial coverage and density throughout spatial scales was of high value for the site-specific determination of important model parameters used in the SMOS retrieval algorithm. Meanwhile, thanks to its spatially representative distribution, the long-term network data set of limited spatial density and extent proved to be of high value for the comparison over longer time scales, thus facilitating the assessment of temporal dynamics.

- Beside the comparison of retrieved data products, this comprehensive approach further offered the advantage of in-depth analysis of the most sensitive parameters in the

SMOS retrieval algorithm. This in turn enabled the localization of (1) mismatch in sampling depth of in situ sensors and L-band soil emission depth, (2) soft RFI and (3) inaccuracies in the retrieval algorithm, namely choice of the vegetation optical depth and the surface roughness parameters, soil properties and dielectric mixing model, to be the most likely error sources for the current discrepancies between the SMOS products and in situ data. Thereby, this work clearly guides to the most urgent issues to be addressed next. Beside the unsolved RFI issues, complex interactions between certain algorithm parameters accompanied by their non-linear behavior over spatial and temporal scales constitute severe challenges to be mastered.

- Another crucial issue disclosed by this work is the influence of the distinct organic layers (with high water storage capacities) present under natural vegetation throughout the Danish validation site and likewise existent across vast areas of the higher northern latitudes. The organic layer certainly needs further attention which can be tackled by means of the acquired (not yet analyzed) campaign data evolving from this dissertation.

The so far gained knowledge together with the established long-term monitoring network as well as the not yet fully utilized campaign data set from the Danish Cal/Val site can pursue to constitute beneficial input for the continuous improvement of SMOS data quality. At the same time, this work can be supportive for upcoming soil moisture space missions such as NASA's Soil Moisture Active and Passive SMAP, scheduled for launch in December 2012. Furthermore, knowing the caveats of the SMOS data at this stage, its use in regional and global modeling efforts for studies of water resources and climate can be initiated.

9. Perspectives

In the future it is planned to continue the validation work at the Danish validation site to deal with issues left open at the end of this dissertation:

- **Mismatch in sampling depth:** In the framework of HOBE a Soil-Vegetation-Atmosphere Transfer (SVAT) model will be set up and calibrated against the data of the individual network stations in the Skjern River Catchment. The model allows for the discretization of the soil surface layer into smaller depth intervals than resolvable by the in situ sensors. This will enable comparison of retrieved SMOS soil moisture with soil moisture modeled for shallower depths, in order to investigate the potential mismatch in sampling depth between ground and spaceborne sensors. This approach will be compared with a method developed by O. Merlin (Centre d'Etudes Spatiales de la Biosphere, CESBIO, personal communication) to correct the SMOS sensing depth according to the in situ sensor sampling depth. Once the SVAT model is calibrated for the prevailing environmental conditions, an attempt could also be made to model soil moisture over the entire SMOS pixel with a spatially complete pattern in order to study scaling issues.

- **RFI:** With respect to the unsolved (soft) RFI issues, it is planned to study the link between L1C and L2 data over longer time frames, as well as to continue collaboration with E. Anterrieu (Laboratoire Astrophysique de Toulouse - Tarbes, LATT) who is currently developing an RFI mitigation technique that also needs to be tested at level 2. Intense RFI research is also conducted at DTU Space substantially supporting the continuous progress on the clarification of this issue.

- **Quality of the SMOS retrieval algorithm and related input:** To study the inaccuracies inherent in the SMOS retrieval algorithm and its input, site-specific modifications in the SMOS L2 processor are planed. This includes the substitution of the Dobson dielectric model with the Mironov model, and the use of local estimates of soil properties, vegetation and roughness parameters. Furthermore, the processor could be run with the retrieval constrained to one parameter at a time.

- **Organic matter:** The role of the organic substrate on top of the mineral soils under natural vegetation (currently compensated by the τ_{NAD} and H_R parameters at the Danish site) will be addressed by means of the organic campaign data. An attempt will be made to calibrate the L-MEB model for this substrate and thus retrieve corresponding model parameters.

- **Impact of open water:** The validation activities can also be expanded to surrounding nodes to explore the impact of higher open water fractions.

References

Al Bitar, A., D. Leroux, Y. Kerr, O. Merlin, P. Richaume, A. Sahoo, and E. F. Wood (Accepted), Evaluation of SMOS soil moisture products over continental US using the SCAN/SNOTEL network, *IEEE Transactions on Geoscience and Remote Sensing*.

Albergel, C., et al. (2011), A first assessment of the SMOS data in southwestern France using in situ and airborne soil moisture estimates: the CAROLS airborne campaign, *Remote Sensing of Environment*, *115*, 2718–2728.

Albertz, J. (2001), *Einführung in die Fernerkundung*, Wissenschaftliche Buchgesellschaft, Darmstadt, Germany.

Anterrieu, E. (2011), On the detection and quantification of RFI in L1a signals provided by SMOS, *IEEE Transactions on Geoscience and Remote Sensing*, *49*(10), 3986–3992, digital Object Identifier : 10.1109/TGRS.2011.2136350.

Bardossy, A., and W. Lehmann (1998), Spatial distribution of soil moisture in a small catchment. Part 1: geostatistical analysis, *Journal of Hydrology*, *206*, 1–15.

Bengoa, B., M. Zapata, C. Cabeza, and M. Rodriguez (2010), SMOS level 2 processor and auxiliary data products specifications, *Tech. Rep. SO-TN-IDR-GS-0006, V5.3*, INDRA, Madrid.

Bircher, S., J. Balling, and N. Skou (2010), SMOS validation activities at different scales in the Skjern River Catchment, Western DK, in *ESA Living Planet Symposium*, edited by H. Lacoste-Francis, ESA, ESA communications, Bergen, Norway.

Bircher, S., J. E. Balling, N. Skou, and Y. Kerr (Accepted), Validation of SMOS brightness temperatures during the HOBE airborne campaign, Western Denmark, *IEEE Transactions on Geoscience and Remote Sensing*, doi:10.1109/TGRS.2011.2170177.

Bircher, S., N. Skou, K. H. Jensen, J. P. Walker, and L. Rasmussen (Submitted), A soil moisture and temperature network for SMOS validation in the Skjern River Catchment, Western Denmark, *Hydrology and Earth System Sciences*.

Bloeschl, G., and M. Sivapalan (1995), Scale issues in hydrological modelling: A review, *Hydrological Processes*, *9*, 251–290.

Bogena, H., M. Herbst, J. A. Huisman, U. Rosenbaum, A. Weuthen, and H. Veerecken (2010), Potential of wireless sensor networks for measuring soil water content variability, *Vadose Zone Journal*, *9*, 1002–1013.

Bornebusch, C., and K. Milthers (1935), Jordbundskort over Danmark, 1:500.000, Danmarks Geologiske Undersoegelse, 111:24.

Bosch, D., V. Lakshmi, T. Jackson, M. Choi, and J. Jacobs (2006), Large scale measurements of soil moisture for validation of remotely sensed data: Georgia soil moisture experiment of 2003, *Journal of Hydrology*, *323*, 120–137.

Bossard, M., J. Feranec, and J. Otahel (2000), CORINE land cover technical guide - Addendum 2000, *Tech. Rep. 40*, European Environmental Agency, Copenhagen.

Bot, A., and J. Benites (2005), The importance of soil organic matter. Key to drought-resistant soil and sustained food production, *FAO Soils Bulletin 80*, Food and Agriculture Organization of the United Nations (FAO), Rome, Italy.

Brocca, L., R. Morbidelli, F. Melone, and T. Moramarco (2007), Soil moisture spatial variability in experimental areas of Central Italy, *Journal of Hydrology*, *333*, 356–373.

Brocca, L., F. Melone, T. Moramarco, and R. Morbidelli (2010), Spatial-temporal variability of soil moisture and its estimation across scales, *Water Resources Research*, *46*, W02,516, doi:10.1029/2009WR008016.

Calvet, J.-C., N. Fritz, F. Froissard, D. Suquia, A. Petitpa, and B. Piguet (2007), In situ soil moisture observations for the Cal/Val of SMOS: the SMOSMANIA network, in *IEEE International Geoscience and Remote Sensing Symposium (IGARSS)*, pp. 1196–1199, Barcelona, Spain.

Cano, A., et al. (2010), The SMOS Mediterranean Ecosystem L-band characteristation EXperiment (MELBEX-I) over natural shrubs, *Remote Sensing of Environment*, *114*, 844–853.

Champagne, C., A. Berg, J. Belanger, H. McNairn, and R. de Jeu (2010), Evaluation of soil moisture derived from passive microwave remote sensing over agricultural sites in Canada using ground-based soil moisture monitoring networks, *International Journal of Remote Sensing*, *31*(14), 3669–3690.

Choudhury, B., T. Schmugge, A. Chang, and R. . Newton (1979), Effect of surface roughness on the microwave emission from soils, *Journal of Geophysical Research*, *84*, 5699–5706.

Coquet, Y., C. Coutadeur, C. Labat, P. Vachier, J. van Genuchten, M. T. annd Roger-Estrade, and J. Simunek (2005), Water and solute transport in a cultivated silt loam soil: 1. field observations, *Vadose Zone Journal*, *4*, 573–586.

Corwin, D. L., J. Hopmans, and G. H. de Rooij (2006), From field- to landscape-scale vadose zone processes: Scale issues, modeling, and monitoring, *Vadose Zone Journal*, *5*, 129–139.

Cosh, M., T. Jackson, R. Bindlish, and J. H. Prueger (2004), Watershed scale temporal and spatial stability of soil moisture and its role in validating satellite estimates, *Remote Sensing of Environment*, *92*, 427–435.

Crow, W. T., D. Ryu, and J. S. Famiglietti (2005), Upscaling of field-scale soil moisture measurements using distributed land surface modeling, *Advances in Water Resources*, *28*, 1–14.

Daganzo, E., et al. (2010), Characterisation of SMOS RF Interferences in the 1400-1427 MHz band as detected during the commissioning phase, in *OCOSS 2010*, Brest, France.

Dall'Amico, J. T., F. Schlenz, A. Loew, and W. Mauser (2010), SMOS soil moisture validation: Status at the Upper Danube Cal/Val site eight months after launch, in *IEEE International Geoscience and Remote Sensing Symposium (IGARSS)*, pp. 3801–3804, Honolulu, Hawaii, USA.

Dall'Amico, J. T., F. Schlenz, A. Loew, and W. Mauser (Accepted), First results of SMOS soil moisture validation in the Upper Danube Catchment, *IEEE Transactions on Geoscience and Remote Sensing*.

Danmarks Statistik, A., and H. Service (2009), Cultivated area by unit, region, crop and time in hectares for the region Midtjylland, verified June 10, 2009.

De Lannoy, G. J. M., P. R. Houser, N. E. C. Verhoest, V. R. N. Valentijn, and T. J. Gish (2007), Upscaling of point soil moisture measurements to field averages at the OPE test site, *Journal of Hydrology*, *343*, 1–11.

de Rosnay, P., C. Gruhier, F. Timouk, F. Baup, E. Mougin, P. Hiernaux, L. Kergoat, and V. LeDantec (2009), Multi-scale soil moisture measurements at the Gourma meso-scale site in Mali, *Journal of Hydrology*, *375*, 241–252.

de Rosnay, P., et al. (2008), The AMMA land surface model intercomparison experiment coupled to the Community Microwave Emission Model: ALMIP-MEM, *Technical Memorandum 565*, ECMWF, Reading, UK.

Decagon Devices, Inc. (2002), *ECH2O data collection system. Operator's manual for models Em50/Em50R*, Decagon Devices, Inc., 2365 NE Hopkins Court Pullman WA 99163 USA, version 6 ed.

Decagon Devices, Inc. (2008), *ECH2O soil moisture sensor. Operator's manual for model 5TE*, Decagon Devices, Inc., 2365 NE Hopkins Court Pullman WA 99163 USA, version 3 ed.

Delwart, S., C. Bouzinac, P. Wursteisen, M. Berger, M. Drinkwater, M. Martin-Neira, and H. Kerr, Yann (2008), SMOS validation and the COSMOS campaigns, *IEEE Transactions on Geoscience and Remote Sensing*, *46*(3), 695–704.

DGU (1945), Geologiske kort over Danmark, 1:100.000, D.G.U.

Dobson, M., F. Ulaby, M. Hallikainen, and M. El-Reyes (1985), Microwave dielectric behavior of wet soil - Part II: Dielectric mixing models, *IEEE Transactions on Geoscience and Remote Sensing*, *23*, 35–46.

Dorigo, W., et al. (2011), The International Soil Moisture Network: A data hosting facility for global in situ soil moisture measurements, *Hydrology and Earth System Sciences*, *15*, 1675–1698, doi:10.5194/hess-15-1675-2011.

EEA (2005), Corine land cover 2000 (CLC2000) 100 m - version 8/2005.

Elachi, C., and J. van Zyl (2006), *Introduction to the Physics and Techniques of Remote Sensing*, 2 ed., John Wiley and Sons, Inc., Hoboken, New Jersey, USA.

Entekhabi, D. (1995), Recent advances in land-atmosphere interaction research, *Reviews of Geophysics*, *33*(S1), 995–1004.

Entekhabi, D., et al. (2004), The Hydrosphere State (Hydros) Satellite Mission: An earth system pathfinder for global mapping of soil moisture and land freeze/thaw, *IEEE Transactions on Geoscience and Remote Sensing*, *42*(10).

Entin, J. K., A. Robock, K. Y. Vinnikov, S. E. Hollinger, S. Liu, and A. Namkhai (2000), Temporal and spatial scales of observed soil moisture variations in the extratropics, *Journal of Geophysical Research*, *105*(D9), 11,865–11,877.

Escorihuela, M., Y. Kerr, P. de Rosnay, J.-P. Wigneron, J.-C. Calvet, and F. Lemaître (2007), A simple model of the bare soil microwave emission at L-band, *IEEE Transactions on Geoscience and Remote Sensing*, *45*(7), 1978–1987.

Escorihuela, M., A. Chanzy, J. Wigneron, and Y. Kerr (2010), Effective soil moisture sampling depth of L-band radiometry: A case study, *Remote Sensing of Environment*, *114*, 995–1001.

Famiglietti, J., J. Devereaux, C. Laymon, T. Tsegaye, P. Houser, T. Jackson, S. Graham, M. Rodell, and P. van Oevelen (1999), Ground-based investigations of soil moisture variability within remote sensing footprints during the Southern Great Plains 1997 (SGP97) Hydrology Experiment, *Water Resources Research*, *35*(6), 1839–1851.

Famiglietti, J. S., J. W. Rudnicki, and M. Rodell (1998), Variability in surface moisture content along a hillslope transect: Rattlesnake Hill, Texas, *Journal of Hydrology*, *210*, 259–281.

Famiglietti, J. S., D. Ryu, A. A. Berg, M. Rodell, and T. J. Jackson (2008), Field observations of soil moisture variability across scales, *Water Resources Research*, *44*, W01,423, doi:10.1029/2006WR005804.

FAO-Aquastat (2003), Review of world water resources by country, *Water Reports, 23*, Rome.

Ferrazzoli, P., L. Guerriero, and J.-P. Wigneron (2002), Simulating L-band emission of forests in view of future satellite applications, *IEEE Transactions on Geoscience and Remote Sensing*, *40*(12), 2700–2708.

Friesen, J., C. Rodgers, P. G. Oguntunde, J. M. H. Hendrickx, and N. van de Giesen (2008), Hydrotope-based protocol to determine average soil moisture over large areas for satellite calibration and validation with results from an observation campaign in the Volta Basin, West Africa, *IEEE Transactions on Geoscience and Remote Sensing*, *46*(7), 1995–2004.

FVM (2005), Information on crops on field level from the Ministry of Food, Fisheries and Agriculture (FVM) regarding application for single-payments in 2005, accessed

via the research-based agricultural registry at the Faculty of Agriculture, Aarhus University.

Gasiewski, A. J. (1993), Calibration and applications of polarization-correlating radiometers, *IEEE Transactions on Microwave Theory and Techniques*, *41*(5), 767–773.

Grant, J., K. Saleh-Contell, J.-P. Wigneron, M. Guglielmetti, Y. Kerr, M. Schwank, N. Skou, and V. de Griend A. (2008), Calibration of the L-MEB model over a coniferous and a deciduous forest, *IEEE Transactions on Geoscience and Remote Sensing*, *46*(3), 808–818.

Grayson, R. B., A. W. Western, F. H. S. Chiew, and G. Bloeschl (1997), Preffered states in spatial soil moisture patterns: Local and non-local controls, *Water Resources Research*, *33*, 2897–2908.

Greve, M. H., M. B. Greve, P. Bøcher, T. Balstrøm, H. Breuning-Madsen, and L. Krogh (2007), Generating a Danish raster-based topsoil property map combining choropleth maps and point information, *Danish Journal of Geography*, *107*(2), 1–12.

Gruhier, C., T. Pellarin, P. de Rosnay, and Y. Kerr (Submitted), SMOS soil moisture product evaluation over West-Africa at local and regional scale, *Remote Sensing of Environment*.

Helvey, J. D., and J. H. Patric (1965), Canopy and litter interception of rainfall by hardwoods of eastern United States, *Water Resources Research*, *1*(2), 193–206.

Hillel, D. (1998), *Environmental Soil Physics*, 771 pp., Academic Press, San Diego, CA, USA.

Hu, Z., S. Islam, and Y. Cheng (1997), Statistical characterization of remotely sensed soil moisture images, *Remote Sensing of Environment*, *61*, 310–318.

IPCC (2007), Climate change 2007: The scientific basis. Contribution of Working Group I to the Fourth Assessment Report of the Intergovernmental Panel on Climate Change, *Tech. Rep. 4*, Intergovernmental Panel on Climate Change (IPCC), Cambridge University Press, New York, Solomon, S. and Qin, D. and Manning, M. and Chen, Z. and Marquis, M. and Averyt, K. B. and Tignor, M. and Miller, H. L. (eds.).

ISSS (1929), Minutes of the first Commission Meetings, in *Proceedings of the International Society of Soil Science*, vol. 4, pp. 215–220, International Society of Soil Science (ISSS), Washington, USA.

Jackson, T., and T. Schmugge (1991), Vegetation effects on the microwave emission of soils, *Remote Sensing of Environment*, *36*, 203–212.

Jackson, T., D. Le Vine, C. Swift, T. Schmugge, and F. Schiebe (1995), Large area mapping of soil moisture using the ESTAR passive microwave radiometer in Washita'92, *Remote Sensing of Environment*, *53*, 27–37.

Jackson, T., D. Le Vine, A. Hsu, A. Oldak, P. Starks, C. Swift, J. Isham, and M. Haken (1999), Soil moisture mapping at regional scales using microwave radiometry: The Southern Great Plains Hydrology Experiment, *IEEE Transactions on Geoscience and Remote Sensing*, *37*(5).

Jackson, T. J., J. Schmugge, and E. T. Engman (1996), Remote sensing applications to hydrology: Soil moisture, *Hydrological Sciences Journal*, *41*(4), 517–529.

Jackson, T. J., M. H. Cosh, R. Bindlish, P. J. Starks, D. D. Bosch, M. Seyfried, D. C. Goodrich, M. S. Moran, and J. Du (2010), Validation of Advanced Microwave Scanning Radiometer soil moisture products, *IEEE Transactions on Geoscience and Remote Sensing*, *48*(12), 4256–4272.

Jackson, T. J., et al. (Accepted), Validation of Soil Moisture and Ocean Salinity (SMOS) soil moisture over watershed networks in the U.S., *IEEE Transactions on Geoscience and Remote Sensing*.

Jarvis, A., H. Reuter, A. Nelson, and E. Guevara (2008), Hole-filled seamless SRTM, data V4.

Jensen, J. R. (2007), *Remote Sensing of the Environment: An Earth Resource Perspective*, 2 ed., Pearson Education, Inc., Upper Saddle River, NJ, USA.

Jensen, K., and T. Illangasekare (2011), HOBE: A hydrological observatory, *Vadose Zone Journal*, *10*, 1–7.

Kainulainen, J., et al. (2010), SMOS calibration and validation activities with airborne interferometric radiometer HUT-2D during spring 2010, in *Geoscience and Remote Sensing Symposium (IGARSS)*, pp. 702–705, Honolulu, HI, USA.

Kerr, Y. (2007), Soil moisture from space: Where are we?, *Hydrogeology Journal*, *15*, 117–120.

Kerr, Y., P. Waldteufel, J.-P. Wigneron, J.-M. Martinuzzi, J. Font, and M. Berger (2001), Soil moisture retrieval from space: The Soil Moisture and Ocean Salinity (SMOS) mission, *IEEE Transactions on Geoscience and Remote Sensing*, *39*(8), 1729–1735, doi:10.1109/36.942551.

Kerr, Y., P. Waldteufel, P. Richaume, P. Davenport, P. Ferrazzoli, and J.-P. Wigneron (2011), SMOS Level 2 Processor. Soil Moisture Algorithm Theoretical Basis Document (ATBD), *Tech. Rep. SO-TN-ARR-L2PP-0037, V3.4*, CBSA, UoR, TV and INRA, Toulouse.

Kerr, Y., et al. (Submitted), The SMOS soil moisture retrieval algorithm, *IEEE Transactions on Geoscience and Remote Sensing*.

Kerr, Y. H. (1996), Optimal choice for MIRAS frequencies scientific requirements, *MMS MIRAS Project Report CCM31996*, CESBIO, Toulouse, France.

Kerr, Y. H., et al. (2010), The SMOS mission: New tool for monitoring key elements of the global water cycle, *Proceedings of the IEEE*, *98*(5), 666–687.

Kim, G., and A. Barros (2002), Space-time characterization of soil moisture from passive microwave remotely sensed imagery and ancillary data, *Remote Sensing of Environment*, *81*, 393–403.

Kizito, F., C. S. Campbell, G. S. Campbell, D. Cobos, B. Teare, B. Carter, and J. Hopmans (2008), Frequency, electrical conductivity and temperature analysis of a low-cost capacitance soil moisture sensor, *Journal of Hydrology*, *352*, 367–378.

Kontu, A., J. Lemmetyinen, J. Pulliainen, K. Rautiainen, J. Kainulainen, and J. Seppaenen (2010), L-band measurements of boreal soil, in *IEEE International Geoscience and Remote Sensing Symposium (IGARSS)*, Digital Object Identifier: 10.1109/IGARSS.2010.5654116, pp. 706–709.

Kraus, K. (1988), *Fernerkundung - Band1: Physikalische Grundlagen und Aufnahmetechniken*, vol. 1, Duemmler, Bonn, Germany.

Krauss, L., C. Hauck, and C. Kottmeier (2010), Spatio-temporal soil moisture variability in Southwest Germany observed with a new monitoring network within the COPS domain, *Meteorologische Zeitschrift*, *19*(6), 523–537.

Lagerloef, G., et al. (2008), The Aquarius/SAC-D mission, *Oceanography*, *21*(1).

Laymon, C., W. Crosson, T. Jackson, A. Manu, and T. Tsegaye (2001), Ground-based passive microwave remote sensing observations of soil moisture at S-band and L-band with insight into measurement accuracy, *IEEE Transactions on Geoscience and Remote Sensing*, *39*, 1844–1858.

Leroux, D. J., Y. H. Kerr, A. Al Bitar, C. Gruhier, R. Bindlish, T. J. Jackson, B. Berthelot, and G. Portet (Submitted), Comparison between SMOS and other satellite and model forecast products, *Remote Sensing of Environment*.

Loeffler, E. (1985), *Geographie und Fernerkundung*, Teubner-Studienbuecher, Stuttgart, Germany.

Martinez-Fernandez, J., and A. Ceballos (2003), Temporal stability of soil moisture in a large-field experiment in Spain, *Soil Science Society of America*, *67*, 1647–1656.

Masson, V., J. Champeaux, F. Chauvin, C. Meriguet, and R. Lacaze (2003), A global database of land surface parameters at 1 km resolution in meterological and climate models, *Journal of Climate*, *16*(9), 1261–1282.

Merlin, O., J. Walker, R. Panciera, M. Escorihuela, and T. Jackson (2009), Assessing the SMOS soil moisture retrieval parameters with high-resolution NAFE'06 data, *Geoscience and Remote Sensing Letters*, *6*(4), 635–639.

Merlin, O., et al. (2008), The NAFE'06 data set: Towards soil moisture retrieval at intermediate resolution, *Advances in Water Resources Research*, *31*, 1444–1455.

Mialon, A., J.-P. Wigneron, P. de Rosnay, M. Escorihuela, and Y. Kerr (Accepted), Evaluating L-MEB from long term microwave measurements over a rough field, SMOSREX 2006, *IEEE Transactions on Geoscience and Remote Sensing*.

Miller, D. H. (1977), *Water at the Surface of the Earth. An Introduction to Ecosystem Hydrodynamics*, 2 ed., 557 pp., Academic Press, New York, USA.

Mironov, V., M. Dobson, V. Kaupp, S. Komarov, and V. Kleshchenko (2004), Generalized refractive mixing dielectric model for moist soils, *IEEE Transactions on Geoscience and Remote Sensing*, *42*(4), 773–785.

Mo, T., and T. Schmugge (1987), A parameterization of the effect of surface roughness on microwave emission, *IEEE Transactions on Geoscience and Remote Sensing*, *GRS-25*(4), 481–486.

Mo, T., B. Choudhury, T. Schmugge, and T. Jackson (1982), A model for microwave emission from vegetation covered fields, *Journal of Geophysical Research*, *11*(11), 229–237.

Mohanty, B. P., and T. H. Skaggs (2001), Spatio-temporal evolution and timestable characteristics of soil moisture within remote sensing footprints with varying soil, slope, and vegetation, *Advances in Water Resources*, *24*, 1051–1067.

Mohanty, B. P., T. H. Skaggs, and J. S. Famiglietti (2000), Analysis and mapping of field-scale soil moisture variability using high-resolution, ground-based data during the Southern Great Plains 1997 (SGP97) Hydrology Experiment, *Water Resources Research*, *36*(4), 1023–1031.

Montzka, C., et al. (Accepted), Brightness temperature validation at different scales during the SMOS validation campaign in the Rur and Erft Catchments, Germany, *IEEE Transactions on Geoscience and Remote Sensing*.

Naeimi, V., K. Scipal, Z. Bartalis, S. Hasenauer, and W. Wagner (2009), An improved soil moisture retrieval algorithm for ERS and MeTop scatterometer observations, *IEEE Transactions on Geoscience and Remote Sensing*, *47*, 1999–2013.

Njoku, E. G., T. J. Jackson, V. Lakshmi, T. K. Chan, and S. V. Nghiem (2003), Soil moisture retrieval from AMSR-E, *IEEE Transactions on Geoscience and Remote Sensing*, *41*, 215–229.

Owe, M., R. A. De Jeu, and J. P. Walker (2001), A methodology for surface soil moisture and vegetation optical depth retrieval using the microwave polarization difference index, *IEEE Transactions on Geoscience and Remote Sensing*, *39*, 1643–1654.

Panciera, R., J. Walker, J. Kalma, E. Kim, J. Hacker, O. Merlin, M. Berger, and N. Skou (2008), The NAFE'05/COSMOS data set: Toward SMOS soil moisture retrieval, downscaling, and assimilation, *IEEE Transactions on Geoscience and Remote Sensing*, *46*(3), 736–745.

Panciera, R., J. Walker, and O. Merlin (2009a), Improved understanding of soil surface roughness parameterization for L-band passive microwave soil moisture retrieval, *IEEE Geoscience and Remote Sensing Letters*, *6*(4), 625–629.

Panciera, R., J. Walker, J. Kalma, E. Kim, K. Saleh, and J.-P. Wigneron (2009b), Evaluation of the SMOS L-MEB passive microwave soil moisture retrieval algorithm, *Remote Sensing of Environment*, *113*, 435–444.

Pardé, M., J.-P. Wigneron, P. Waldteufel, Y. Kerr, A. Chanzy, S. S. Søbjærg, and N. Skou (2004), N-parameter retrievals from L-band microwave observations acquired over a variety of crop fields, *IEEE Transactions on Geoscience and Remote Sensing*, *42*(6), 1168–1178.

Peischl, S., J. P. Walker, C. Rüdiger, Y. Nan, Y. Kerr, and E. Kim (In Prep.), The AACES field experiments: SMOS calibration and validation across the Murrumbidgee River Catchment.

Peischl, S., et al. (2009), Towards validation of SMOS using airborne and ground data over the Murrumbidge Catchment, in *18th World IMACS/MODSIM Congress*, Cairns, Australia.

Pellarin, T., et al. (2003), Two-year global simulation of L-band brightness temperatures over land, *IEEE Transactions on Geoscience and Remote Sensing*, *41*(9), 2135–2139.

Peplinski, N., F. Ulaby, and M. Dobson (1995), Dielectric properties of soils in the 0.3-1.3-GHz range, *IEEE Transactions on Geoscience and Remote Sensing*, *33*(3), 803–807.

Peters-Lidard, C. D., F. Pan, and E. F. Wood (2001), A re-examination of modeled and measured soil moisture spatial variability and its implication for land surface modeling, *Advances in Water Resources*, *24*, 1069–1083.

Piles, M., D. Entekhabi, and A. Camps (2009), A change detection algorithm for retrieving high-resolution soil moisture from SMAP radar and radiometer observations, *IEEE Transactions on Geoscience and Remote Sensing*, *47*(12), 4125–4131.

Plauborg, F. L., J. Refsgaard, H. Henriksen, G. Blicher-Mathiesen, and C. Kern-Hansen (2003), Problemer med vandbalancen på mark- og oplandsskala, *Vand og Jord*, *10*(2), 59–61.

Prigent, C., F. Aires, W. B. Rossow, and A. Robock (2005), Sensitivity of satellite microwave and infrared observations to soil moisture at a global scale: Relationship of satellite observations to in situ soil moisture measurements, *Journal of Geophysical Research*, *110*(D07110), 1–15.

Raju, S., A. Chanzy, J.-P. Wigneron, J.-C. Calvet, Y. Kerr, and L. Laguerre (1995), Soil moisture and temperature profile effects on microwave emission at low frequencies, *Remote Sensing of Enviornment*, *54*(2), 85–97.

Rüdiger, C., J. P. Walker, and Y. H. Kerr (2011a), On the airborne spatial coverage requirement for microwave satellite validation, *IEEE Geoscience and Remote Sensing Letters*, *8*(4), 824–828.

Rüdiger, C., J. P. Walker, Y. H. Kerr, A. Mialon, O. Merlin, and E. J. Kim (2011b), Validation of the Level 1c and Level 2 SMOS products with airborne and ground-based observations, in *International Congress on Modelling and Simulation (MODSIM)*, Perth, Australia.

Reichle, R., and R. Koster (2004), Bias reduction in short records of satellite soil moisture, *Geophysical Research Letters*, *31*(L19501), doi:10.1029/2004GL.020938.

Robinson, D. A., C. S. Campbell, J. W. Hopmans, B. K. Hornbuckle, S. B. Jones, R. Knight, F. Ogden, J. Selker, and O. Wendroth (2008), Soil moisture measurement for ecological and hydrological watershed-scale observatories: A review, *Vadose Zone Journal*, *7*, 358–389.

Robock, A., C. A. Schlosser, K. Y. Vinnikov, N. A. Speranskaya, J. K. Entin, and S. Qiu (1998), Evaluation of the AMIP soil moisture simulations, *Global and Planetary Change*, *19*, 181–208.

Robock, A., K. Y. Vinnikov, G. Srinivasan, J. K. Entin, S. E. Hollinger, N. A. Speranskaya, S. Liu, and A. Namkhai (2000), The Global Soil Moisture Data Bank, *Bulletin of the American Meteorological Society*, *81*, 1281–1299.

Rodriguez-Iturbe, I., G. Vogel, R. Rigon, D. Entekhabi, F. Castelli, and A. Rinaldo (1995), On the spatial organization of soil moisture fields, *Geophysical Research Letters*, *22*(20), 2757–2760.

Rosenbaum, U., J. Huisman, A. Weuthen, H. Vereecken, and H. Bogena (2010), Sensor-to-sensor variability of the ECH2O EC-5, TE and 5TE sensors in dielectric liquids, *Vadose Zone Journal*, *9*(1), 181–186.

Roth, K., R. Schulin, H. Fluehler, and W. Attinger (1990), Calibration of time domain reflectometry for water content measurement using a composite dielectric approach, *Water Resources Research*, *26*(10), 2267–2273.

Rüthnick, M. (1998), Zusammenhänge zwischen Bodenart und Eigenschaften eines Bodens (correlation between soil texture and soil properties), Figure, source: Geographisches Institut Universität Hannover 1990, Graphik: Rüthnick, M. 1998.

Sabins, F. F. (1996), *Remote Sensing: Principles and Interpretation*, 3 ed., W. H. Freeman and Company, New York, USA.

Saleh, K., J.-P. Wigneron, P. de Rosnay, J.-C. Calvet, M. Escorihuela, Y. Kerr, and P. Waldteufel (2006b), Impact of rain interception by vegetation and mulch on the L-band emission of natural grass, *Remote Sensing of Environment*, *101*, 127–139.

Saleh, K., J.-P. Wigneron, P. Waldteufel, P. de Rosnay, M. Schwank, J.-C. Calvet, and Y. Kerr (2007), Estimates of surface soil moisture under grass covers using L-band radiometry, *Remote Sensing of Environment*, *109*, 42–53.

Saleh, K., et al. (2009), Soil moisture retrievals at L-band using a two-step inversion approach (COSMOS/NAFE'05 Experiment), *Remote Sensing of Environment*, *113*, 1304–1312.

Schaefer, G. L., M. H. Cosh, and T. J. Jackson (2007), The USDA Natural Resources Conservation Service Soil Climate Analysis Network (SCAN), *Journal of Atmospheric and Oceanic Technology*, *24*, 2073–2077.

Scharling, M. (1999), Klimagrid Danmark Nedboer 10 x 10 km (ver.2), *Technical Report 99-15*, Danish Meteorological Institute, Copenhagen, p. 18 (in Danish).

Scheffer, F., and P. Schachtschabel (2002), *Lehrbuch der Bodenkunde*, Spektrum Akademischer Verlag GmbH, Heidelberg, Berlin.

Schlenz, F., J. T. Dall'Amico, A. Loew, and W. Mauser (Accepted), Uncertainty assessment of the SMOS validation in the Upper Danube Catchment, *IEEE Transactions on Geoscience and Remote Sensing*.

Schmugge, T., J. Wang, and G. Asrar (1988), Results from the push broom microwave radiometer flights over the Konza Prairie in 1985, *IEEE Transactions on Geoscience and Remote Sensing*, *26*(5).

Schmugge, T. J., T. J. Jackson, and H. L. McKim (1980), Survey of methods for soil moisture determination, *Water Resources Research*, *16*(6), 961–979.

Schou, A. (1949), Atlas over danmark, 1:750.000, Det Kongelige Danske Geografisk Selskab med støtte af den Danske Stat, Carlsbergfondet og private virksomheder. H. Hagerup, C.A. Reitzels Forlag, København.

Schwank, M., C. Mätzler, M. Guglielmetti, and H. Flühler (2005), L-band radiometer measurements of soil water under growing clover grass, *IEEE Transactions on Geoscience and Remote Sensing*, *43*(10), 2225–2237.

Skou, N., S. Søbjærg, J. Balling, and S. Kristensen (2006), A second generation L-band digital radiometer for sea salinity campaigns, in *Geoscience and Remote Sensing Symposium (IGARSS)*, pp. 3984–3987, Denver, CO, USA.

Skou, N., S. S. Søbjærg, J. Balling, S. S. Kristensen, and A. Kusk (2010a), EMIRAD-2 and its use in the SMOS Cal/Val campaign, *Tech. Rep. AR 502*, DTU Space, Kgs. Lyngby, Denmark.

Skou, N., S. Misra, J. E. Balling, S. S. Kristensen, and S. S. Søbjærg (2010b), L-band RFI as experienced during airborne campaigns in preparation for SMOS, *IEEE Transactions on Geoscience and Remote Sensing*, *48*(3), 1398–1407.

Skou, N., J. Balling, S. S. Søbjærg, and S. S. Kristensen (2010c), Surveys and analysis of RFI in the SMOS context, in *Proceedings of IGARSS*, pp. 2011–2014.

Smed, P. (1979), Landskabskort over Danmark, 1:360.000, Geografforlaget, 5464 Brenderup.

Strahler, A. H., and A. N. Strahler (1999), *Physische Geographie*, Verlag Eugen Ulmer Stuttgart.

Topp, G. C., J. L. Davis, and A. P. Annan (1980), Electromagnetic determination of soil water content: Measurement in coaxial transmission lines, *Water Resources Research*, *16*(3), 574–582.

Ulaby, F. T., R. K. Moore, and A. K. Fung (1981), *Microwave Remote Sensing: Active and passive. Volume I: Microwave Remote Sensing Fundamentals and Radiometry*, vol. 1, Addison-Wesley Publishing Company, Reading, MA, USA.

Ulaby, F. T., R. K. Moore, and A. K. Fung (1982), *Microwave Remote Sensing: Active and passive. Volume II: Radar Remote Sensing and Surface Scattering and Emission Theory*, vol. 2, Addison-Wesley Publishing Company, Reading, MA, USA.

Ulaby, F. T., R. K. Moore, and A. K. Fung (1986), *Microwave Remote Sensing: Active and passive. Volume III: From Theory to Appilcations*, vol. 3, Artech House, Inc., Dedham, MA, USA.

Vachaud, G., A. Passerat de Silans, P. Balabanis, and M. Vauclin (1985), Temporal stability of spatially measured soil water probability density function, *Soil Science Society of America Journal*, *49*, 822–828.

Van de Griend, A., and J.-P. Wigneron (2004), The b-factor as a function of frequency and canopy type at H-polarization, *IEEE Transactions on Geoscience and Remote Sensing*, *42*(4), 786–794.

Vasquez, V., and A. Thomsen (2010), Calibration of a capacitance probe for groundwater recharge modeling based on soil moisture dynamics, in *1st International Conference and Exploratory Workshop on Soil Architecture and Physio-chemical Functions (CESAR)*, Faculty of Agricultural Sciences, Aarhus University, Aarhus University Research Center Foulum, Denmark.

Vejen, F., H. Madsen, and P. Allerup (2000), Korrektion for fejlkilder på måling af nedbør - korrektionsprocenter ved udvalgte stationer 1989-1999, *Technical Report 00-20*, Danish Meteorological Institute, Copenhagen, p. 53 (in Danish).

Vinnikov, K. Y., A. Robock, N. A. Speranskaya, and C. A. Schlosser (1996), Scales of temporal and spatial variability of midlatitude soil moisture, *Journal of Geophysical Reserach*, *101*(D3), 7163–7174.

Wagner, W., G. Lemoine, and H. Rott (1999), A method for estimating soil moisture from ERS scatterometer and soil data, *Remote Sensing of Enviornment*, *70*, 191–207.

Wagner, W., G. Blöschl, P. Pampaloni, J.-C. Calvet, B. Bizzarri, J.-P. Wigneron, and Y. Kerr (2007), Operational readiness of microwave remote sensing of soil moisture for hydrologic applications, *Nordic Hydrology*, *38*(1), 1–20.

Walker, J. P., G. R. Willgoose, and J. D. Kalma (2001), The Nerrigundah data set: Soil moisture patterns, soil characteristics, and hydrological flux measurements, *Water Resources Research*, *37*(11), 2653–2658.

Wang, J., and T. Schmugge (1980), An empirical model for the complex dielectric permittivity of soil as a function of water content, *IEEE Transactions on Geoscience and Remote Sensing*, *GE-18*(4), 288–295.

Western, A. W., and G. Bloeschl (1999), On the spatial scaling of soil moisture, *Journal of Hydrology*, *217*, 203–224.

Western, A. W., G. Bloeschl, and R. Grayson (1998), Geostatistical characterisation of soil moisture patterns in the Tarrawarra Catchment, *Journal of Hydrology*, *205*, 20–37.

Western, A. W., R. B. Grayson, and G. Bloeschl (2002), Scaling of soil moisture: A hydrologic perspective, *Annual Review of Earth and Planetary Sciences*, *30*, 149–180.

Western, A. W., S. Zhou, R. B. Grayson, T. A. McMahon, R. B. Bloeschl, and D. J. Wilson (2004), Spatial correlation of soil moisture in small catchments and its relationship to dominant spatial hydrological processes, *Journal of Hydrology*, *286*, 113–134.

Wigneron, J., et al. (2011), Evaluating an improved parameterization of the soil emission in L-MEB, *IEEE Transactions on Geoscience and Remote Sensing*, *49*(4).

Wigneron, J.-P., A. Chanzy, J.-C. Calvet, and N. Bruguier (1995), A simple algorithm to retrieve soil moisture and vegetation biomass using passive microwave measurements over crop fields, *Remote Sensing of the Environment*, *51*, 331–341.

Wigneron, J.-P., L. Laguerre, and Y. Kerr (2001), A simple parameterization of the L-band microwave emission from rough agricultural soils, *IEEE Transactions on Geoscience and Remote Sensing*, *39*(8).

Wigneron, J.-P., A. Chanzy, J.-C. Calvet, A. Olioso, and Y. Kerr (2002), Modeling approaches to assimilating L-band passive microwave observations over land surfaces, *Journal of Geophysical Research*, *107*(D14), ACL11–1–14, atmosphere.

Wigneron, J.-P., et al. (2007), L-band Microwave Emission of the Biosphere (L-MEB) model: Description and calibration against experimental data sets over crop fields, *Remote Sensing of Environment*, *107*, 639–655.

Woodhouse, I. H. (2006), *Introduction to Microwave Remote Sensing*, CRC Press, Taylor & Francis Group, Boca Raton, FL, USA.

Woods, R. A., R. B. Grayson, A. W. Western, M. J. Duncan, and D. J. Wilson (2001), *Observations and Modeling of Land Surface Hydrological Processes*, chap. Experiment design and initial results from the Mahurangi River variability experiment: MARVEX, American Geophysical Union.

Acknowledgments

There is a long list of people who I would like to thank for their support in various ways throughout my PhD studies:

First of all I want to acknowledge the support from the side of my supervisors: Niels Skou, Henning Skriver and Inge Sandholt gave me the opportunity to work on this thesis and were there when help was needed. They also made it possible for me to participate in numerous workshops and conferences as well as the Australian SMOS Cal/Val campaign where I had the chance to meet worldwide SMOS specialists, connect with this community and learn from their experience. Thank you very much!

At the same time I would also like to show my appreciation to the HOBE project leader: Karsten Høgh Jensen showed me his strong interest in my work and his support and encouragement helped me to overcome many obstacles. Thanks a lot!

Yann Kerr provided me the possibility to work in the SMOS team at the Centre d'Etudes Spatiales de la Biosphère, Toulouse, France. During several stays in Toulouse I gained valuable insight into the secrets of SMOS and the approaches to deeply dig into its data, which has clearly broadened my scientific horizon. Thank you so much Yann Kerr, Delphine Leroux, Elsa Jacquette, Arnaud Mialon, Philippe Richaume, Silvia Enache Juglea, Heather Lawrence, Ahmad Albitar, Claire Gruhier, Olivier Merlin, Lucie Berthon, Yan Soldo, François Cabot, Ali Khazaal, Arnaud Quesney for a great time in Toulouse, for many fruitful discussions, the possibility to work with the SMOS data and your codes to process it, and not less for many pleasant coffee and lunch breaks as well as loads of cheerful evenings in town to forget about work in between! And in this context, I would also like to thank Eric Anterrieu from the Laboratoire Astrophysique de Toulouse - Tarbes for providing data processed with the RFI detection scheme for the Danish validation site.

During my PhD-studies I had the opportunity to participate in the Australian Airborne Cal/val Experiment for SMOS. This experience was a most valuable contribution to my work, particularily in preparation for the organisation of the HOBE airborne campaign. Thank you very much Jeff Walker, Sandy Peischl and Chris Rüdiger for sharing your knowledge with me, introducing me to this new topic and to make the stay in Australia an unforgettable journey!

During installation of the soil moisture network and the organisation of the HOBE airborne campaign I have also spent a remarkable amount of days in the field in the Skjern River Catchment. I have very much enjoyed the time outdoors and thereby, got the strong support from the HOBE technician: Thank you very much Lars Rasmussen for many pleasant field days, your very helpful technical advises and also for giving me confidence in my work! Furthermore, I would like to thank the field manager at and around the HOBE study site

Voulund, Torben Hansen, who was always there for support and thought me fundamental knowledge about farming in Denmark.

For the organisation of the HOBE airborne campaign I could count on numerous helping hands. First, there was the HOBE academic secretary, Frederik Uldall, who did an incredible job in the organisation of the logistics, and again, Lars Rasmussen spent many hours to assist the preparations in the field. Furthermore, I would like to mention the precious contributions from Hector Nieto and Eline Bojsen Haarder, as well as Dennis who prepared excellent food for us in Salten Skov. During the campaign various people found their way to the Danish fields. In the first week of the campaign, together with Christian Hauck from the Department of Geosciences, University of Fribourg, Switzerland, I organized a field course in the framework of their master program. This was a great opportunity for me to be introduced to academic teaching. Christian's openness for this collaboration as well as his extensive experience with soil moisture measurements were of extreme value. In the second week, I was supported by many people comming from several institutes in and around Denmark. Without you, the measurements would not have been possible: Christian Hauck, Frida Zettergren, Samuel Arrigo, Roland Huguenin, Alice Voinesco, Alexandre Abbet, Pierre Joly, Sovik Kumar Nath, Ekim Saraclar, Stefano Bergamaschi, Melina Dini, Antoine Marmy, Aris Bugada, Cecile Pellet, Mazzal Stokvis, Etienne Rosset, Horst Machguth, Eline Bojsen Haarder, Hector Nieto, Delphine Leroux, Elsa Jacquette, Roos-Anne Schrooten, Robin du Mée, Kinza Haider, Xiulan He, Ida B. Karlsson, Mette Bakmand-Mikalski, Steen Savstrup Kristensen, Vicente Vasquez, Lars Rasmussen, Sachin Karan. Thank you very much for your dedication and also for maintaining a great atmosphere throughout the campaign which helped me a lot to relieve stress from this heavy burden! I woul also like to thank Karsten Høgh Jensen and Niels Skou who came by to make sure that everything was in order, as well as Jan E. Balling for his efforts in the operation of the airborne radiometer. Last but not least, I am very greatful for the texture analysis done by Inge Juul from the Department of Geography and Geology at the University of Copenhagen.

I also would like to say thank you to my colleagues at DTU Space. Special thank goes to Jan E. Balling for the EMIRAD data processing, the collaboration on data comparison, the translation of my abstracts into Danish, as well as many pleasant lunch breaks. Furthermore, I would like to especially mention the great support from Birte Kronbak Andersen in various administrative issues and her encouraging words. Thanks a lot!

My deepest thankfulness is offered to my parents, family and friends in Switzerland for their continuous caring and moral support on my way and for strengthen my confidence when it was urgently needed. Finally, I cannot express my gratitude for the support of Horst Machguth in mere words. He substantially contributed to this work with precious scientific advice from an outside view as well as help in formatting this manuscript - and thereby definitely convinced me about the advantages of LaTeX;-) But even more importantly, he was always there for me, inspired me and never lost faith in me and my work. Thank you very very much!!

Part IV.

Appendix

A. Revised campaign soil moisture measurements

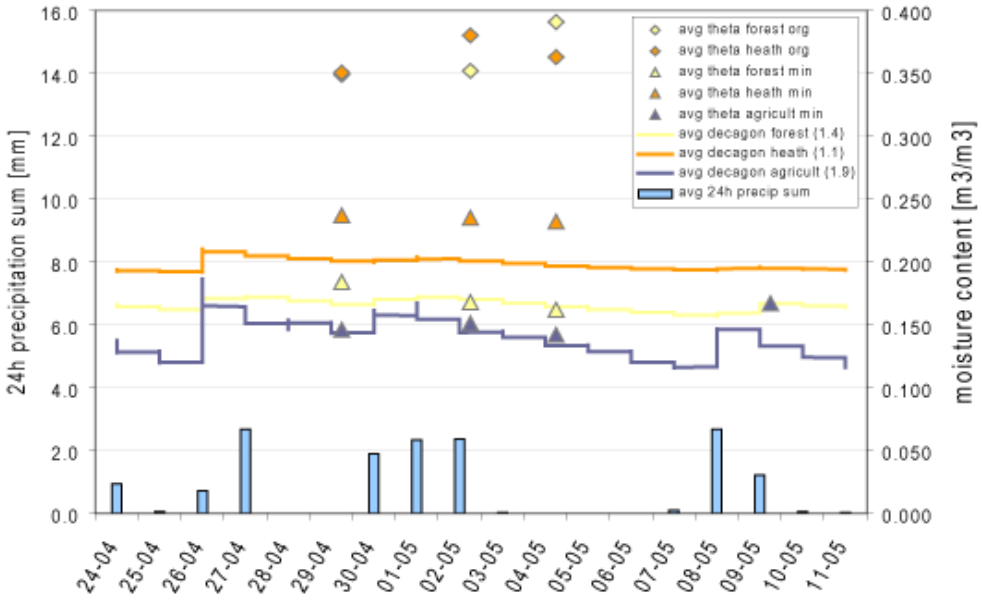

Figure A.1.: Average 24-hour precipitation sum [mm] of 5 closest rain gauges of the Danish Meteorological Institute, avgerage moisture $[m^3/m^3]$ from hand-held campaign ThetaProbe readings (recalculated using site-specific calibration) per sampling patch (agriculture, heath and forest) and Decagon 5TE measurements (0-5 cm depth) of one network station within each patch during the airborne campaign in the Skjern River Catchment. In case of forest and heath, both, the mineral as well as the organic data is shown.

Table A.1.: Average (Avg.) and standard deviation (Std.) of ThetaProbe moisture readings (recalculated using site-specific calibration) $[m^3/m^3]$ per sampling patch (A: agriculture, H: heath and F: forest) and day for mineral (min.) and organic (org.) substrates, respectively.

	A min.		H min.		org.		F min.		org.	
	Avg.	Std.	Avg.	Std.	Avg.	Std.	Avg.	Std.	Avg.	Std.
29-apr	0.146	0.031	0.237	0.075	0.351	0.170	0.184	0.075	0.349	0.120
02-may	0.151	0.033	0.235	0.069	0.380	0.158	0.168	0.070	0.352	0.125
04-may	0.142	0.026	0.232	0.073	0.363	0.160	0.162	0.060	0.391	0.133
09-may	0.167	0.027								

DTU Space
National Space Institute
Technical University of Denmark

Juliane Maries Vej 30
DK - 2100 Copenhagen Ø
Tel (+45) 3532 5701
Fax (+45) 3536 2475

www.space.dtu.dk

ISBN-13 978-87-92477-09-5